

Annual Research Briefs – 1988

Center for Turbulence Research

February 1989



Ames Research Center



Stanford University

CONTENTS

Preface	1
The length scale for sub-grid-scale parameterization with anisotropic resolution D. K. LILLY	3
Turbulence modeling T. -H. SHIH	11
On curve and surface stretching in turbulent flow N. ETEMADI	19
Renormalization group analysis of turbulence L.M. SMITH	29
Low-dimensional chaos in turbulence J. A. VASTANO	35
Close interactions of 3d-vortex tubes M. V. MELANDER	39
Numerical simulation of viscous vortex rings S. K. STANAWAY	51
The effects of particle loading on turbulence structure and modelling K. D. SQUIRES and J. K. EATON	55
Analyses of turbulence structures in shear flows M. J. LEE	63
Direct numerical simulation of compressible free shear flows S. K. LELE	79
Direct simulation of compressible reacting flows T. J. POINSOT	99
Turbulent transport in the solar nebula K. W. THOMPSON	107
Transition to turbulence in laminar hypersonic flow J. VAN DER VEGT	115
Direct numerical simulations of turbulent convection with a variable gravity and Keplerian rotation W. CABOT	121
Experimental investigation of flow over a backward facing step-progress report L. W. B. BROWNE	127
The effects of stabilizing and destabilizing longitudinal curvature on the structure of turbulent, two-stream mixing layers M. W. PLESNIAK and J. P. JOHNSTON	147
An experimental investigation of a low Reynolds number turbulent boundary layer subject to an adverse pressure gradient J. H. WATMUFF	153
Appendix	167

PRECEDING PAGE BLANK NOT FILMED

Preface

This report contains the 1988 annual progress reports by the Postdoctoral Fellows of the Center for Turbulence Research. It is intended primarily as a contractor report to the National Aeronautics and Space Administration, Ames Research Center. A separate report entitled, "Studying turbulence using numerical simulation databases -II," covering the 1988 Summer program activities was released earlier this year.

The primary objective of the CTR is to stimulate and produce advances in physical understanding of turbulence, in turbulence modeling and simulation, and in turbulence control. The primary means by which CTR seeks to achieve these objectives is by bringing together key individuals in fields bearing on turbulence to address diverse problems in turbulence. Postdoctoral Research Fellows and students conduct research in collaboration with staff of NASA-Ames Research Center and Stanford faculty members, using a substantial array of research facilities provided by both institutions.

Four thrust areas have been established for research:

1. Fundamental modeling of turbulence
2. Turbulence structure and control
3. Transition and turbulence in high-speed compressible flows
4. Turbulent reacting flows

These program areas have been used in selecting the Research Fellows and also as a guide for turbulence research by graduate students. The CTR roster for 1988 is provided in the Appendix. All Fellows with tenure of more than two months at the Center provided a written report outlining their study and accomplishments which appear in the following pages. The reports are grouped in the general areas of modeling, theory and simulation, compressible and reacting flows, and experimental research.

Parviz Moin
William C. Reynolds
John Kim

The length scale for sub-grid-scale parameterization with anisotropic resolution

By D. K. LILLY¹

Abstract

Use of the Smagorinsky eddy-viscosity formulation and related schemes for sub-grid-scale parameterization of large eddy simulation models requires specification of a single length scale, earlier related by Lilly to the scale of filtering and/or numerical resolution. An anisotropic integration of the Kolmogoroff enstrophy spectrum allows generalization of that relationship to anisotropic resolution. It is found that the Deardorff assumption is reasonably accurate for small anisotropies and can be simply improved for larger values.

1. Introduction

Numerical integration of the time-dependent equations of fluid dynamics to simulate evolution of the largest scales of motion has been applied for about 30 years, initially in the field of weather prediction. Early workers were concerned over what to do about the scales of motion too small to be resolved by the computer, but the problem was often confused with the numerical errors introduced by finite difference algorithms. The technique that Smagorinsky (1963) introduced grew out of an empirical variable eddy viscosity method due, I believe to R. Richtmyer (no reference available), for smoothing simulated shock wave calculations. Smagorinsky and his associates recognized, however, that Richtmyer's variable viscosity was also consistent with the notion of a universal equilibrium range of turbulence. I pursued this point and used the Kolmogoroff inertial sub-range hypothesis to quantitatively relate the length scale required in the Smagorinsky formulation to the resolved scale (Lilly, 1966, 1967). I assumed isotropic resolution, although numerical simulations then and now often are carried out with anisotropic resolution. The question of how to generalize my expression for this purpose has engaged some attention. Deardorff (1970) assumed that the length scale is proportional to the cube root of the product of the resolution scales in the three directions. Alternatives have also been proposed, most of them involving the effects of a nearby boundary. Piomelli, et al (1987) review the subject and conclude that no real consensus has yet emerged, though Deardorff's formulation is widely used.

1 Permanent Address: CIMMS, University of Oklahoma

The purpose of this note is to aid in resolving this issue. I extend my earlier calculation, oriented now toward spectral and pseudo-spectral integration techniques, to allow resolution to vary with direction. I still assume, however, that the small scale limit of the simulation is in the Kolmogoroff inertial sub-range in all directions. This is a serious limitation, as the most common reason for applying anisotropic resolution is an expectation of anisotropic and/or inhomogeneous turbulence, typically in regions close to a boundary. Thus the scale anisotropy problem is usually compounded with a boundary layer problem and with the likelihood that a classical inertial sub-range may not exist, at least in the scales resolved by the simulation. Piomelli, et al (1987) discuss and test several additional parameterizations intended to improve the boundary layer resolution, but all are modifications of an isotropic formulation related to Deardorff's. The results to be presented here are offered to test and perhaps improve the Deardorff assumption.

2. The problem and the solution

Consider the problem of integrating the Navier-Stokes equation under conditions of incompressibility and constant density, so that

$$\partial u_i / \partial t + \partial(u_i u_j) / \partial x_j + \partial p / \partial x_i = \nu \partial^2 u_i / \partial x_j^2 \quad (1)$$

and

$$\partial u_i / \partial x_i = 0, \quad (2)$$

where p is pressure divided by density, and other terminology is conventional. A low-pass spatial filter is applied to these equations, in recognition of the limited resolution available to any real discretization technique. In the early development era this was typically a uniform average over a box surrounding a spatial grid point. Leonard (1974) introduced the use of Gaussian filters, a technique which is widely applied in engineering fluid dynamics simulations. In many current research simulations the effective filter is the spectral cut-off of a finite Fourier transform. In any case it is assumed to be a linear operator and is here designated by angle brackets $\langle \rangle$. Because it is linear it may be exchanged with the differential operators in (1) and (2) and applied to the flow variables directly. This allows the linear terms of the equations to be integrated as if they were unfiltered. The filtered momentum flux product, $\langle u_i u_j \rangle$, cannot, however, be resolved directly from the filtered velocities, and must be subject to a creative parameterization.

I assume the decomposition of the momentum flux product applied by Smagorinsky, Lilly, and Deardorff, i.e.

$$\begin{aligned}
\langle u_i u_j \rangle &= \langle u_i \rangle \langle u_j \rangle - \tau_{ij} + \delta_{ij} E, \\
\tau_{ij} &= - \langle u_i u_j \rangle + \langle u_i \rangle \langle u_j \rangle - \delta_{ij} E \\
E &= (\langle u_i^2 \rangle - \langle u_i \rangle^2) / 2
\end{aligned} \tag{3}$$

with τ_{ij} designated as the subgrid scale (SGS) stress, E the SGS kinetic energy, and δ_{ij} is the Kronecker delta. The filtered equations of motion and continuity are now written as

$$\begin{aligned}
\partial \langle u_i \rangle / \partial t + \partial (\langle u_i \rangle \langle u_j \rangle) / \partial x_j + \partial \pi / \partial x_i \\
= \partial \tau_{ij} / \partial x_j + \nu \partial^2 \langle u_i \rangle / \partial x_j^2
\end{aligned} \tag{4}$$

$$\partial \langle u_i \rangle / \partial x_i = 0, \tag{5}$$

where $\pi = \langle p \rangle + E$.

The Smagorinsky parameterization for the SGS stress is of the eddy viscosity type, given by

$$\tau_{ij} = K(S_{ij} + S_{ji}), \tag{6}$$

where $S_{ij} = \partial \langle u_i \rangle / \partial x_j$, and

$$K = \lambda^2 S, \tag{7}$$

where $S^2 = S_{ij}(S_{ij} + S_{ji})$. The length scale λ was assumed by Smagorinsky to be proportional to the grid resolution. Some investigators have replaced S by ω , the square root of the enstrophy, i.e. $\omega^2 = (\partial u_i / \partial x_j - \partial u_j / \partial x_i)^2 / 2$. Not much difference is found in practice, corresponding to the fact that the volume integrals of S^2 and ω^2 are identical and they have the same Fourier spectral amplitudes.

I evaluated the length scale λ by assuming the validity of inertial cascade theory and neglecting intermittency effects. If the resolved kinetic energy equation is derived by multiplying (4) by $\langle u_i \rangle$, the contribution from the eddy stress term is

$$\begin{aligned}
\langle u_i \rangle \partial \tau_{ij} / \partial x_j &= \partial (\langle u_i \rangle \tau_{ij}) / \partial x_j - K S^2 \\
&= \partial (\langle u_i \rangle \tau_{ij}) / \partial x_j - \lambda^2 S^3
\end{aligned} \tag{8}$$

The first term on the rhs is variable in sign and vanishes or is small in the volume average, while the second term is always negative. It is assumed that the loss of energy from the resolved scales, $\lambda^2 S^3$, is the same as the viscous dissipation of energy, ϵ . These are equated after evaluating S^2 from spectral integration, i. e.

$$S^2 = \int_0^{k_m} k^2 E(k) dk \tag{9}$$

where $E(k)$ is the spectral amplitude of kinetic energy, defined as an integral along the surfaces of spheres in spectral space. The wavenumber k_m must correspond to the resolution limit, which is the cut-off wavenumber for spectral discretization. It is assumed that at and near k_m the energy spectrum is given by the inertial range form, i.e.

$$E(k) = \alpha \epsilon^{2/3} k^{-5/3}, \quad (10)$$

where α is the Kolmogoroff constant, about 1.5, and ϵ is the viscous dissipation of kinetic energy. Substitution of (10) into (9) leads to the result of integration

$$S^2 = (3/4) \alpha \epsilon^{2/3} k_m^{4/3} \quad (11)$$

The rate of energy removal from the resolved flow is evaluated by substituting (11) into the last term of (8) so that

$$\lambda^2 S^3 = (3\alpha/4)^{3/2} \lambda^2 \epsilon k_m^2 \quad (12)$$

Equating this expression to dissipation allows evaluation of the length scale as

$$\lambda = S^{-3/2} \epsilon^{1/2} = (4/3\alpha)^{3/4} k_m^{-1} \quad (13)$$

One may now set $k_m = \text{constant}/\Delta$, where Δ is the grid interval, assumed to be isotropic. The minimum value for the constant, assuming the spectral wavelengths are bounded by the Nyquist limit, is two. When pseudo-spectral integration techniques are applied, in order to avoid aliasing the constant must be no less than three, which increases λ by 50%.

I now wish to drop the assumption of resolution isotropy. For simplicity I assume, however, axisymmetry, i.e. that the limits of resolution in two of the three dimensions are the same. The typical situation involves *increased* resolution close to a boundary, either through a variable grid length or use of Chebyshev polynomials. Within the axisymmetric framework one also may consider the effects of *decreased* resolution in one direction. In the conclusion section I argue that the results for different resolution in all three directions can be determined adequately from the axisymmetric case.

Results are obtained by writing the enstrophy spectrum function in three-dimensional spectral space and integrating it over prolate or oblate spheroids, that is figures obtained by rotating an ellipse about its long or short axis. This may not correspond accurately to the resolution limits in a model using Fourier modes in two dimensions and Chebyshev polynomials or finite differences in the third, but it is more readily compared with the isotropic case. Similar results can be obtained by assuming a cylindrical volume in wavenumber space, but they differ only slightly and not in any qualitatively important manner.

If the three-dimensional spectrum function is isotropic, as assumed, it is $E(k)/4\pi k^2$, and the 3-d enstrophy or S^2 spectrum is $E(k)/4\pi$. The wavenumber spheroid is assumed to be bounded by the equation for an ellipsoid, i.e.

$$(k_h/k_{hm})^2 + (k_z/k_{zm})^2 = 1$$

where k_h is the wavenumber in the axisymmetric direction, notationally assumed to be horizontal, and k_z is that in the vertical direction, with k_{hm} and k_{zm} the horizontal and vertical spectral limits. In place of (9), the evaluation of S^2 is accomplished by integration over the spheroid as follows:

$$S^2 = \int_0^{k_{zm}} \int_0^{k_{h1}} E(k) k_h dk_h dk_z \quad (14)$$

The limit on the first integral is $k_{h1} = k_{hm}(1 - k_z^2/k_{zm}^2)^{1/2}$. Note that if $E(k)$ were replaced by 4π in (14), the integral would give the volume of the wavenumber spheroid, $4\pi k_{hm}^2 k_{zm}$. With the energy spectrum given by (10), with $k^2 = k_h^2 + k_z^2$, integration of (14) yields

$$S^2 = (3/4)\alpha\epsilon^{2/3} k_{hm}^{8/9} k_{zm}^{4/9} y(r) \quad (15)$$

$$\text{where } r = k_{hm}/k_{zm} \text{ and } y = r^{10/9} \int_0^1 [r^2 + (1 - r^2)x^2]^{-5/6} dx.$$

The particular form for S is chosen so that if it is substituted into the first equality of (13), with $y = 1$ and the wavenumbers assumed to be inversely proportional to the grid spacings Δx , Δy , Δz , one obtains the expression assumed by Deardorff, i.e. $\lambda \sim (\Delta x \Delta y \Delta z)^{1/3}$. More generally, upon substituting S into (13) one obtains

$$\lambda = \lambda_D y^{-3/4}, \lambda_D = (4/3\alpha)^{3/4} k_{hm}^{-2/3} k_{zm}^{-1/3}, \quad (16)$$

with λ_D equivalent to Deardorff's expression.

The integral for y in (15) can be reduced to the forms

$$y = r^{4/9} (1 - r^2)^{-1/2} \int_0^{x_m} (\cos x)^{-1/3} dx, \tan x_m = (1 - r^2)^{1/2}/r, \text{ for } r < 1 \quad (17a)$$

$$y = r^{4/9} (r^2 - 1)^{-1/2} \int_0^{x_m} (\cos x)^{-2/3} dx, \sin x_m = (r^2 - 1)^{1/2}/r, \text{ for } r > 1 \quad (17b)$$

For the extreme cases $r = 0, \infty$, the integration limits x_m become $\pi/2$ in both expressions, and the integrals are evaluated in terms of tabulated Gamma functions. Thus for small r , $S^2 \sim k_{hm}^{4/3}$ and $\lambda \sim k_{hm}^{-1}$, while for large r , $S^2 \sim k_{hm}^{1/3} k_{zm}$ and $\lambda \sim k_{hm}^{-1/4} k_{zm}^{-3/4}$. A somewhat more revealing interpretation can be obtained by differentiating λ with respect to r . This yields the following:

$$-1/3 \text{ for } r \ll 1 \quad (18a)$$

$$r\lambda^{-1}\partial\lambda/\partial r = -(3r/4y)\partial y/\partial r = 0 \text{ for } r = 1 \quad (18b)$$

$$5/12 \text{ for } r \gg 1 \quad (18c)$$

$$\partial^2\lambda/\partial(\ln r)^2 = (4/27)\lambda_D \text{ at } r = 1. \quad (18d)$$

These show that the Deardorff expression is valid in the vicinity of $r = 1$, but that with increasing anisotropy in either direction λ becomes larger than λ_D . Fig. 1 is a plot of λ/λ_D . The data for the curve labelled "Length scale" were calculated to two-three digit accuracy by using the (18d) for $.05 < r < 20$ and matching that with an expansion of the expressions in (17a,b) around their limiting values. The straight lines are plots of the asymptotic forms, that is $y^{-3/4}$ for the y 's given by (17a) for $r \ll 1$ and (17b) for $r \gg 1$.

An accurate approximation for $.02 < r < 50$ is

$$\lambda/\lambda_D = r^{(2/27)^{1/2}} + r^{-(2/27)^{1/2}} - 1 \quad (19)$$

This is obtained as a solution to (18d), but with the rhs replaced by $(2/27)(\lambda + \lambda_D)$. This relation is also plotted in Fig. 1, and is imperceptibly different from the "Length scale" except at the most extreme anisotropies.

3. Conclusions

The results of the above calculation indicate that the Deardorff formulation is accurate to within 20% for $.2 < r < 5$. For anisotropies greater than that the length scale should be increased, with (19) sufficiently accurate for anisotropies less than a factor of 50 either way. Such large anisotropies are unlikely to produce accurate simulations in any case, and probably need to be enhanced by more sophisticated parameterizations than the Smagorinsky formulation.

Upon consideration of the nature of these solutions, it seems evident that they can be extended to the case where the resolution is different in all three directions. Since equation (18) or (19) is symmetric in $\ln r$, it doesn't seem to matter much whether two wavenumber limits are larger and one smaller, or one larger and two smaller. Apparently the results are only sensitive to the largest ratio of the length scales, so presumably the existence of a third dimension with an intermediate resolution would have little effect.

REFERENCES

- DEARDORFF, J. W. 1970 A numerical Study of three-dimensional turbulent channel flow at large Reynolds numbers. *J. Fluid Mech.* **41**, 453-480.

- LEONARD, A. 1974 Energy cascade in large-eddy simulations of turbulent fluid flows. *Adv. Geophys.* **18A**, 237-248.
- LILLY, D. K. 1966 On the application of the eddy viscosity concept in the inertial sub-range of turbulence. *NCAR Manuscript No. 123* Boulder, CO.
- LILLY, D. K. 1967 The representation of small-scale turbulence in numerical simulation experiments. *Proceedings of the IBM Scientific Computing Symposium on Environmental Sciences*. Yorktown Heights, NY.
- PIOMELLI, U., J. H. FERZIGER, AND P. MOIN 1987 Models for large eddy simulations of turbulent channel flows including transpiration. *Report TF-32*, Thermosciences Division, Department of Mechanical Engineering, Stanford University, 185 pp.
- SMAGORINSKY, J. 1963 General circulation experiments with the primitive equations. I. The basic experiment. *Mon. Weather Rev.* **91**, 99-164.

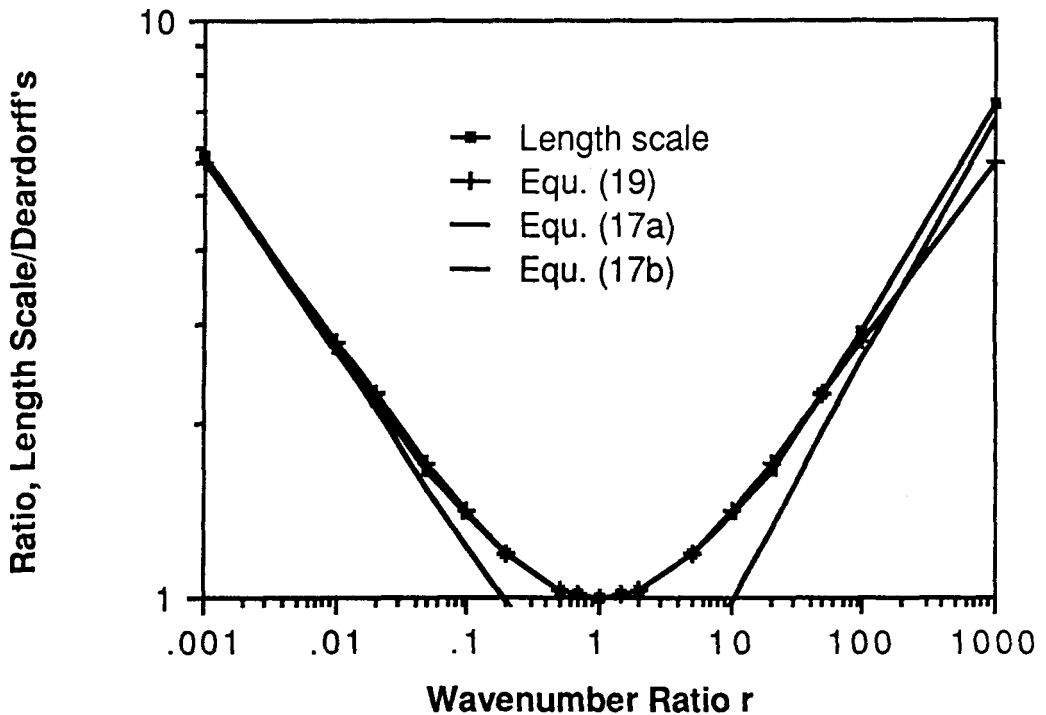


FIGURE 1. The turbulence length scale, normalized by Deardorff's (1970) assumption, and determined by solution of (13) and (15), for various ratios of the limiting wavenumbers, k_{hm}/k_{zm} . The straight lines are asymptotic forms from (17a,b) and the curve marked with + signs is an approximation given by (19).

Turbulence modeling

By T. -H. SHIH

1. Motivation and Objective

Motivation

In recent years codes that use the Navier-Stokes equations to compute aerodynamic flows have evolved from computing two-dimensional flows around simple airfoils to computing flows around full scale aircraft configurations. Most flows of engineering interest are turbulent and turbulence models are needed for their prediction. Yet, we know that present turbulence models are adequate only for simple flows and do poorly in complicated flows such as three-dimensional separation, large-scale unsteadiness, etc. The same progress that allowed the development of these aerodynamic codes, namely the introduction of supercomputers, has allowed us to compute directly turbulent flows, albeit only for simple flows at moderate Reynolds numbers. These direct turbulence simulations provide us with detailed data that experimentalists have not been able to measure. This work is motivated by the fact that data exists for developing better turbulence models and by the need for better models to compute flows of engineering interest.

Objective

The objective of this work is then to develop turbulence models for engineering applications. The model categories that show promise for immediate use are on the two-equation level and the Reynolds-stress level. We will make use of existing methodologies to develop models. The models will be tested using data from direct simulations, experiments and analysis. Specifically, our objectives are as follows:

1. Examine the Reynolds stress budgets using direct simulation flow fields (Mansour et al 1988, Moin et al 1989).
2. Use Rapid Distortion Theory to analytically study the effects of mean deformation on turbulence. In particular, examine the development of the rapid pressure-strain under rapid distortions.
3. Compare existing models with data and theory. Develop models where needed using appropriate expansions and constraints. Test these new models using results from direct simulation, experiment and theory.
4. Use the method of moment generating function to extend second order closures to higher order closures. We know that there exist a close connection between high-order moments and coherent structures. The moment generating

function approach should allow us to include the effect of coherent structures on the models.

5. Extend turbulence modeling to compressible flows.

2. Work Accomplished

1. Numerical simulation of a three-dimensional boundary layer — AIAA paper no. 89-0373 (work supported in part by AFOSR)

The objective of this simulation is to study the mechanics of three-dimensional boundary layers and develop improved models for their predictions. Three-dimensional effects were achieved by direct simulation of a fully developed turbulent channel flow subjected to transverse pressure gradient. To obtain a good statistical sample during the transient period, 14 computer runs were ensemble averaged. Each run started from a different realization of the channel flow (far apart in time). The simulation shows that, in agreement with experimental observations, the Reynolds stresses are reduced and that near the wall a lag develops between the stress and the strain rate. The reduction in the stress is due largely to a drop in the production rate and an increase in the dissipation rate. In the coming year, we will study the performance of existing second order closures in predicting this drop and introduce improvements where needed.

2. k - ϵ modeling

k - ϵ turbulence models are often used in computing engineering flows with moderate success. In general, the flow field is qualitatively well predicted, but quantitative agreement often falls short. In the case of Reynolds stress modeling the question of a length scale for an eddy viscosity does not arise, and the energy dissipation rate, ϵ , is one of the unknowns of the problem. In this work an ϵ equation has been developed following the methodology of Lumley (1978). We used it in connection with both two-equation modeling and Reynolds stress modeling.

A two-equation model for use in low-Reynolds number flows has been tested against the channel data of Kim, Moin and Moser (1987). The modeled equations are given by,

$$k_{,t} + U_k k_{,k} = \left[\left(\frac{\nu_T}{\sigma_k} + \nu \right) k_{,k} \right]_{,k} + \nu_T S_{ij} S_{ij} - \epsilon$$

$$\epsilon_{,t} + U_k \epsilon_{,k} = \left[\left(\frac{\nu_T}{\sigma_\epsilon} + \nu \right) \epsilon_{,k} \right]_{,k} + C_1 \frac{\epsilon}{k} \nu_T S_{ij} S_{ij} - C_2 f_\epsilon \frac{\epsilon \tilde{\epsilon}}{k}$$

$$\begin{aligned}
\sigma_k &= 1 \\
\sigma_\epsilon &= 1.3 \\
C_1 &= 1.48 \\
C_2 &= 1.8 \\
\tilde{\epsilon} &= \epsilon - \phi \\
\phi &= k_{,j} k_{,j} / (2k) \\
\nu_T &= C_\mu f_\mu k^2 / \tilde{\epsilon} \\
C_\mu &= 0.09 \\
f_\mu &= 1 - \exp(-0.0115 \frac{u_\tau y}{\nu}) \\
f_\epsilon &= 1 - \frac{0.4}{1.8} \exp\left(-\left(\frac{k^2}{6\nu\epsilon}\right)^2\right)
\end{aligned}$$

We find that the model adequately predicts the mean velocity profile (see figure 1) and the turbulent kinetic energy (see figure 2).

3. Second order modeling of near-wall low-Reynolds number turbulence

A set of second order closure models for low-Reynolds number turbulence has been developed for the simulation of wall bounded flows without using wall functions. The wall effect is built in the pressure-strain correlation term of the Reynolds stress equation and in the modeled terms of the dissipation rate equation. We find that realizability is particularly important for modeling the near wall turbulence. The proposed models are particularly suitable for surfaces of arbitrary topology since they do not use the wall distance as a parameter. The models are tested by computing the fully developed channel flow. The full set of equations are used to compute the mean velocity, all the Reynolds stresses and the dissipation rate of the turbulent kinetic energy. We find reasonable agreement between the prediction of the mean profile and the data (see Figures 3) which is an indication that the shear stress is well predicted. However, the normal stresses are not as well predicted. In particular the streamwise component is underpredicted (see figure 4) while the transverse component is overpredicted. The cause of this shortcoming is still being investigated.

4. Second order modeling of a passive scalar in turbulent shear flows — AIAA paper no. 89-0607

A model equation for the scalar dissipation rate was proposed using the ansatz that the ratio of mechanical time scale to scalar time scale has an equilibrium value. In addition a model for the pressure related terms in the scalar flux equation was constructed based on consideration of realizability. The models were tested by comparison with experimental data for heated plane and axisymmetric jets.

5. Rapid Distortion Theory and 2-D 2-C turbulence modeling

Rapid distortion theory was used to analyze the development of the Reynolds stress in a 2-D 2-C homogeneous turbulence under mean irrotational strain and

mean shear. Here, 2-C refers to two-component turbulence. We found that the development of the Reynolds stress under 2-D 2C conditions is very different from its development under 3-D 3-C conditions. The findings can be summarized as follows:

1. The mean shear or strain have no effects on the isotropy of the Reynolds stress if the initial field is isotropic.
2. Initially anisotropic fields become isotropic under the influence of mean shear or strain.

These findings are opposite to the finding in 3D 3C turbulence where mean shear or strain will drive isotropic turbulence away from isotropy. In 2D 2C turbulence the pressure strain drives the Reynolds stresses back to isotropy.

A general 2D 2C model for the pressure-strain term, T_{ij} , was constructed which contains only one undetermined coefficient C ,

$$\frac{T_{ij}}{2k} = S_{ij} + 4Cb_{ik}b_{pj}S_{pk} + 2\Omega_{jk}b_{ik} + 2\Omega_{ik}b_{kj}$$

where,

$$S_{ij} = \frac{1}{2}(U_{i,j} + U_{j,i}), \quad \Omega_{ij} = \frac{1}{2}(U_{i,j} - U_{j,i})$$

$$b_{ij} = \frac{\overline{u_i u_j}}{2k} - \frac{1}{3}\delta_{ij}, \quad k = \frac{1}{2}\overline{u_i u_i}$$

Rapid distortion theory will be used to determine this coefficient. We postulate that the more general 3D 3C model should reduce to this model in the limit of 2D 2C turbulence.

3. Future Plans

1. Examine the performance of existing second order closures in predicting three-dimensional turbulent boundary layers. Introduce improvements where needed.
2. Use Rapid Distortion Theory to study the effects of mean deformation on turbulence. Extend the analysis developed for mean strain and shear to study the effect of rapid rotation on the turbulence.
3. Use the method of moment generating function to extend second order closures to higher order closures.
4. Use non-weighted ensemble averaging method (Shih et al, 1987) to extend the second order models to compressible flows. This averaging technique (as opposed to Favre averaging) will allow us to apply all the incompressible modeling methodologies to modeling compressible flows.

REFERENCES

- MANSOUR, N. N., MOIN, P. & KIM, J. 1988 Reynolds-stress and dissipation-rate budgets in a turbulent channel flow. *J. Fluid Mech.* **194**, 15-44.

MOIN, P., SHIH, T., DRIVER, D. & MANSOUR, N. 1989 Numerical Simulation of a Three-Dimensional Turbulent Boundary Layer AIAA 89-0373.

SHIH, T. H., LUMLEY, J. L., & JANICKA, J. 1987 Second order modeling of a variable-density mixing layer. *J. Fluid Mech.* 180, 93-116.

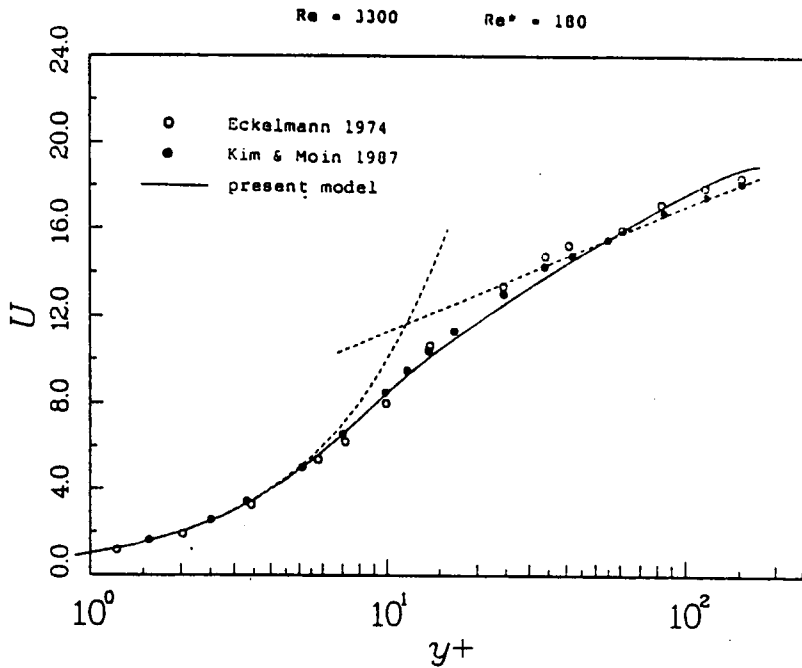


FIGURE 1. Mean velocity profile in a channel as predicted by a two-equation model.

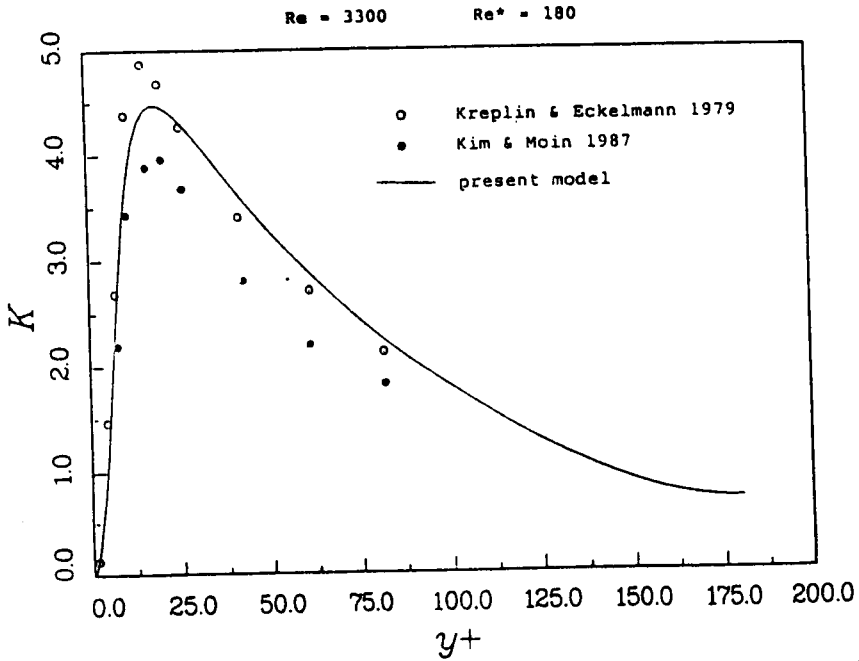


FIGURE 2. Mean turbulent kinetic energy in the channel as predicted by a two-equation model.

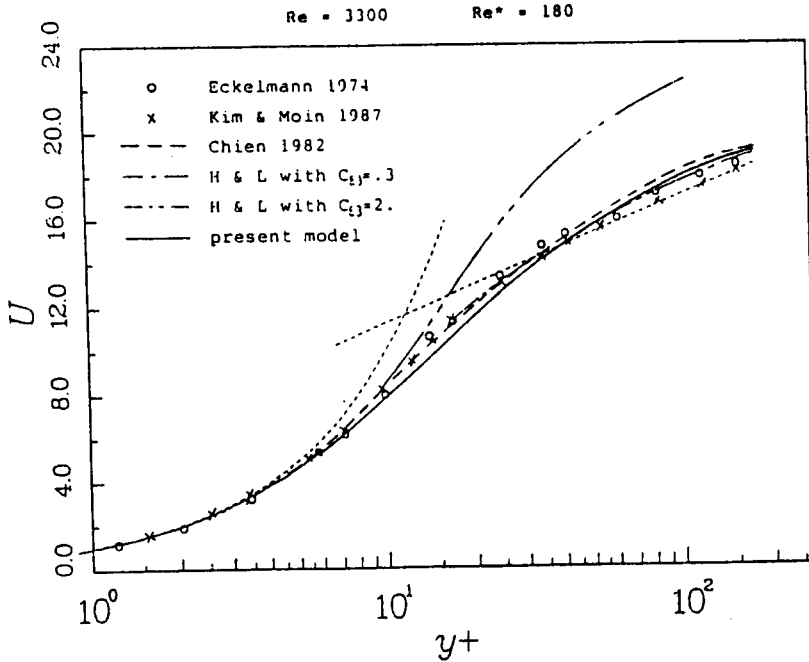


FIGURE 3. Mean velocity profile in a channel as predicted using a Reynolds stress model.

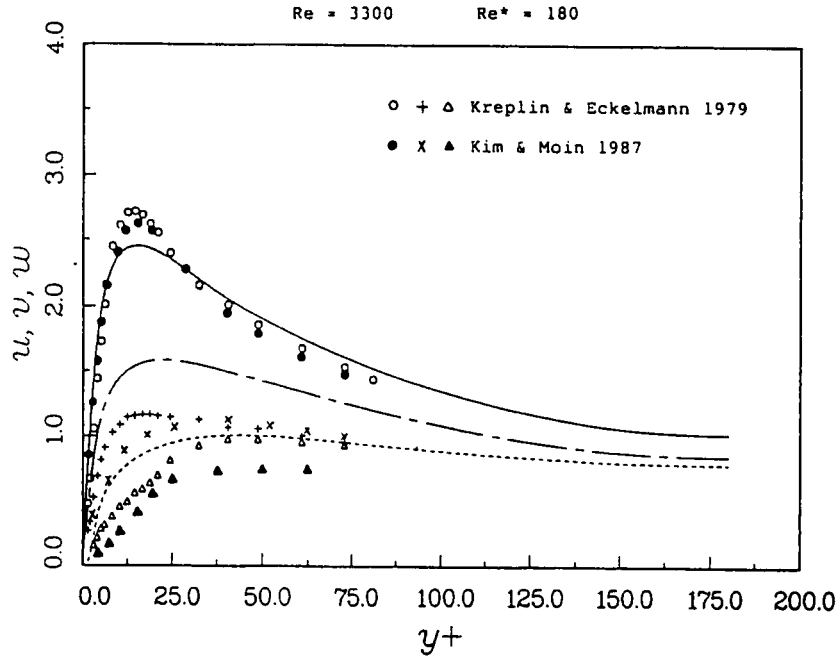


FIGURE 4. Normal stress in a channel as predicted using a Reynolds stress model.

On curve and surface stretching in turbulent flow

By N. ETEMADI¹

Cocke (1969) proved that in incompressible, isotropic turbulence the average material line (material surface) elements increase in comparison with their initial values. We obtain rigorously, among other things, good estimates of how much they increase in terms of the eigenvalues of the Green deformation tensor.

Introduction

In the following note we will study deformation of material curves and surfaces convected in a turbulent flow. We will do this by looking at the notion of material line and surface elements as a means of generating hypotheses for the so called *flow path (Lagrangian)* of the motion. Then we will use these hypotheses to obtain upper and lower bounds for the evolution of the *ensemble average* of the arc length (surface area) of an arbitrary curve (surface) in time.

For the definition of material line and surface elements and their historical background see Monin and Yaglom (1975). Cocke (1969) is the first who generated these mathematical assumptions, see section 1.1, "implicitly" and gave a convincing proof of them for isotropic turbulence. Orszag (1970, 1977) takes these assumptions for granted, and by a variant of Cocke's arguments obtains somewhat weaker results than Cocke's, see Remark 1.2. Our work *complements* the work of Cocke. Namely, we will bring out these assumptions in section 1, and we will show, first, that once one accepts these assumptions then Cocke's (1969) results can be improved to obtain "tight" upper and lower bounds for the ensemble average of material lines and surfaces. Then, in the remaining part of section 1 and in section 2 we carry on the results to arbitrary curves and surfaces, and in turn we also obtain upper bounds for moments of the dispersion between two points moving in the flow at any given time in terms of their separation at initial time.

Throughout our work we will use $x(a, t)$ as the Lagrangian representation of the flow, i.e. the trajectory followed by the particle which is at a at initial time t_0 . We will assume that x is smooth enough in a space-time region and is, for fixed t , an invertible mapping so that our manipulations are legitimate. We will also use $|v|$ as the magnitude of an arbitrary vector v , whose components, without danger of confusion, will be denoted by v_1, v_2 , and v_3 .

¹ University of Illinois at Chicago

1. Curve Stretching

The motion of an infinitesimal material line δl is governed by the equation

$$\frac{d\delta l}{dt} = (\delta l \cdot \nabla)u \quad \text{or} \quad \frac{d\delta l}{dt} = \sum_{j=1}^3 u_{,j} \delta l_j, \quad (1)$$

with $\delta l(t_0) = \delta^0 l$. Where $\frac{d}{dt}$ is the material derivative following the motion, see e.g. Monin and Yaglom (1975) section 24.5. It is easy to check that the above equation has the solution,

$$\delta l = \sum_{k=1}^3 x_{,k} \delta^0 l_k \quad ; \quad x(a, t_0) = a, \quad (x_{i,j}(a, t_0)) = (\delta_{ij}) = I, \quad (2)$$

where I is the identity matrix.

Let $\rho(a, t)$ be the Lagrangian density. It is easy to show that

$$\det(x_{i,j}(a, t)) = \frac{\rho(a, t_0)}{\rho(a, t)} = \frac{\rho_0}{\rho_t}, \quad (3)$$

where the left hand side is the determinant of the Jacobian matrix (or the Jacobian) of the transformation $y = x(a, t), t > t_0$, see Batchelor (1977) p.79. In particular, the Jacobian is one when the flow is incompressible.

Next consider

$$|\delta l|^2 = \delta^0 l^T (x_{i,j})^T (x_{i,j}) \delta^0 l = \delta^0 l^T W \delta^0 l. \quad (4)$$

Clearly W is a symmetric non-negative definite matrix. Since its determinant is $(\rho_0/\rho_t)^2$, consequently its eigenvalues, say w_1, w_2, w_3 , are strictly positive and we have

$$\det(W) = \det(X_{i,j})^2 = w_1 w_2 w_3 = \frac{\rho_0^2}{\rho_t^2}. \quad (5)$$

Let $A = (a_{ij})$ be the unitary (rotation) matrix corresponding to diagonalization of W . Thus $|A\delta^0 l| = |\delta^0 l|$. We can rewrite,

$$\begin{aligned} \frac{|\delta l|^2}{|\delta^0 l|^2} &= w_1 \frac{(A\delta^0 l)_1^2}{|A\delta^0 l|^2} + w_2 \frac{(A\delta^0 l)_2^2}{|A\delta^0 l|^2} + w_3 \frac{(A\delta^0 l)_3^2}{|A\delta^0 l|^2} \\ &= (\sin^2 \theta \cos^2 \psi) w_1 + (\sin^2 \theta \sin^2 \psi) w_2 + (\cos^2 \theta) w_3, \end{aligned} \quad (6)$$

where θ, ψ are the usual spherical coordinates of the unit vector $\frac{A\delta^0 l}{|A\delta^0 l|}$.

Now we are in a position to take ensemble averages of both sides of this equation. To do so, we need to make some assumptions about the joint probability

distribution of the variables involved; namely w_i 's, θ and ψ . This is where the physics of the problem come in. The following three assumptions have been extracted from the work of Cocke (1969) who proved them to be true for incompressible, isotropic turbulence.

Assumptions;

- (1) w_i 's are independent of θ and ψ ,
- (2) θ and ψ are uniformly distributed over the unit sphere,
- (3) w_i 's are identically distributed.

Assumption one implies that the random orientation of the element δl is uncorrelated with its random deformations along the principal axis. Assumption two simply says that δl is equally likely to be oriented in any direction. Finally, assumption three means that the random deformations of δl along its principal axis have the same probability law.

Proposition 1.1. Under Assumptions (1) and (2) we have,

$$\frac{1}{3} \langle \sqrt{w_1} + \sqrt{w_2} + \sqrt{w_3} \rangle \leq \langle \frac{|\delta l|}{|\delta^0 l|} \rangle \leq \frac{1}{2} \langle \sqrt{w_1} + \sqrt{w_2} + \sqrt{w_3} \rangle, \quad (i)$$

$$\frac{1}{2} \langle (w_1 + w_2 + w_3)^{\frac{1}{2}} \rangle \leq \langle \frac{|\delta l|}{|\delta^0 l|} \rangle \leq \langle (w_1 + w_2 + w_3)^{\frac{1}{2}} \rangle. \quad (ii)$$

Proof. Since \sqrt{x} is concave and the coefficients of w_i 's add up to one, from (6) and (19) we obtain,

$$\frac{|\delta l|}{|\delta^0 l|} \geq (\sin^2 \theta \cos^2 \psi) \sqrt{w_1} + (\sin^2 \theta \sin^2 \psi) \sqrt{w_2} + (\cos^2 \theta) \sqrt{w_3}. \quad (7)$$

Also it is clear from (6) that,

$$\frac{|\delta l|}{|\delta^0 l|} \leq |\sin \theta \cos \psi| \sqrt{w_1} + |\sin \theta \sin \psi| \sqrt{w_2} + |\cos \theta| \sqrt{w_3}. \quad (8)$$

Next, use the joint density function of θ and ψ , i.e. $\frac{1}{4\pi} \sin \theta$ $0 \leq \theta \leq \pi$, $0 \leq \psi \leq 2\pi$, to conclude that the average of the coefficients of w_i 's and their square roots, in (6), are $\frac{1}{3}$ and $\frac{1}{2}$, respectively, and this will in turn give us (i). Since the coefficient of w_i 's in (6) are bounded by one we are only left to show the left hand side of (ii). To see this note that again by the fact that \sqrt{x} is concave, from (6) and (19) we have,

$$\begin{aligned} \frac{|\delta l|}{|\delta^0 l|} &= (w_1 + w_2 + w_3)^{\frac{1}{2}} \left[\frac{(\sin^2 \theta \cos^2 \psi) w_1 + (\sin^2 \theta \sin^2 \psi) w_2 + (\cos^2 \theta) w_3}{w_1 + w_2 + w_3} \right]^{\frac{1}{2}} \\ &\geq (w_1 + w_2 + w_3)^{\frac{1}{2}} \left[\frac{|\sin \theta \cos \psi| w_1 + |\sin \theta \sin \psi| w_2 + |\cos \theta| w_3}{w_1 + w_2 + w_3} \right]. \end{aligned} \quad (9)$$

Now the average of the coefficient of w_i 's in the above line is $\frac{1}{2}$ and we are through by Assumption (1).///

Proposition 1.2. Under Assumptions (1) and (2) and/or (1) and (3) we have,

$$\frac{1}{3}\langle w_1^{\frac{p}{2}} + w_2^{\frac{p}{2}} + w_3^{\frac{p}{2}} \rangle \leq \langle \left(\frac{|\delta l|}{|\delta^0 l|} \right)^p \rangle \leq \langle w_1^{\frac{p}{2}} + w_2^{\frac{p}{2}} + w_3^{\frac{p}{2}} \rangle \text{ for } 0 < p < 2, \quad (i)$$

$$\langle \frac{|\delta l|^2}{|\delta^0 l|^2} \rangle = \frac{1}{3}\langle w_1 + w_2 + w_3 \rangle \text{ for } p = 2, \quad (ii)$$

$$\langle \frac{w_1^{\frac{1}{2}} + w_2^{\frac{1}{2}} + w_3^{\frac{1}{2}}}{3} \rangle^p \leq \langle \left(\frac{|\delta l|}{|\delta^0 l|} \right)^p \rangle \leq \langle \frac{w_1^{\frac{p}{2}} + w_2^{\frac{p}{2}} + w_3^{\frac{p}{2}}}{3} \rangle \text{ for } 2 < p < \infty, \quad (iii)$$

$$\frac{1}{6}\langle \log(w_1 w_2 w_3) \rangle \leq \langle \log\left(\frac{|\delta l|}{|\delta^0 l|} \right) \rangle. \quad (iv)$$

Proof. In light of what we have said in the proof of the above proposition, (ii) is immediate under Assumptions (1) and (2). Now we can conclude (ii) by utilizing Assumptions (1) and (3) in (6) to obtain,

$$\begin{aligned} \langle \frac{|\delta l|^2}{|\delta^0 l|^2} \rangle &= \langle \sin^2 \theta \cos^2 \psi \rangle \langle w_1 \rangle + \langle \sin^2 \theta \sin^2 \psi \rangle \langle w_2 \rangle + \langle \cos^2 \theta \rangle \langle w_3 \rangle. \\ &= \langle \sin^2 \theta \cos^2 \psi + \sin^2 \theta \sin^2 \psi + \cos^2 \theta \rangle \langle w_1 \rangle = \langle w_1 \rangle \\ &= \frac{1}{3}\langle w_1 + w_2 + w_3 \rangle. \end{aligned} \quad (10)$$

The left hand side of (i) and the right hand side of (iii) follow from an inequality like the one given in (7). \sqrt{x} should be replaced by $x^{\frac{p}{2}}$, and the direction of the inequality should be reversed due to convexity when $p > 2$. The right hand side of (i) is trivially true and the left hand side of (iii) is a consequence of $\langle \frac{|\delta l|}{|\delta^0 l|} \rangle^p \leq \langle \left(\frac{|\delta l|}{|\delta^0 l|} \right)^p \rangle$, $p \geq 1$, see (18), and the right hand side of (i) for $p = 1$.

Finally to obtain (iv) use the concave function $\log(x)$ rather than \sqrt{x} in (7) under Assumption (1) and (2), and an argument similar to the one given at (10) under Assumption (1) and (3).///

Remark 1.1. Note that the left hand side inequalities in the above propositions are strict unless $w_1 = w_2 = w_3$. For all the concave functions involved are strictly increasing. Clearly this happens only when W is the identity matrix, meaning pure rotation. Furthermore, this has to be the case with probability one in order to have equality in the above propositions, which is certainly not an interesting case.

Corollary 1.1. (Cocke). For an isotropic incompressible turbulence,

$$\langle \log \frac{|\delta l|}{|\delta^0 l|} \rangle > 0, \quad \langle \frac{|\delta l|^p}{|\delta^0 l|^p} \rangle > 1,$$

for any $p > 0$.

Proof. Cocke (1969) gives an a priori proof to the effect that the Assumption (1) to (3) are true for isotropic incompressible flow. This invokes the above proposition and together with Remark 1.1 and the fact that $\det(x_{i,j}) = 1$, see (3), we obtain the first inequality. The second one follows from (18), and the one we have just established as follows;

$$\langle \frac{|\delta l|^p}{|\delta^0 l|^p} \rangle = \exp[\log \langle \frac{|\delta l|^p}{|\delta^0 l|^p} \rangle] \geq \exp[\langle \log \frac{|\delta l|^p}{|\delta^0 l|^p} \rangle] = \exp[p \langle \log \frac{|\delta l|}{|\delta^0 l|} \rangle] > 1. \quad (11)$$

We could have also used the arithmetic geometric mean inequality, $(w_1^r + w_2^r + w_3^r)/3 \geq \sqrt[3]{(w_1 w_2 w_3)^r}$, to achieve the same end.///

Remark 1.2. The proof of the Assumptions (1) to (3) is the thrust of the work in Cocke (1969) in which he has also shown Proposition 1.2 (ii) and (iv), the above remark and corollary by using the same argument. Orszag (1970) takes these assumptions for granted, follows Cocke's argument and obtains a weaker result, $\langle \frac{|\delta l|^2}{|\delta^0 l|^2} \rangle > 1$, see the above corollary for $p = 2$. Note that this result *does not imply* that the average material line stretches. Now if we agree on all three assumptions, then it is trivial to show that $\langle W \rangle = \gamma(\delta_{i,j})$; where γ is the right hand side of (ii) in Proposition 1.2. In this connection see also Orszag (1977), p.240-241.

Next we extend the above results to an arc length following the flow. The statement of the inequalities needed to carry this on can be found in the appendix. Let $C(s; t_0) : [a, b] \rightarrow \mathbb{R}^3$ be a parametric representation of a *non-random* curve at time t_0 . Then $C(s; t) = x(C(s; t_0), t)$ is the corresponding *random curve*, following the flow at time t . Let C_{t_0} and C_t , $t \geq t_0$ be their arc lengths, respectively. For homogenous turbulence define,

$$\alpha(t) = \langle \frac{\sqrt{w_1} + \sqrt{w_2} + \sqrt{w_3}}{3} \rangle \leq \beta(t) = \langle \sqrt{\frac{w_1 + w_2 + w_3}{3}} \rangle, \\ \leq \gamma(t) = \sqrt{\langle \frac{w_1 + w_2 + w_3}{3} \rangle},$$

where the first and second inequalities are the consequence of (19) and (18) respectively.

Theorem 1.1. For an isotropic, incompressible flow,

$$C_{t_0} \leq \exp\{\langle \log(C_t) \rangle\} \leq \langle C_t \rangle \leq \gamma(t) C_{t_0}, \quad (i)$$

$$C_{t_0} \leq \alpha(t) C_{t_0} \leq \langle C_t \rangle \leq \frac{3}{2} \alpha(t) C_{t_0}, \quad (\text{ii})$$

$$\frac{\sqrt{3}}{2} \beta(t) C_{t_0} \leq \langle C_t \rangle \leq \sqrt{3} \beta(t) C_{t_0}. \quad (\text{iii})$$

Proof. The above corollary implies that for the non-random vector $\delta^0 l = C'(s; t_0)$,

$$\langle \log(|\sum_{k=1}^3 x_k C'_k(s; t_0)|) \rangle = \langle \log(|\delta l|) \rangle \geq \log(|\delta^0 l|) = \log(|C'(s; t_0)|). \quad (12)$$

Consequently,

$$\begin{aligned} \exp\{\langle \log(C_t) \rangle\} &= \exp\{\langle \log\left(\int_a^b \left|\frac{\partial C(s; t)}{\partial s}\right| ds\right) \rangle\} \\ (\text{by (20), } S_1 = [a, b]) &\geq \int_a^b \exp\{\langle \log\left(\left|\frac{\partial C(s; t)}{\partial s}\right|\right) \rangle\} ds \\ &= \int_a^b \exp\{\langle \log(|\sum_{k=1}^3 x_k(C(s; t_0), t) C'_k(s; t_0)|) \rangle\} ds \quad (13) \\ (\text{by (12)}) &\geq \int_a^b \exp\{\log(|C'(s; t_0)|)\} ds \\ &= \int_a^b |C'(s; t_0)| ds = C_{t_0}. \end{aligned}$$

Next, inequality in (i) is an immediate consequence of (18) with $\phi = \exp(x)$. The following one is true by virtue of (18) with $\phi = \sqrt{x}$, and Proposition 1.2 (ii). For the rest of the inequalities all we need is Proposition 1.1.///

Remark 1.3. Since in an inviscid flow vortex lines remain vortex lines, the above theorem is an statement about their evolution in time when the flow is isotropic and incompressible. The same is also true for vortex sheets which will follow from the discussion in section 2.

Remark 1.4. The reason for presenting various upper and lower bounds is for their potential in applications. For instance, with regard to the above remark and under the same conditions, one can compute $\gamma^2(t)$ as the ratio of the enstrophy at time t to time t_0 .

Proposition 1.2 will give us "tight" upper and lower bounds for $\langle \int_a^b \left|\frac{\partial C(s; t)}{\partial s}\right|^p ds \rangle$ in an obvious way. This can be used partially to get information about the moments of C_t .

Theorem 1.2. For an isotropic, incompressible flow, let $\alpha_p(t) = \langle w_1^{\frac{p}{2}} + w_2^{\frac{p}{2}} + w_3^{\frac{p}{2}} \rangle / 3$. Then, for $p > 0$,

$$(C_{t_0})^p \leq \langle (C_t)^p \rangle \quad (i)$$

for $0 < p \leq 1$,

$$\alpha_p(t) [\min_{s \in [0,1]} \{|C'(s; t_0)|^{p-1}\}] C_{t_0} \leq \langle (C_t)^p \rangle \leq \langle C_t \rangle^p \leq c_2^p (C_{t_0})^p \quad (ii)$$

for $p \geq 1$,

$$(C_{t_0})^p \leq c_1^p (C_{t_0})^p \leq \langle C_t \rangle^p \leq \langle (C_t)^p \rangle \leq 3\alpha_p(t) [\max_{s \in [0,1]} \{|C'(s; t_0)|^{p-1}\}] C_{t_0} \quad (iii)$$

where c_2 (c_1) is the minimum (maximum) of the coefficients of C_{t_0} in the upper (lower) bounds for $\langle C_t \rangle$ in Theorem 1.1, and without loss of generality, we have assumed $[a, b] = [0, 1]$.

Proof. The easiest way to handle (i) is to raise the left hand side of (i) in Theorem 1.1 to power p , take p inside the \log , and then use (18) with $\phi = \exp(x)$. The left hand side of (ii) and the right hand side of (iii) are also the cosequences of (18) with $\phi = x^p$ in an obvious way, and the remaining parts are easily followed by Theorem 1.1.///

The next corollary will give us information about the moments of evolution of a straight line segment in turbulent flow and also the moments of dispersion of two points as time goes on.

Corollary 1.2. Let $d_1 = \min[c_1^p, \alpha_p(t)]$, $d_2 = \max[c_2^p, 3\alpha_p(t)]$ with c_1, c_2 and $\alpha_p(t)$ as in the above theorem. Let $C(s; t_0) = a_1 + s(a_2 - a_1)$, $s \in [0, 1]$. Then for an isotropic, incompressible turbulence,

$$d_1 |a_2 - a_1|^p \leq \langle (C_t)^p \rangle \leq d_2 |a_2 - a_1|^p \quad \text{for } p > 0, \quad (i)$$

$$\langle |x(a_2, t) - x(a_1, t)|^p \rangle \leq d_2 |a_2 - a_1|^p \quad \text{for } p > 0. \quad (ii)$$

Proof. Note that $|\frac{\partial C(s; t)}{\partial s}| = |a_2 - a_1|$ and use the above theorem.///

2. Surface Stretching

In this section we will extend the above results to the evolution of a surface area in turbulent flow. It turns out, just as in the work of Cocke (1969), that only minor modifications are needed to do so.

Let $\delta^0 l$ and $\delta^0 k$ be two infinitesimal material line at $t = t_0$. We can form an infinitesimal material surface by taking the vector product of these vectors, i.e. $\delta^0 S = \delta^0 l \times \delta^0 k$. This at time t becomes,

$$\delta S = \delta l \times \delta k = \left(\sum_{j=1}^3 X_{,j} \delta^0 l_j \right) \times \left(\sum_{j=1}^3 X_{,j} \delta^0 k_j \right). \quad (14)$$

Let the matrices W , A and the eigenvalues, w_i 's, of W , be as before. From the identity,

$$|v_1 \times v_2|^2 = |v_1|^2 |v_2|^2 - (v_1 \cdot v_2)^2, \quad (15)$$

for any given vectors v_1 and v_2 and the fact that $|\delta^0 S|^2 = |A\delta^0 l \times A\delta^0 k|^2$, A being unitary, we can easily obtain,

$$\begin{aligned} \frac{|\delta S|^2}{|\delta^0 S|^2} &= w_2 w_3 \frac{(A\delta^0 l \times A\delta^0 k)_1^2}{|A\delta^0 l \times A\delta^0 k|^2} + w_1 w_3 \frac{(A\delta^0 l \times A\delta^0 k)_2^2}{|A\delta^0 l \times A\delta^0 k|^2} + w_1 w_2 \frac{(A\delta^0 l \times A\delta^0 k)_3^2}{|A\delta^0 l \times A\delta^0 k|^2} \\ &= (\sin^2 \theta \cos^2 \psi) w_2 w_3 + (\sin^2 \theta \sin^2 \psi) w_1 w_3 + (\cos^2 \theta) w_1 w_2. \end{aligned} \quad (16)$$

Now (16) plays the role of (6), and we only need to modify Assumption (3) as follows;

Assumption;

(4) $w_1 w_2, w_1 w_3$ and $w_2 w_3$ are identically distributed. (Note that Assumptions (3) and (4) are equivalent for incompressible flows.)

Now all we need to do is to replace w_1, w_2, w_3 by $w_2 w_3, w_3 w_1, w_1 w_2$; $\delta l, \delta^0 l$ by $\delta S, \delta^0 S$, and C_t, C_{t_0} by S_t, S_{t_0} , and $[a, b]$ by D , respectively, in the above results, including the remarks, to obtain the new ones corresponding to surfaces. Where we let $S(u, v; t_0)$ be a parametric representation of a *nonrandom* surface on a region D on the plain, S_{t_0} be its area, and,

$$S_t = \int \int_D \left| \frac{\partial x(S(u, v; t_0), t)}{\partial u} \times \frac{\partial x(S(u, v; t_0), t)}{\partial v} \right| du dv, \quad (17)$$

the area at time t .

The only *nonsymbolic* modification of the proofs are: (a) In Theorem 1.2 the area of D has to be one or otherwise the right (left) hand side of (iii) ((ii)) has to be multiplied by that area to the power $p - 1$ due to the correct usage of Jensen's inequality; (b) In Corollary 1.2 the notion of a distance between two points has to be replaced by an area of a region on a *plane* and its left hand side of (ii) to be interpreted correctly.

Remark 2.1 We could have always used Proposition 1.2 and its counterpart for surfaces to obtain upper and lower bounds for moments of material lines, material surfaces, arc lengths, and surface areas at the expense of having different *constants*. Compare Proposition 1.1 with Proposition 1.2 when $p = 1$. The difference between these two propositions becomes significant if one can realize physically non-isotropic incompressible flows that satisfy only one pair of the assumptions, involved in these propositions, rather than all of them. Finally, for analogous results concerning homogeneous turbulence we invite the reader to consult Corrsin (1972).

Appendix

(Jensen's Inequality) Let X be a random variable and ϕ a convex (concave) function containing the range of X . Assume both X and $\phi(X)$ have ensemble averages, then

$$\phi(\langle X \rangle) \leq (\geq) \langle \phi(X) \rangle. \quad (18)$$

Proof. See any standard graduate textbook in probability theory or measure theory e.g. Billingsley (1986) p.283.

The following special case of Jensen's inequality has been used frequently; let p_1, p_2 , and p_3 be three positive numbers whose total sum is one, let a_1, a_2 , and a_3 be any real numbers. Then with ϕ as above we have,

$$\phi\left(\sum_{i=1}^3 p_i a_i\right) \leq (\geq) \sum_{i=1}^3 p_i \phi(a_i). \quad (19)$$

Proof. Let X in (18) be the random variable which takes the value a_i with probability p_i , $i = 1, 2, 3$.//

(Dunford and Schwartz[5], p.535). Let (S, Σ, μ) and (S_1, Σ_1, μ_1) be positive measure spaces. Assume $\mu(S) = 1$. Then if K is a $\mu \times \mu_1$ - measurable function defined on $S \times S_1$,

$$\int_{S_1} \exp\left\{\int_S \log|K(s, s_1)|\mu(ds)\right\}\mu_1(ds_1) \leq \exp\left\{\int_S \left[\log\left(\int_{S_1} |K(s, s_1)|\mu_1(ds_1)\right)\right]\mu(ds)\right\}. \quad (20)$$

REFERENCES

- BATCHELOR, G. K. 1977 *An Introduction to Fluid Dynamics*. Cambridge University Press.
- BATCHELOR, G. K. 1952 Proc. Roy. Soc. (London) A213, 349.
- BILLINGSLEY, P. 1986 Probability and measure. Wiley- interscience pub., New York.
- COCKE, W. J. 1969 *The Physics of Fluids* 12, 2488.
- CORRSIN, S. 1972 *The Physics of Fluids* 15, 1370.
- DUNFORD, N. & SCHWARTZ, J. T. 1958 *Linear Operators. Part I*. Interscience pub., New York.
- MONIN, A. S. & YAGLOM A. M. 1975 *Statistical fluid mechanics. Vol. II*. The MIT Press.
- ORSZAG, S. A. 1970 *The Physics of Fluids* 13, 2203.
- ORSZAG, S. A. 1977 Fluid Dynamics. Gordon and Beach Sci.Pub.

Renormalization group analysis of turbulence

By L. M. SMITH

1. Objective

The objective is to understand and extend a recent theory of turbulence based on dynamic renormalization group (RNG) techniques. The application of RNG methods to hydrodynamic turbulence has been explored most extensively by Yakhot and Orszag (1986). They calculate an eddy viscosity consistent with the Kolmogorov inertial range by systematic elimination of the small scales in the flow. Further, assumed smallness of the nonlinear terms in the redefined equations for the large scales results in predictions for important flow constants such as the Kolmogorov constant. The authors emphasize that no adjustable parameters are needed. The parameterization of the small scales in a self-consistent manner has important implications for sub-grid modeling.

2. The RNG Transformation

Renormalization group methods were first developed for quantum field theories. They were later applied to the theory of critical points in materials that undergo phase transitions (Ma, 1976). Predictions for the universal exponents characterizing the behavior of thermodynamic quantities near critical points are quite accurate. The common feature of the physical phenomena amenable to RNG analysis is a lack of characteristic length and time scales.

The lack of characteristic length and time scales in turbulence makes RNG methods attractive. The universality of the inertial range spectrum in widely varying turbulent flows is also suggestive.

The RNG transformation consists of two steps. First, small scales are eliminated by an averaging procedure. Second, space is rescaled. New independent variables are defined on the original intervals by the rescaling. In most cases, the dependent variables must also be rescaled.

A set of equations is renormalizable if it is unchanged by the RNG transformation. Renormalizability implies scale invariance. Usually a set of equations is renormalizable only for specific values of its coefficients and the scaling parameters. These points are called fixed points. However, the physics of more general cases is often well described by the physics at a fixed point.

The method of attack is to iterate the RNG transformation of the equations. With each transformation the coefficients in the equations change. One looks for a situation in which this iteration procedure converges.

In addition to redefining coefficients of existing terms, the scale elimination often generates terms of different form than those in the original equations.

These new terms can be classified as irrelevant, marginal or relevant according to whether they decay, are constant or grow when rescaled. One can ask if a fixed point exists in the absence of new terms. If so, all new terms must be irrelevant for the system to be truly renormalizable at that point.

3. The Basic Premise of the RNG Analysis of Turbulence

The theory is based on the postulated equivalence between inertial range solutions of the Navier Stokes equations subject to initial and boundary conditions, and homogeneous isotropic flow driven by a Gaussian random force (Forster et. al., 1977, Yakhot and Orszag, 1986). The model equations are then

$$\frac{\partial \mathbf{v}}{\partial t} + (\mathbf{v} \cdot \nabla) \mathbf{v} = \mathbf{f} - \frac{1}{\rho} \nabla P + \nu_o \nabla^2 \mathbf{v} \quad (1)$$

$$\nabla \cdot \mathbf{v} = 0 \quad (2)$$

where $\mathbf{v}(\mathbf{x}, t)$ is the velocity, P the pressure, ρ the density, ν_o the kinematic viscosity and \mathbf{f} the forcing. The domain of equations (1) and (2) is unbounded.

The white noise force is given by its correlation function in wavevector, frequency space. The correlation is assumed to obey a power law spectrum,

$$\langle f_i(\mathbf{k}, \omega) f_j(-\mathbf{k}, -\omega) \rangle \propto |\mathbf{k}|^{-y} \quad (3)$$

where the brackets indicate an ensemble average. The exponent y is chosen to give the inertial range energy spectrum. Once y is fixed, there are no adjustable parameters in the problem.

4. A Revised RNG Analysis

Yakhot and Orszag show that analysis of (1)-(3) using the full RNG transformation yields the scaling laws of velocity correlations, and thus the energy spectrum. If y is set equal to the number of dimensions, 3, the Kolmogorov spectrum is recovered: $E(k) \propto k^{-5/3}$ where $k = |\mathbf{k}|$. Amplitudes, however, are left undetermined.

By performing only the scale elimination, and abandoning the rescaling, they are able to find both scaling laws and amplitudes. Then $E(k) = K_{ORNG} \epsilon^{2/3} k^{-5/3}$, where ϵ is the dissipation rate and K_{ORNG} is the RNG prediction for the Kolmogorov constant.

Rescaling is used only to justify neglect of new terms generated by the elimination procedure. The terms of concern are cubic in the velocity vector and are marginal with respect to the fixed point found in their absence. One wonders how the results would change if the cubic terms are retained. A goal of the present research is to assess the effect of these terms on the system.

5. The Effect of the Small Scales

The theory developed by Yakhot and Orszag is an attempt to calculate the effect of the small scales on the large scales in turbulence. Their method determines that the large scales 'feel' the small scales as an eddy viscosity.

Equations (1) and (2) are written in wavevector, frequency space and the pressure is eliminated by taking the curl of the curl. The equations for the Fourier coefficients of the velocity field are then expanded in a power series via the introduction of an ordering parameter which multiplies the nonlinear term.

A narrow band of wavenumbers is removed by averaging over their force field. The averaging procedure replaces the contribution of the nonlinear interaction of those wavenumbers with a term linear in the velocity vector for the remaining wavenumbers. The nonlinear interaction is only approximately represented in this term. The approximation is due to truncation of the power series at second order and neglect of terms cubic in the velocity vector for the remaining wavenumbers.

The coefficient of the linear term is an integral. The integral is evaluated in the limit $0 \sim k \ll k_c$, where k_c is the low wavenumber cutoff of the eliminated band. In this limit the integral is proportional to k^2 . Thus the large scales see the small scales as (approximately) a viscous term.

Iteration of the elimination procedure produces an equation for the large scales and long times identical in form to equation (1). The molecular viscosity ν_o is replaced by an eddy viscosity,

$$\frac{\partial \mathbf{v}}{\partial t} + \bar{\lambda}(\mathbf{v} \cdot \nabla)\mathbf{v} = \mathbf{f} - \frac{\bar{\lambda}}{\rho} \nabla P + \nu_T \nabla^2 \mathbf{v} \quad (4)$$

where ν_T is the eddy viscosity and $\bar{\lambda}$ is the nondimensionalized ordering parameter. The eddy viscosity depends on k_c ,

$$\nu_T = \nu_o [1 + \beta^3 \epsilon (k_c^{-4} - k_d^{-4})]^{1/3} \quad (5)$$

where β is a function of $\bar{\lambda}$, k_c is the last eliminated wavenumber and k_d is the viscous cutoff. If one now takes the limit $k_c \sim k \sim 0$,

$$\nu_T \sim \beta \epsilon^{1/3} k^{-4/3}. \quad (6)$$

In this limit the 'renormalized' equation (4) has a fixed point, at which all subsequent analysis takes place.

6. Evaluation of Universal Flow Constants

The nondimensionalized ordering parameter $\bar{\lambda}$ is proportional to $(y + 1)^{1/2}$, where $-y$ is the power of k in the force correlation function (see (3)). Recall $y = 3$ for a Kolmogorov inertial range. Using $y = 3$, the fixed point value of $\bar{\lambda}$

is 11.5. However, the RNG results depend on the simultaneous extrapolation of $k_c \sim k \sim 0$ and y approaching -1.

The assumption of small $(y + 1)$ allows a power series expansion of the renormalized equations. The equation for the zeroth order velocity coefficient is the Langevin equation,

$$(-i\omega + \nu_T k^2) \bar{v}^{(0)}(\mathbf{k}, \omega) = \bar{f}, \quad (7)$$

where $\bar{v}(\mathbf{k}, \omega)$ is the Fourier amplitude, $\bar{v} = \bar{v}^{(0)} + \bar{\lambda} \bar{v}^{(1)} + \bar{\lambda}^2 \bar{v}^{(2)} + \dots$, k and ω are small, and ν_T is given by equation (6). The value of β at the fixed point, evaluated to zeroth order in $\bar{\lambda}$, is found to be $\beta = .493$.

Evaluation of the Kolmogorov constant follows a power series expansion at the fixed point of the energy equation (the equation for the two-point velocity correlations). The analysis is again for $k_c \sim k \sim 0$ with ν_T given by (6). When terms to lowest nontrivial order are retained, its value is found to be $K_{ORNG} = 1.617$ (Dannevik et. al., 1987).

The same scale elimination procedure can be performed on the equations for the advection of a passive scalar. The renormalized equations for the large scales are characterized by an eddy diffusivity. A power series expansion with $k_c \sim k \sim 0$ leads to a prediction for the Batchelor constant, Ba .

7. Goals

a. Further steps in the analysis remain to be understood. For example, the RNG $\kappa - \epsilon$ model leads to a prediction for the von Karman constant.

b. One would like to assess the importance of the neglected new terms generated by the scale elimination procedure. These terms are cubic in the transform coefficients of the velocity vector for the large scales.

c. An exploration of other forcing functions will be revealing.

i. We have already investigated the possibility of a non-white noise, power law spectrum. The force correlation is allowed to fall off with frequency and considered proportional to $k^{-y} \omega^{-b}$. We find that there is no positive value of b consistent with both dimensional analysis and a Kolmogorov energy spectrum.

ii. A completely satisfactory theory of turbulence should account for spatial intermittency. In the present RNG formulation, intermittency might be included by changing the statistics assumed for the forcing function.

d. It should be possible to extend the theory to flows other than homogeneous, isotropic turbulence. Perhaps one can do away with the artificial forcing for realizable kinds of turbulence.

e. Finally, the RNG sub-grid and $\kappa - \epsilon$ models should be tested.

REFERENCES

- DANNEVIK, P., YAKHOT, V. & ORSZAG, S. A. 1987 *Phys. Fluids* **30**, 2021.

- FORSTER, D., NELSON, D. R. & STEPHEN, M. J. 1977 *Physical Review A* **16**, 732.
- KRAICHNAN, R. H. 1987 *Phys. Fluids* **30**, 2400.
- MA, S. K. 1976 *Modern Theory of Critical Phenomena - Frontiers in Physics*, **46**.
- YAKHOT, V. & ORSZAG, S. A. 1986 *Journal of Scientific Computing* **1**, 3.

Low-dimensional chaos in turbulence

By J. A. VASTANO

Abstract

Direct numerical simulations are being performed on two different fluid flows in an attempt to discover the mechanisms underlying the transition to turbulence in each. The first system is Taylor-Couette flow; the second, two-dimensional flow over an airfoil. Both flows exhibit a gradual transition to high-dimensional turbulence through low-dimensional chaos. The hope is that the instabilities leading to chaos will be easier to relate to physical processes in this case, and that the new understanding of these mechanisms can then be applied to a wider array of turbulent systems.

In the past decade a new understanding of nonlinear processes in nature has been provided by the application of mathematical ideas on chaos and bifurcation theory (Ott 1981, Swinney 1983). An important result for turbulence researchers has been the finding that some systems undergo a transition to turbulence by first becoming low-dimensionally chaotic (Brandstater and Swinney 1987, Keefe 1987, Sreenivasan 1985). Turbulence models should benefit from a better understanding of weakly turbulent cases in which low-dimensional models can in principle capture *all* of the system dynamics.

The purpose of this research project is to study instability mechanisms in two model cases that have exhibited a gradual transition to turbulence, i. e., a transition to turbulence via low-dimensional chaos. The hope is that the instabilities leading to chaos will be easier to relate to physical processes in these models, and that the new understanding of these mechanisms can then be applied to a wide array of turbulent systems.

The first of the two projects, undertaken with the advice and assistance of Drs. Robert Moser (NASA-Ames) and Lawrence Keefe (CTR), is the computation of the Lyapunov exponent spectrum for a model of Taylor-Couette flow, the flow between concentric rotating cylinders (Brandstater and Swinney 1987, Moser 1983). Experiments on moderate aspect ratio Taylor-Couette systems have observed a transition from laminar, time-independent Couette flow to periodic, quasiperiodic, and finally to low-dimensional chaotic motion. The physical mechanisms driving the low-order transitions have been found, but the transition to chaos is not well understood. The numerical method that we will use was developed by Moser (1983) to study curved channel flow and assumes axial periodicity. The method recovers the low-order transitions well, but the

axial constraint may significantly affect the chaotic states. The experimental evidence in the chaotic regime includes measurements of wavespeeds associated with dominant frequency components in the flow as well as estimates of the fractal dimension for the chaotic attractor. We can, therefore, verify the accuracy of our simulation: the wavespeeds can be measured just as they are in experiment, and the fractal dimension can be computed directly from a knowledge of the Lyapunov exponent spectrum for the flow (Keefe 1987). If our numerical results differ greatly from the experimental results on wavespeed, we may need to consider a finite axial extent model. Given an good numerical model of the flow, our dimension estimate will be more accurate (as accurate as computer resources allow) than dimension estimates obtained indirectly from experimental time series data.

Although the dimension estimate we obtain from the Lyapunov exponent spectrum is necessary to validate the model (or, perhaps, the experiment), there is a great deal more to be learned from the exponents. The Lyapunov exponents for a system measure the exponential rates of growth or decay for infinitesimal perturbations in each phase space direction. There are, therefore, an infinite number of Lyapunov exponents for any spatially-extended system, but for dissipative systems almost all of the exponents are large and negative, signifying the decay of transients to some attractor. The number of positive Lyapunov exponents is a rough indication of the number of distinct mechanisms destabilizing the flow. Moreover, the time-varying contributions to the long-time average exponents will indicate *when* in the system evolution the chaos-generating mechanisms are operating. The spatial structure of the eigenvectors associated with the positive Lyapunov exponents at those times may indicate the nature of that mechanism by showing *where* in the flow it is operating.

Progress on this work since 1 Sept 1988 includes familiarization with the NAS operating environment and the Vectoral programming language, and full implementation of the curved channel code on the Cray 2. The additions to the code necessary to compute the Lyapunov exponents have been inserted and tested on periodic and quasiperiodic Taylor vortex flow. The basic code (without the exponent calculations) is being run in order to estimate the minimum resolution needed to model chaotic Taylor-Couette flow. Moser's previous results showed, for example, that a $32 \times 16 \times 32$ ($R - \theta - Z$) simulation of a periodic (wavy Taylor vortex) flow reproduced the azimuthal wave speed found in experiments to within the experimental uncertainty. Lowering the resolution to $16 \times 16 \times 16$ only changes the wave speed by 1%, while a resolution of $16 \times 16 \times 8$ gives a 5% deviation. Moser attained good agreement with experiments on quasiperiodic (modulated wavy Taylor vortex) flows using a $64 \times 32 \times 64$ model. We are currently checking the effects of lowered resolution on this case. It seems likely that only moderately-high resolution will be needed for chaotic solutions at Reynolds numbers close to the quasiperiodic-chaotic transition.

A second, related research project is being conducted in collaboration with

Dr. Thomas Pulliam (NASA-Ames) (Pulliam 1989, Pulliam and Vastano). This is a study of the transition to turbulence in two-dimensional flow over airfoils at high angles of attack. Experiments on forced flow over airfoils have found that a transition to a chaotic state can be produced (Stuber and Gharib). Numerical simulations of two-dimensional unforced flow had found a transition for increasing Reynolds number from periodic flow to aperiodicity that included one period-doubling (Pulliam 1989). We have now seen a period-doubling cascade of bifurcations and a transition to low-dimensional chaos past a period-doubling accumulation point. We are currently attempting to characterize the observed chaos using Poincaré sections and Lyapunov exponent estimates from time series data. As in the Taylor-Couette research, the goal here is to identify the physical mechanisms causing the period-doubling to chaos, rather than simply establishing that such a transition exists.

REFERENCES

- OTT, E. 1981 *Rev. Mod. Phys.* **53**, 655.
- SWINNEY, H. L. 1983 *Physica* **7D**, 3.
- BRANDSTATER, A. & SWINNEY, H. L. 1987 *Phys. Rev. A* **35**, 2207.
- KEEFE, L., MOIN, P., & KIM, J. 1987 *Bull. APS* **32**, 2026.
- SREENIVASAN, K.R. 1985 in *Frontiers in Fluid Mechanics*, ed. S. H. Davis and J. L. Lumley (Springer, Berlin, 1985), p. 41.
- MOSER, R. D., MOIN, P., & LEONARD, A. 1983 *J. Comp. Phys.* **52**, 524.
- PULLIAM, T. 1989 presented at 27th AIAA Aerospace Sciences Meeting, Reno, Nevada, January.
- PULLIAM, T. & VASTANO, J. A. to be submitted to *J. Fluid Mechanics*.
- STUBER, K. & GHARIB, M., preprint.

Close interactions of 3D vortex tubes

By M. V. MELANDER¹

Abstract

The motivation for studying close vortex interactions is briefly discussed in the light of turbulence and coherent structures. Particular attention is given to the interaction known as reconnection. Two reconnection mechanisms are discussed. One is annihilation of vorticity by cross-diffusion, the other is an inviscid head-tail formation. At intermediate Reynolds numbers both mechanisms are operating.

1. Introduction

Close interaction and self-deformation of vortices are intriguing facets of fluid mechanics. These interactions occur repeatedly in turbulent flows. We can, therefore, expect that insight into fundamental vortex interactions will lead to a deeper understanding of turbulence. The theory of turbulence in 2D flows illustrates this point clearly. In 2D flows fundamental vortex interactions such as axisymmetrization, merger, and dipole formation provide the mechanisms for the emergence of large scale coherent structures (McWilliams 1984). These structures in turn invalidate earlier statistical theories based on random phases (Babiano et al 1987). Compared to 2D vortex dynamics, our understanding of three dimensional vortex interactions is in its infancy. In order to improve this level of understanding, it seems logical to begin by investigating the most basic vortex interactions. This report marks the beginning of a thorough investigation of such interactions.

We confine the study to unforced incompressible flows with no density variations and unbounded domains. Turbulence may then be viewed as a tangle of interacting vortices. This follows directly from the integral formulation of Navier-Stokes equations.

$$\mathbf{u}(\mathbf{r}) = \frac{1}{4\pi} \int \frac{\boldsymbol{\omega}(\mathbf{r}') \times (\mathbf{r} - \mathbf{r}')}{|\mathbf{r} - \mathbf{r}'|^3} d\mathbf{r}' + \nabla\phi \quad (1)$$

$$\boldsymbol{\omega} = \nabla \times \mathbf{u} \quad (2)$$

$$\frac{D\boldsymbol{\omega}}{Dt} = (\boldsymbol{\omega} \cdot \nabla)\mathbf{u} + \nu\Delta\boldsymbol{\omega} \quad (3)$$

¹ Permanent address: SMU, Texas

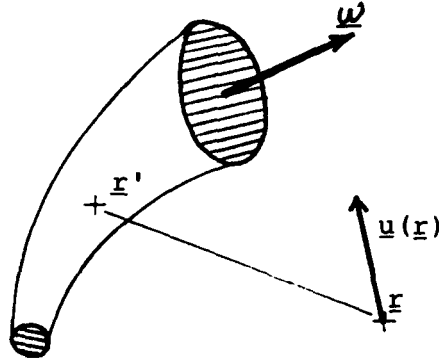


FIGURE 1. Schematic for the calculation of the velocity field $u(r)$ generated by a vortical structure.

When the fluid is at rest at infinity, the potential component in (1) vanishes. The Biot-Savart law (1) then shows that the vorticity governs the flow. The vorticity transport equation (3) in turn describes how the vorticity evolves with the flow. Some attractive features of the formulation (1) - (3) are: I) The irrotational part of the fluid does not appear in this description. This fact is the motivation behind computational methods known as "vortex methods" (Leonard 1985). Unfortunately, these methods make strong assumptions concerning the local vorticity distribution and may need further development before they can safely be used to investigate delicate vortex interactions. II) The description (1) - (3) appeals to our physical intuition. It is conceptually easy to give a qualitative prediction of the short time evolution of a given vorticity configuration by means of arm-waving and finger-twisting arguments. It is also possible to understand vortex dynamics in terms of primitive variables and force-balancing (Moore and Saffman 1972); although this approach leads to the same physical results, it seems considerably more complicated. III) A systematic description of how the small scale vortical structures influence the far-field $u(r)$ can be obtained from the Biot-Savart law (1).

Let us consider the last point in detail. Let a vorticity configuration be given near position r' (Figure 1). The Biot-Savart integral gives the velocity field $u(r)$ generated by this vorticity configuration at position r . The integration extends over the entire vorticity configuration. Clearly the integrand depends on r , so it is an enormous task to evaluate the integral for many different r positions. However, if $|r' - r|$ is large, we can expand the integrand in inverse powers of $|r' - r|$. The coefficients in this expansion are moments of the vorticity configuration and hence independent of r . These moments describe the shape and internal structure of the vorticity configuration. Far away, only the lowest order moment matters, but as we let r approach the vorticity configuration, an increasing number of moments must be included. We see that physical space moments yield a systematic description of internal structures influence on the

far-field. This idea has been used with success in 2D (Melander et al 1986).

The above discussion shows that the interaction between well separated vortices can be calculated efficiently in a straightforward manner. However, when $|\mathbf{r} - \mathbf{r}'|$ is small, we are faced with an entirely different situation. We no longer have a natural expansion parameter for the evaluation of the Biot-Savart integral. The integrable singularity in (1) tends to amplify the influence of the local structure. As a consequence, the local self-induced velocity can become very large for slender vortices. Such slender vortices can easily develop through vorticity stretching. A more subtle effect of small scale vorticity lies in its ability to alter neighboring large scale vortical structures. A concrete example from 2D is the axisymmetrization of a single isolated vortex (Melander et al 1987); here the small scale structures (filaments) influence the large scales in such a way as to make the vortex core circular symmetric. Because of these effects, we must treat the local vorticity structure and the associated small scales carefully. A thorough study of close vortex interactions via direct numerical simulations will, therefore, be most helpful for modelling of the local vorticity distributions and the associated small scales.

Vortex dynamics reveals its most useful role when viewed in the light of coherent structures. These vortical structures have been observed in many flows that were previously regarded as fully random (Hussain 1986). Often these large scale structures are superimposed by fluctuating vorticity (incoherent vorticity), which makes the structures less obvious, but not less important. In spite of the incoherent vorticity, the large structures still dominate the far-field. The incoherent vorticity does not influence the far-field directly, but can have an indirect influence by altering neighboring structures, as discussed above. Many interesting questions arise concerning the formation, persistence, characterization, topology, and interaction of coherent structures. Some of these questions are best approached through vortex dynamics. In this report we concentrate on interactions that can change the topology. These interactions are generally known as reconnections, although other names such as cut-and-connect, cross-linking, and fusion are also used. We examine a number of reconnection interactions under very idealized conditions. The interactions are simulated in isolation such that non-local effects do not obscure the dynamics. Also, there is no incoherent vorticity in our initial conditions.

2. Initial Conditions, Simulation Methods, and Diagnostics

The simulations were performed using a dealiased spectral (Galerkin) method with a fourth order predictor-corrector algorithm for the time advancement. This algorithm solves the Navier-Stokes equations (or the corresponding equations with superviscosity) in a cube with periodic boundary conditions. The evolution of a passive scalar at a unity Schmidt number is calculated simultaneously. The initial conditions (Figure 2a-f) were chosen as rectilinear vortices with a Gaussian vorticity profile. The evolution starting from the initial condition

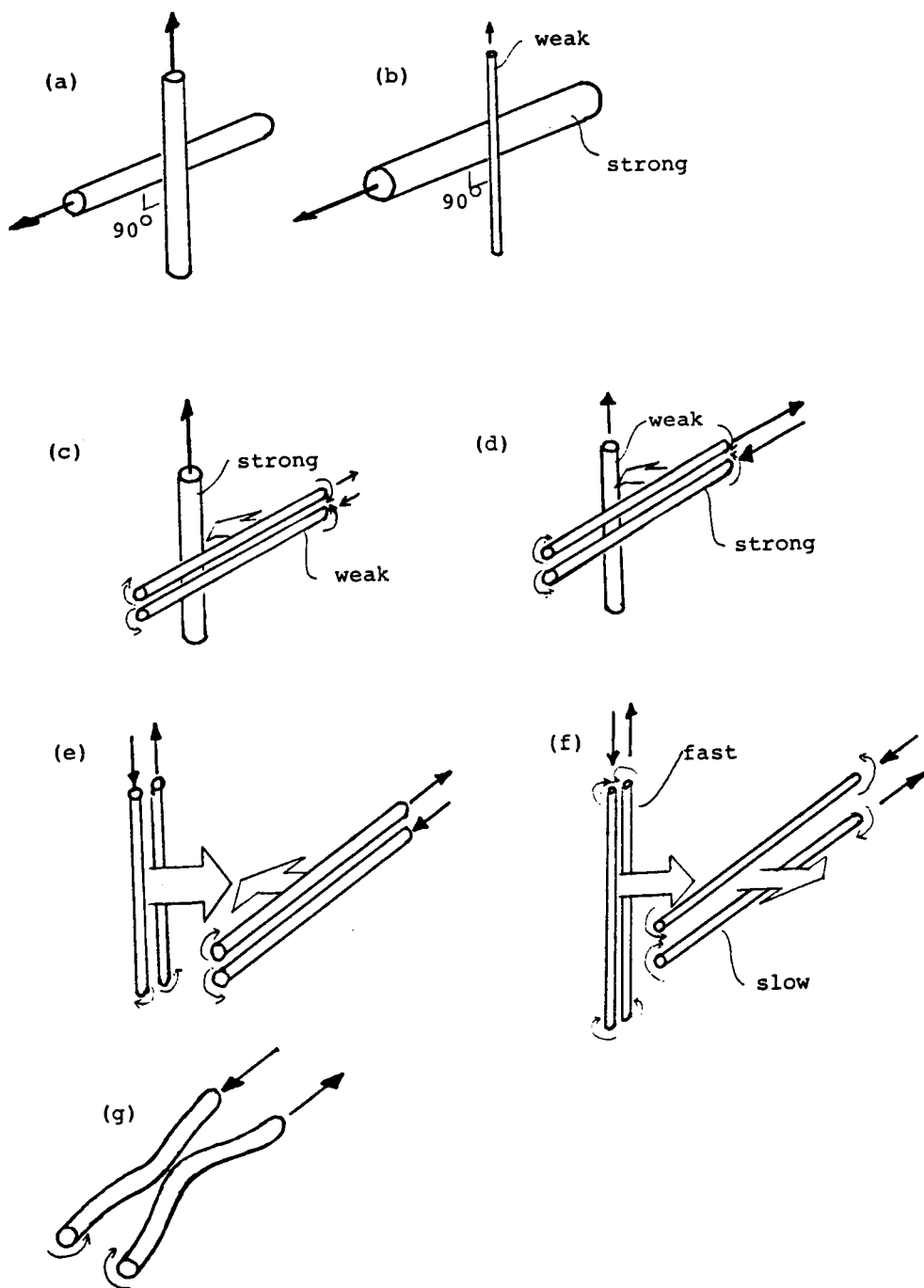


FIGURE 2. Initial conditions for the simulations.

shown in Figure 2a was simulated using both Newtonian viscosity ($Re = 2000$) and superviscosity, while in the cases (b-f) only superviscosity was used. The spatial resolution in all these cases was 96 meshpoints in each direction. The simulation starting from the initial condition shown in Figure 2g is discussed at great length elsewhere (Melander and Hussain 1988 a,b,c).

The simulations produced databases which were analyzed on graphics workstations using the "interactive" program TURB3D. Displays of the spatial vorticity distribution at various stages of the evolution were crucial in obtaining a physical understanding of the interactions. Cross sections of vorticity and velocity fields were also very helpful, whereas displays of other quantities such as helicity, dissipation, and enstrophy production were found to be of secondary importance. Tracing of vortex-lines turned out to be a major disappointment, for it seemed impossible to find just the right set of vortex lines to clearly illustrate a given interaction. In general, a few vortex-lines were not enough to reveal the dynamics, while a larger number such as 20 gave a picture that was too complicated to follow. Perhaps displays of vortex tubes via Clebsch potentials would be more appropriate.

3. Discussion

In order to achieve a higher effective Reynolds number, a superviscosity was used in most simulations. The superviscosity leaves the largest scales more inviscid than does a corresponding Newtonian viscosity. However, it is also known that the superviscosity generates artificial small scale structures. Comparison of two simulations, starting from the same initial condition (Figure 2a) but with different diffusion operators, showed similar evolutions. The most important difference between these two simulations was the evolution time-scale; it was shorter in the superviscosity simulation. A similar effect has also been observed by decreasing the Newtonian viscosity, and hence increasing Reynolds number. We therefore conclude that the use of a superviscosity mimics a higher Reynolds number flow and that the artificial small scale structures do not significantly influence the large scale structures.

Inviscid filament calculations with regularized circular cores show that two orthogonally offset vortices become locally antiparallel (Schwarz 1983 and 1985, Siggia 1985). Careful studies show that if the same filament calculations are continued further in time, then a finite-time singularity develops (Pumir and Siggia 1987). This singularity is most likely caused by insufficient degrees of freedom in the vortex cores, that is, inadequate modelling. Nevertheless, some researchers feel that a similar singularity might be present in the full Euler equations (Pumir and Kerr 1987, Kerr and Hussain 1988). It has also been suggested that this singularity is present in the Navier-Stokes equations at sufficiently high Reynolds number (Pumir and Siggia 1987). Direct numerical simulations have failed to capture signs of this singularity.

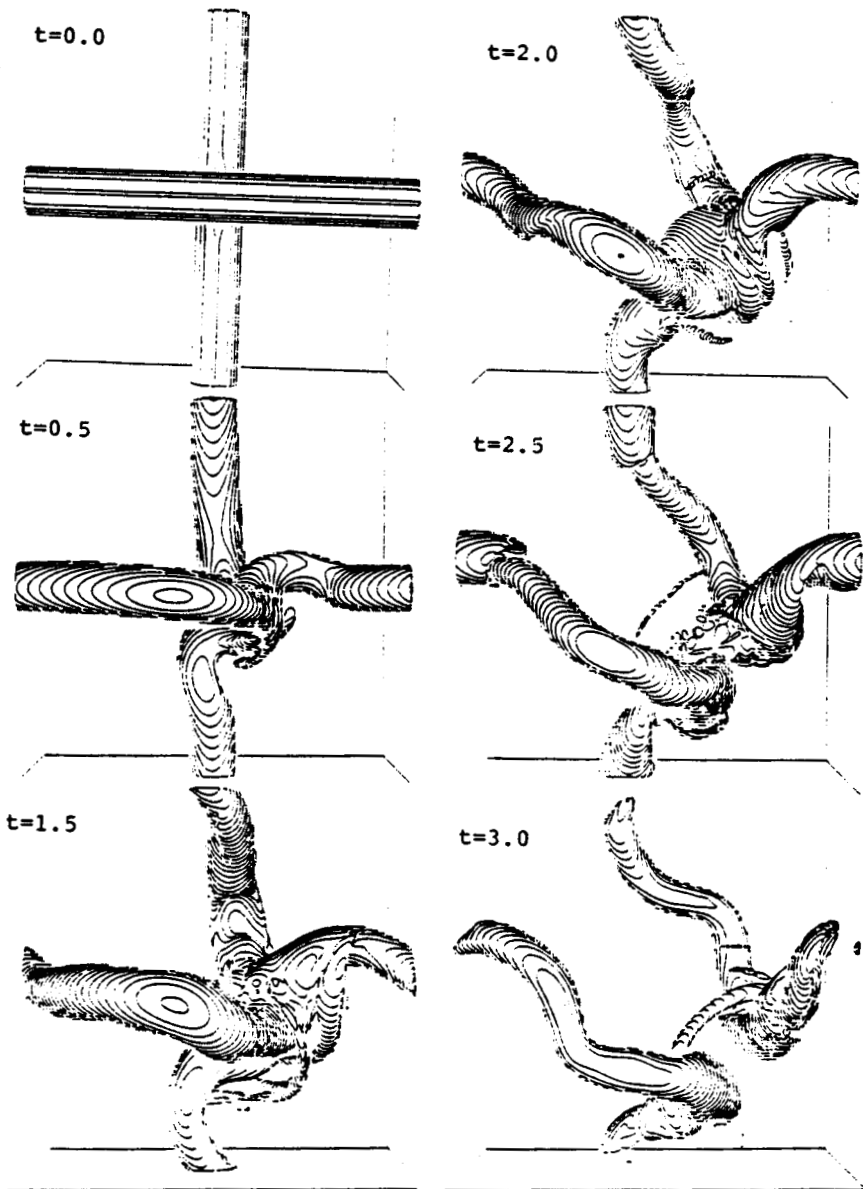


FIGURE 3. Evolution of the initial condition shown in Figure 2a at Reynolds number 2000. The panels show isovorticity surfaces at 56% of the initial peak value. Time is measured in units of $\omega_{\max}(0)/20$.

Since it is almost impossible to prove or disprove the presence of a singularity numerically, a more fruitful avenue is to concentrate on understanding the operating physical mechanisms. One can argue that if it is possible to explain the evolution without including new terms in the governing equations, then there probably is no singularity. This argument rests on the general experience that a singularity is a sign of missing physics in the governing equations.

The evolution starting from the initial condition shown in Figure 2a highlights the soft and pliable nature of vortex cores, thereby clearly showing that vortex cores do not remain nearly circular. The close proximity of the vortices results in pulling of hairpins from the outer layer of the vortex tubes (Figure 3). These hairpins form even before the main vortex tubes become locally antiparallel. Later more hairpins form, especially in the wake of the locally antiparallel vortex pair (hereafter referred to as the dipole).

The dipole is initially squashed by self-induction (due to the curvature of the antiparallel vortex pair) and thereby form a head-tail structure. The dipole is propagating by mutual induction. However, an oppositely directed velocity field is generated by the remaining part of the vortex tubes. At first the dipole velocity is the largest, but later the dipole-strength diminishes and as a result the dipole is washed backwards. Thereby the curvature of the locally antiparallel vortices reverses, the self-induced motion, therefore, also reverses, and the dipole separates slowly. This reversal is the crucial part of the reconnection process and occurs at the same time as the new "reconnected" vortices begin to separate (Figure 3).

The reversal is caused by the diminishing dipole-strength, which can happen by both a diffusive and an inviscid mechanism. The diffusive mechanism is annihilation of antiparallel vorticity by cross-diffusion in the contact-zone and is clearly important for low to medium Reynolds numbers. The result is a true reconnection, albeit this reconnection is only partial as the cross-diffusion is arrested by the reversal of the dipole propagation direction (Melander and Hussain 1988a). The inviscid mechanism is the head-tail formation. The dipole propagation velocity is determined almost exclusively by the head; therefore, the head-tail formation effectively diminishes the circulation in the dipole. In the high Reynolds number limit, this may result in an apparent reconnection. That is, the large scale vortical structures appear as though a topological reconnection has occurred, where in fact only a topology preserving entanglement has taken place. The reasons for this conjecture are as follows.

Several numerical simulations with different Reynolds numbers and different diffusion operators show that the large scale vortical structures rearrange on a time-scale T , which does not increase with Reynolds number. Weakening of the dipole is responsible for this rearrangement. If viscous effects are solely responsible for this weakening, then $|\nu\Delta\omega|$ must be at least finite as the Reynolds number tends to infinity. This in turn implies that $|\Delta\omega|$ must become unbounded within the finite time T , which can only happen through axial stretching of the

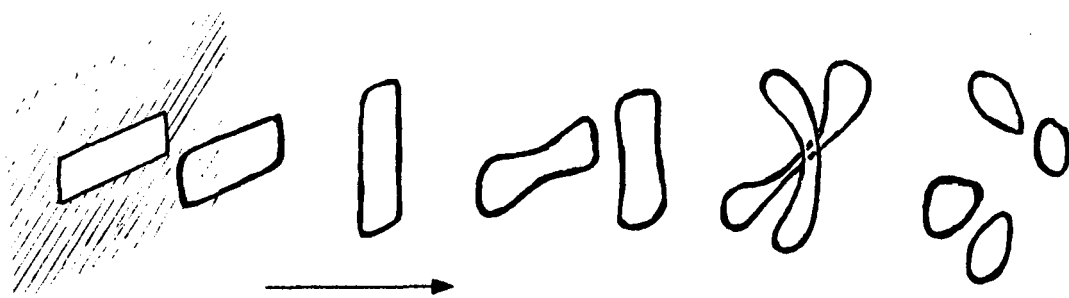


FIGURE 5. Sketch of Husain and Hussain's rectangular jet experiment.

dipole. This stretching is caused by lengthening of the antiparallel vortices in the contact-zone and by the strain form outside the contact-zone. From axisymmetric vortex dynamics (Stanaway et al 1988), we know that the lengthening effect is insufficient to cause a finite time blow up of $|\Delta\omega|$. The external strain is also bounded due to the finite length of the contact-zone.

Neither of the simulations starting from the initial condition shown in Figure 2a had sufficient resolution to clearly separate the inviscid and viscous mechanisms. It does not seem likely that sufficient resolution can be obtained in the near future. In this respect the asymmetric initial condition (Figure 2b) is more promising due to the fact that the circulation ratio can be made small such as to allow for combined simulation and analysis. The dynamics of this simulation is also much easier to grasp, see Figure 4. The weak vortex wraps around the stronger one and thereby forms a large hairpin. Vortex stretching occurs mainly in the legs of the hairpin. The tip of the hairpin is unstretched and dispersed in the azimuthal direction. Therefore, the curvature of the legs accounts for most of the self-induced motion, which is such as to split the hairpin into two diverging helical structures.

The evolutions of the initial conditions shown in Figures 2c-f were also investigated and explained. I later became aware that the latter occurs in a rectangular jet experiment by F. Hussain, see Figure 5. Pulsing of the jet generates rectangular vortex rings, which initially undergo a near-recurrence with 90° axis-flip. This phenomenon can be explained by a filament model (Bridges and Hussain 1988), except for rapid mixing processes near the corners. Further downstream an overtaking collision occurs and the resulting reconnections produce four rings. The overtaking collision occurs because the rectangular vortex

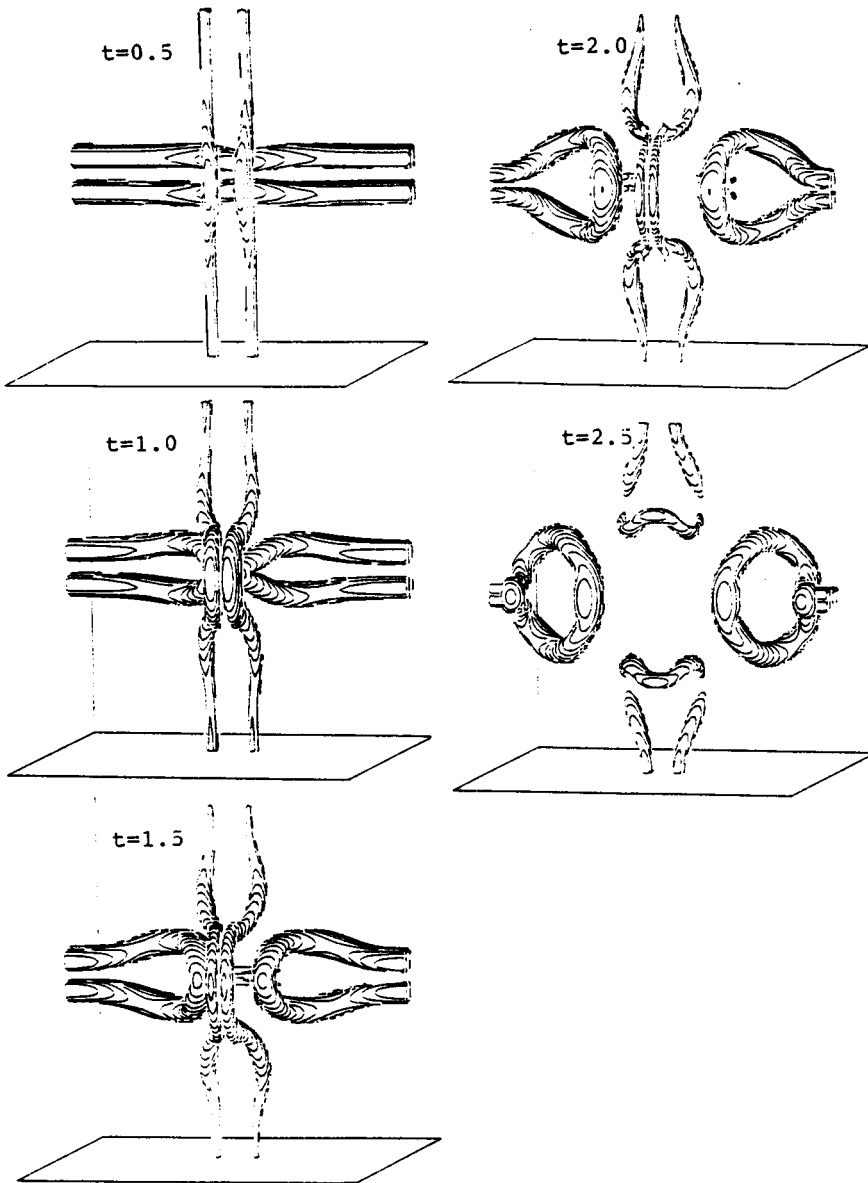


FIGURE 6. Simulation of an overtaking collision; the fast vortex pair has twice as much circulation as the slow pair. The isosurface level and timescaling are the same as in Figure 3.

rings do not comply with the traditional leap-frog process of axisymmetric vortex rings. The experiment compares well with the simulation shown in Figure 6 and clearly validates our selection of idealized initial conditions.

4. Conclusion

The insight gained by viewing the evolutions of the above idealized initial conditions on graphics workstations has proved to be invaluable in the process of constructing mathematical models of the evolutions. The modelling, which is now under way, centers around two types of initial conditions. One type is the symmetric configuration of two antiparallel vortices with sinusoidal perturbations (Figure 2g). The analysis of this model also applies to the collisions shown in Figure 2e-f. The asymmetric entanglement shown in Figure 2b and Figure 4 is also being modelled for small values of the circulation ratio.

Acknowledgement

The simulations were done at Pittsburgh Supercomputing Center and were diagnosed on workstations at NASA-Ames. I gratefully acknowledge Dr. K. Shariff for help with the workstations and many helpful discussions. Furthermore, I acknowledge Prof. F. Hussain for pointing out the connection with coherent structures.

REFERENCES

- BABIANO, A., BASDEVANT, G., LEGRAS, & B., SADOURNY, R. 1987 *J. Fluid Mech.* **183**, 379-398.
- BRIDGES, J. & HUSSAIN, F. 1988 *Bull. Amer. Phys. Soc.* **33**, 2306.
- HUSSAIN, FAZLE, A. K. M. 1986 *J. Fluid Mech.* **173**, 303-356
- KERR, R. M. & HUSSAIN, F. 1988 *Physica D.* (Subjudice).
- LEONARD, A. 1985 *Ann. Rev. Fluid Mech.* **17**, 523-59.
- MCWILLIAMS, J. C. 1984 *J. Fluid Mech.* **146**, 21-43.
- MELANDER, M. V., ZABUSKY, N. J., & STYCZEK, A. S. 1986 *J. Fluid Mech.* **167**, 95-115.
- MELANDER, M. V., & HUSSAIN, F. 1988 Center for Turbulence Research. Proceedings of the summer program 1988. (to appear)
- MELANDER, M. V., & HUSSAIN, F. 1988 *Phys. Rev. Lett.* (Subjudice).
- MELANDER, M. V., & HUSSAIN, F. 1988 *Phys. of Fluids* (Subjudice).
- MOORE, D. W., & SAFFMAN, P. G. 1972 *Philos. Trans. R. Soc. London Ser. A* **272**, 403-429.
- PUMIR, A. & KERR, R. 1987 *Phys. Rev. Lett.* **58**, 1636.
- SCHWARZ, K. W. 1983 *Phys. Rev. Lett.* **50**, 364.

SCHWARZ, K. W. 1985 *Phys. Rev. B* **31**, 5782.

SIGGIA, E. D. 1985 *Phys. of Fluids* **28**, 794.

STANAWAY, S., SHARIFF K., & HUSSAIN, F. 1988 CTR Proceedings of the 1988 Summer Program, 287-309.

Numerical simulation of viscous vortex rings

By S. K. STANAWAY

1. Motivation & Objectives

This work is directed toward understanding vortex interactions and their role in turbulent flow. The objectives are twofold. First, to use the existing axisymmetric code to study the annihilation process of colliding vortex rings and determine the relevance of this problem to similar 3D phenomena. The second objective is to extend the code to three dimensions. The code under development is unique in that it can compute flows in a truly infinite domain (i.e. without periodic boundary conditions or approximations from truncating the domain). Because of this, we are able to compute the far field sound, and therefore, contribute to improved models of turbulence generated noise for this class of flows. Issues which can be addressed by the code include: effects of viscosity on mode selection in azimuthal breakdown of vortex rings (i.e. the Widnall instability); reconnection, the associated production of small scales, and the time scale of the process.

2. Accomplishments

Objective 1: Study head-on collision of viscous vortex rings

During the CTR Summer Program, a collaboration was undertaken between the author, K. Shariff and F. Hussain to study the head-on collision of two identical axisymmetric viscous vortex rings through direct simulations of the incompressible Navier-Stokes equations. The result of this effort is described in the proceedings for the 1988 Summer Program of the CTR (Stanaway *et al.* 1988).

Initial conditions of varying core shapes (thin rings, and Hill's spherical vortex rings) and Reynolds numbers (350 to 1000) were considered and the subsequent annihilation process was studied through time history of circulation, vorticity contours and local contributions to annihilation. The results provide a database to model such a problem and also information about the level of detail required to accurately model this phenomenon. A typical interaction proceeds as follows. Two vortices of opposite sense and the same strength approach each other by self-induction, the radii increase by mutual induction, and vorticity cancels through viscous diffusion across the collision plane. Following contact, we observed (for the cases considered here) that the vorticity distribution in the core forms a head-tail structure, a behavior which has also been seen in inviscid calculations (Shariff *et al.* 1988), 3D viscous calculations with periodic boundary conditions

(Melander & Hussain 1988, MH), and experiments (Oshima 1978). In examining the local contributions to the total vorticity annihilation in both the head and tail regions, we conclude that the tail does contain a significant part of the vorticity and should be included in an accurate model of the annihilation process.

The characteristic time of vorticity annihilation is compared with that of a 3D collision experiment (Schatzle 1987) and 3D numerical simulations (MH). It is found that the annihilation timescale for the axisymmetric collision is faster than the viscous timescale, a_o^2/ν , and slower than the timescale set by the circulation, $a_o^2/(\Gamma_o\nu)^{1/2}$, where a_o is the initial core radius, Γ_o is the initial circulation, and ν is the viscosity. This indicates that the local effects are important in enhancing annihilation, however, nonlocal effects such as vorticity realignment are also important in 3D. One might expect that during the initial stages of the collision, local effects are dominant, and as the circulation in the symmetry plane weakens, the bridges strengthen and the out-of-plane strain becomes the more important effect.

The flow is also computed to the large time Stokes flow limit where the circulation decays as $t^{-3/2}$ and the vorticity distribution agrees with the quadrupole solution of the Stokes equations. In this limit, the self-annihilation is exactly twice the mutual annihilation. For one of the cases computed, the far-field quadrupole sound is compared with the experimental results of Kambe & Minota (1983). The agreement is quite good even though the Reynolds numbers are very different.

Objective 2: Extend axisymmetric spectral code to three dimensions

An operational axisymmetric code which solves the Navier-Stokes equations in an unbounded domain is being modified to compute 3D flows. The method (Stanaway, Cantwell & Spalart 1988) uses divergence free basis functions, having the advantages of reducing the number of unknowns from four to two, and eliminating the need to solve a Poisson equation for the pressure at each time step. The solution is expanded in polar coordinates with the associated Legendre functions in the polar direction and Jacobi polynomials matched to an algebraic mapping of the radial coordinate. The third dimension, the azimuthal direction, is expanded in Fourier series. The above functions are used in order that the resulting matrix equations are numerically attractive; they are completely orthogonal in two directions and have a constant and relatively narrow bandwidth in the third direction (bandwidth ≤ 11). In addition, in the present method the matrices are symmetric and positive definite.

The unknown coefficients in wave space, referred to as the $+$ and $-$ modes (in keeping with the notation of similar approaches), each have an ordinary differential equation describing their evolution. The axisymmetric basis functions are a subset of the three dimensional functions, meaning that in extending the axisymmetric code to 3D, much of the code remains intact. Specifically, the evolution equation for the $+$ modes is unchanged. In the 3D case, an additional

evolution equation is required for the $-$ modes. In the development of the axisymmetric code, it was necessary to compute the matrix elements analytically rather than numerically in order to minimize errors leading to ill conditioned matrices. This process, which was rather involved due to the complex coordinate system and mapping, was made possible with the aid of MACSYMA, an algebraic manipulation program. It is worth noting that the effort required to compute the elements of the matrices for the $-$ modes was considerably less than it was for the $+$ modes. The major effort, therefore, in extending the code to three dimensions has been in developing the transforms to and from wave space for the 3D basis functions. This step is nearly finished and will be tested in a straightforward manner by starting with an initial vorticity field, transforming to wave space, and then back to real space.

So the problem of extending the code involves four phases:

- (i) Deriving the basis functions and evolution equations.
- (ii) Forming the matrices for the $-$ mode evolution equation.
- (iii) Developing and testing three dimensional transforms going to and from wave space.
- (iv) Running test cases.

Considerable progress has been made in extending the code to three dimensions and it is expected that the 3D code will soon be operational.

3. Future Plans

This new method gives us the unique capability to study many important and often controversial phenomena accurately, notably

- the Widnall instability of an almost axisymmetric ring, in particular, the mode selection process;
- viscous connection and splitting;
- redistribution of vorticity by colliding or pairing vortex rings; and
- generation, intensification and annihilation of vorticity through vortex ring interactions.

REFERENCES

- KAMBE, T. & MINOTA, T. 1983 acoustic wave radiated by head-on collision of two vortex rings. *Proc. R. Soc. Lond. A.* **386**, 277–308.
- MELANDER, M. & HUSSAIN, F. 1988 Cut-and-connect of two antiparallel vortex tubes. *CTR Proc. of the 1988 Summer Program* NASA Ames Research Center/Stanford University.
- OSHIMA, Y. 1978 Head-on collision of two vortex rings. *J. Phys. Soc. Jap.* **44**, 328–331.
- SCHATZLE, P. R. 1987 An experimental study of fusion of vortex rings. Ph.D. Thesis. Graduate Aeronautical Laboratories, Caltech.

- SHARIFF, K., LEONARD, A., ZABUSKY, N., & FERZIGER, J. 1988 Acoustics and dynamics of coaxial interacting vortex rings. *Fluid Dynamics Research*. **3**.
- STANAWAY, S. K., CANTWELL, B. J. & SPALART, P. R. 1988 A numerical study of viscous vortex rings using a spectral method. NASA TM 101004.
- STANAWAY, S. K., SHARIFF, K. & HUSSAIN, F. 1988 Head-on collision of viscous vortex rings. *CTR Proc. of the 1988 Summer Program* NASA Ames Research Center-Stanford University.

The effects of particle loading on turbulence structure and modelling

By K. D. SQUIRES AND J. K. EATON

1. Introduction

Conventional wisdom implies that the presence of particles provides an additional dissipation or attenuation of turbulence. However, it is not clear how this extra dissipation may be incorporated into turbulence models or how it depends on the parameters of the problem including the particle time constant, the mass loading, and the various dimensionless parameters describing the turbulence. Simply focusing on the extra dissipation completely neglects the effect of turbulence structure on the instantaneous particle concentration field and the possibility of interactions between the particle cloud and instability mechanisms generating turbulence. For example, particles selectively concentrated in particular structures may cause rapid attenuation of that structure or trigger a new instability mechanism. Therefore, it is important to determine the effect of turbulence structure on the behavior of the particle cloud.

The objective of the present research was to extend the DNS approach to particle-laden turbulent flows using a simple model of particle/flow interaction. The program addressed the simplest type of flow, homogeneous, isotropic turbulence, and examined interactions between the particles and gas phase turbulence. The specific range of problems examined include those in which the particle is much smaller than the smallest length scales of the turbulence yet heavy enough to slip relative to the flow. The particle mass loading is large enough to have a significant impact on the turbulence, while the volume loading was small enough such that particle-particle interactions could be neglected. Therefore, these simulations are relevant to practical problems involving small, dense particles conveyed by turbulent gas flows at moderate loadings.

This report presents a sample of the results illustrating modifications of the particle concentration field caused by the turbulence structure and also illustrating attenuation of turbulence by the particle cloud.

2. Overview of the simulations

The numerical method used in the present research is based on the pseudo-spectral technique developed by Rogallo (1981) for solving the incompressible Navier-Stokes equations. A modification of Rogallo's code was used to simultaneously track a large number of particles using a vectorized, second-order interpolation scheme. This code is time advanced using second-order Runge-Kutta, and at each substep the fluid velocity at the particle position was calculated

using trilinear interpolation. Numerical experiments showed that more accurate interpolation schemes do not significantly improve the results. The new position was obtained by then integrating the particle equation of motion

$$\frac{dv_i(t)}{dt} = \frac{u_i(X_j(t), t) - v_i(t)}{\tau_p} \quad (2.1)$$

$$\frac{dX_i(t)}{dt} = v_i(t) \quad (2.2)$$

where $X_j(t)$ and $v_i(t)$ are the position and velocity of the particle, τ_p is the particle time constant, and $u_i(X_j(t), t)$ is the velocity of the fluid. Stokes' law has been used to calculate the drag on a particle, and it is, therefore, assumed that the particle is much smaller than any lengthscale of the flow (the Kolmogorov scale, η). It is also assumed that the particles are sufficiently dense such that other forces in the full equation of motion, e.g. buoyancy and added mass, are negligible compared to the Stokes drag. Finally, the particles are assumed to occupy a negligible volume fraction, and particle-particle interactions are also assumed negligible.

To calculate the effect of the particles on the turbulence, the momentum equation of the fluid was modified by a source term on the right-hand side

$$\frac{\partial u_i}{\partial t} + u_j \frac{\partial u_i}{\partial t} = -\frac{1}{\rho} \frac{\partial P}{\partial x_i} + \nu \frac{\partial^2 u_i}{\partial x_j \partial x_j} - \frac{c}{\tau_p \rho} (u_i - v_i) \quad (2.3)$$

where $c(x_i, t)$ is the particle mass per unit of volume, or particle density (repeated indices imply summation).

The problem studied is homogeneous, isotropic turbulence in a box. "Natural" isotropic turbulence decays, and the lack of stationarity complicates analysis of the results. Therefore, the low wave number modes (large scales) are artificially forced to maintain stationarity using the scheme developed by Hunt, et al (1987). Results were obtained using 373000 particles for simulations using 32^3 points and 1×10^6 particles for simulations using 64^3 points. The relatively coarse grid 32^3 calculations permitted a parameter study in particle time constant and mass loading ratio. For the 32^3 simulations the values of the particle time constant divided by the eddy turnover time used were 0.14, 0.75, and 1.50. The mass-loadings used in the 32^3 simulations were 0.1, 0.5, and 1.0. All three values of the mass loading were used for each of the time constants for these simulations. For the 64^3 simulations the values of the dimensionless time constant were 0.075, 0.15, and 0.52 and the mass loadings were 0.1, 0.5, and 1.0.

For each simulation the two phases were uncoupled and time-advanced to reach a statistically stationary state and eliminate initial transients of the forcing. At this point in time, the momentum equation of the fluid was coupled to the particle momentum equation with a specified mass loading. Once the phases

were coupled, the simulations were time advanced just over 12 eddy turnover times for the 32^3 simulations and slightly over 6 eddy turnover times for the 64^3 simulations.

Results from the simulations of no coupling ($\phi = 0$ where ϕ is the mass loading) between the phases provide a baseline case to compare the effect of increased mass loading on the turbulence statistics. These simulations are also useful for examining the effect of turbulence "structure" on the particle concentration field. For these baseline simulations the Reynolds number based on the Taylor microscale was approximately 37. This relatively low value for the Reynolds number assured good resolution of the velocity field.

3. Results and discussion

Maxey (1987) has shown that particles will tend to accumulate in regions of high strain rate or low vorticity. This effect can be measured by using the second invariant of the deformation tensor, $\partial u_i / \partial x_j$. The second invariant of $\partial u_i / \partial x_j$ is given by

$$II_d = -\frac{1}{2}(s^2 - \frac{1}{2}\omega_j\omega_j) \quad (3.1)$$

where s^2 is the magnitude of the strain rate, $s_{ij}s_{ji}$, ω_j is the j th component of the vorticity vector and $\omega_j\omega_j$ is by definition the enstrophy.

Thus, from equation (3.1) highly vortical regions correspond to II_d being large and positive (where the number density is small), while regions of high strain correspond to II_d being large and negative (where the number density is large).

Contours of number density for each of the particles used in the simulations showed distinct regions where particles had collected. It was found that the peak number density is as much as 40-50 times the mean value for the lightest particles used in the simulations. By comparing these contours with the contours of the second invariant of $\partial u_i / \partial x_j$, it was found that the particles showed a tendency to accumulate in regions of low vorticity or high strain rate. As the particles were made more sluggish (i.e., larger τ_p), there is less of a tendency for them to accumulate in these regions. For the heaviest particle used in the 32^3 simulations ($\tau_p/T_e = 1.50$), the particle concentration field was found to be essentially random.

The preceding results were quantified by examining the conditional expectation of the number density given the value of the enstrophy. The conditional expectation showed that the effect of increasing particle inertia reduced the likelihood of finding the particles in regions of low vorticity (figure 1). For the 64^3 simulations, the lightest particles ($\tau_p/T_e = 0.075$) actually showed *less* of a tendency to accumulate in regions of low vorticity than did particles which were twice as heavy ($\tau_p/T_e = 0.150$). This can be explained by the fact that very light particles can follow nearly all of the turbulent motions and would, therefore, show no preference to be in regions of low vorticity.

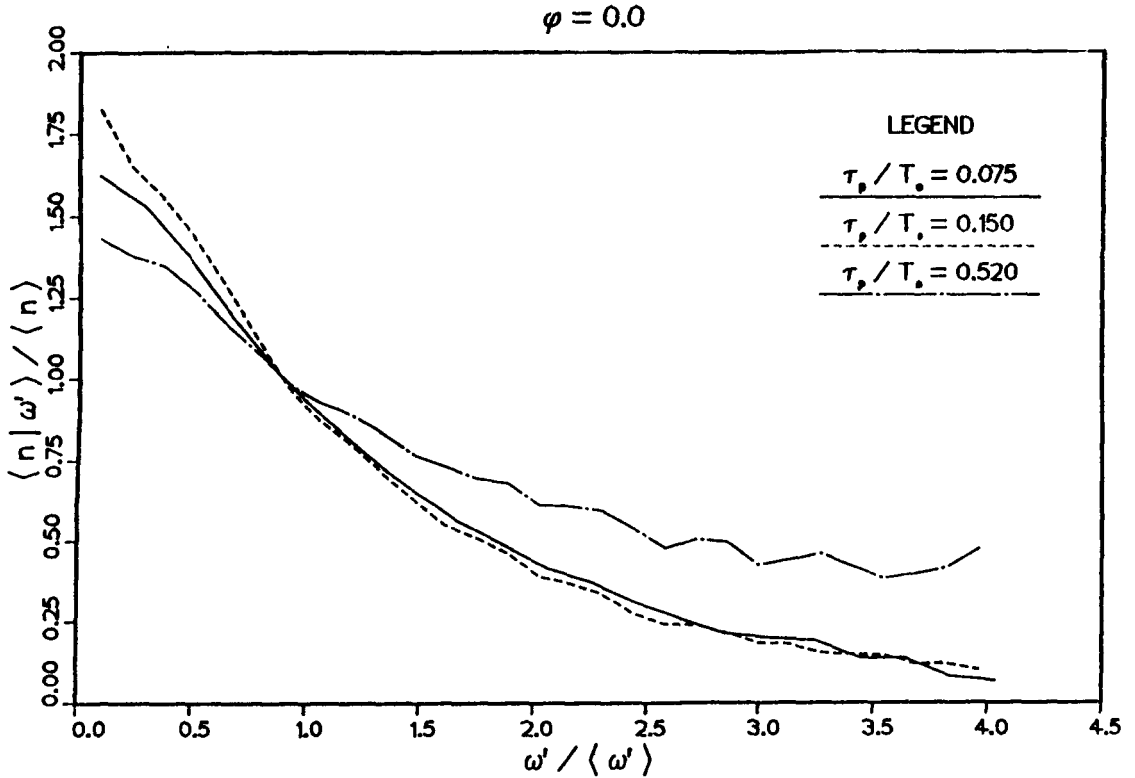


FIGURE 1. Conditional expectation of number density given enstrophy for the 64^3 simulations, $\phi = 0$.

For increasing values of the mass loading, the conditional expectation of number density given the enstrophy for the light particles showed that they had less of a tendency to be in regions of low vorticity. However, this was not the case for the heavier particles.

Correlations between the number density and enstrophy showed that as the loading was increased the lightest particles became less correlated with enstrophy. For the larger time constants, however, the number density and enstrophy become more correlated for increasing values of the time constant and increased loading. Correlations between number density and II_d showed that as the mass loading was increased the correlation between number density and II_d increased. This increase in the correlation was more significant for larger values of the time constant.

Once the two phases were coupled, the turbulence evolved to a new stationary state within about two eddy turnover times. For all the time constants used in the simulation, it was found that the time required to come to a new equilibrium was longer for increasing loadings, and the maximum development time for any case was just over two eddy turnover times. Time averaged statistics such as turbulence energy showed that increased mass loading decreased the turbulence

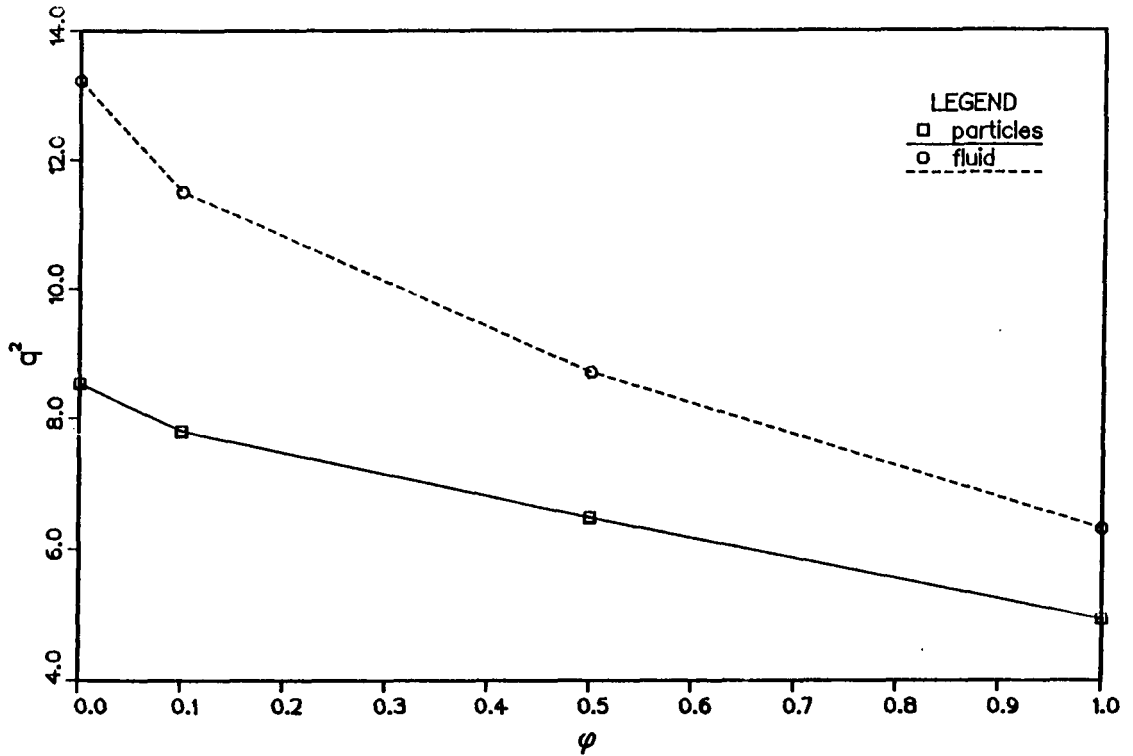


FIGURE 2. Turbulence energy versus loading from the 32^s simulations, $\tau_p/T_e = 0.75$.

energy (figure 2). These results are consistent with the fact that the drag of the particles on the turbulence acts as an additional source of dissipation. This can be shown by deriving the transport equations for $u_i u_i$ (beginning with equation (2.3)).

Frequency spectra measured *along the particle path* were nearly identical for all simulations. The differences in the turbulence spectrum for the three cases can be attributed to the fact that the lighter particles are found more often in regions of low vorticity and high strain rate than are the heavier particles. This causes a sampling bias resulting in the differences between the spectra along the particle path. Measured values of the particle velocity spectra were found to be in excellent agreement with a theoretical prediction of Csanady (1963). It was somewhat surprising to find such close agreement with Csanady's theory in view of the fact that the particles are concentrated within particular regions of the turbulence. Examination of the power spectra of the turbulence for increasing values of the mass loading showed that energy was removed nearly equally from all frequencies. This may be due in part to the low Reynolds number of the simulations. Selective energy loss within certain frequency bands may occur at higher Reynolds numbers.

Correlations between enstrophy and pressure were decreased more by the light particles than by the heavy particles for increasing values of the mass loading. Since regions of low pressure are associated with regions of high vorticity, these results indicate that the lighter particles cause more distortion of these eddies than do the heavier particles. The fact that the lighter particles show a more pronounced tendency to accumulate in regions of lower vorticity (for $\phi = 0$) than do the heavier particles may provide some explanation for this.

Correlations between II_d and pressure showed that for the time constants and mass loadings used in the simulations the correlation between these two quantities remained reasonably constant, decreasing slightly for the lightest particles. Correlating II_d with pressure correlates regions of low pressure with vortices (large positive II_d) and regions of high pressure with straining regions (large negative II_d). Therefore, these results indicate that the correlation between the straining regions with regions of high pressure must be increasing to compensate for the loss of correlation between the vortical regions and regions of low pressure for the lighter particles.

In summary, it was found that for the case of zero loading there are significant effects of the turbulence "structure" on the resulting concentration field. These results were quantified by measuring conditional expectations and correlations. It is shown that the lighter particles show a strong tendency to be in regions of low vorticity and high strain rate.

For increasing values of the mass loading the power spectra of the turbulent fluctuations do not show any frequencies to be preferentially modified by the particles. This may be partially due to the fact that there is not a large range of scales in the simulations.

The lightest particles used in these simulations were found to modify the turbulence field differently than did the heavier particles. Since the light particles show a more pronounced tendency to accumulate in regions of low vorticity for $\phi = 0$, these regions are modified more by the light particles as the loading is increased than the heavy particles. Evidently, this selective modification by the light particles causes more of a distortion of the turbulent eddies than the more uniform modification by the heavier particles.

REFERENCES

- CSANADY, G. T. 1963 Turbulent Diffusion of Heavy Particles in the Atmosphere. *Journal of the Atmospheric Sciences*. 20, 201-208.
- HUNT, J. C., BUELL, J. C., & WRAY, A. A. 1987 Big Whorls Carry Little Whorls. *Report CTR-S87* Proceedings of the 1987 Summer Program, NASA Ames-Stanford Center for Turbulence Research, Stanford, California.

- MAXEY, M. R. 1987 The Gravitational Settling of Aerosol Particles in Homogeneous Turbulence and Random Flow Fields. *Journal of Fluid Mechanics*. **174**, 441-465.
- ROGALLO, R. S. 1981 Numerical Experiments in Homogeneous Turbulence. *NASA Tech. Memo.* **81315**.

Analyses of turbulence structures in shear flows

By M. J. LEE

Outline of the research program and a recent progress in the studies of sheared turbulence are described. The research program reported here is directed at two goals: (i) understanding of fundamental physics of organized structures in turbulent shear flows; and (ii) development of phenomenological models of turbulence based on physical arguments. Three projects that have been carried out are:

- A. structure of sheared turbulence near a plane boundary;
- B. distortion of turbulence by axisymmetric strain and dilatation;
- C. study of energy transfer in turbulent shear flow.

1. Motivation and Objectives

Project A was motivated by the demonstration of remarkable similarity between homogeneous turbulent shear flow and turbulent channel flow in instantaneous velocity (and vorticity) fields and statistical correlations at the same dimensionless shear rate $S^* = Sq^2/\epsilon$ (Lee, Kim & Moin 1987). Here, $S = dU/dy$ is the mean 'shear rate,' $q^2 = \overline{u_i u_i}$ is twice the turbulent kinetic energy and ϵ is the dissipation rate of the kinetic energy. The similarity in instantaneous vector flow topology as well as in statistical measures bears a profound implication towards a possibility of developing a 'universal' turbulence model. In particular, this study showed that shear rate alone (without a wall) can produce the streaky structures, providing a strong support for the importance of shear rate in determining turbulence structures.

The presence of a solid boundary affects turbulence in two fundamental ways:

- (i) generation of mean velocity gradient (via the no-slip condition) which, upon interaction with turbulence, supplies energy to it; and
- (ii) suppression of velocity fluctuations in its vicinity.

It is hypothesized that these two effects are distinct in affecting turbulence structure so that they can be accounted for separately. Project A centers on the analysis of these two functions of a solid boundary and consists of three subprojects: uniform-shear boundary layer (USBL), plane Couette flow (PCF) and shear-free channel flow (SFCF). See figure 1 for schematic of the flows.

The uniform-shear boundary layer (USBL) project aims at a theoretical explanation of the generation mechanism of the streaks in turbulent shear flows (Lee & Hunt 1988). In USBL, the mean flow has a velocity profile $U = Sy + U_0$ with the shear rate S uniform and constant, and the flow field is assumed to be inviscid with a slip velocity condition at the surface $y = 0$. The analysis was

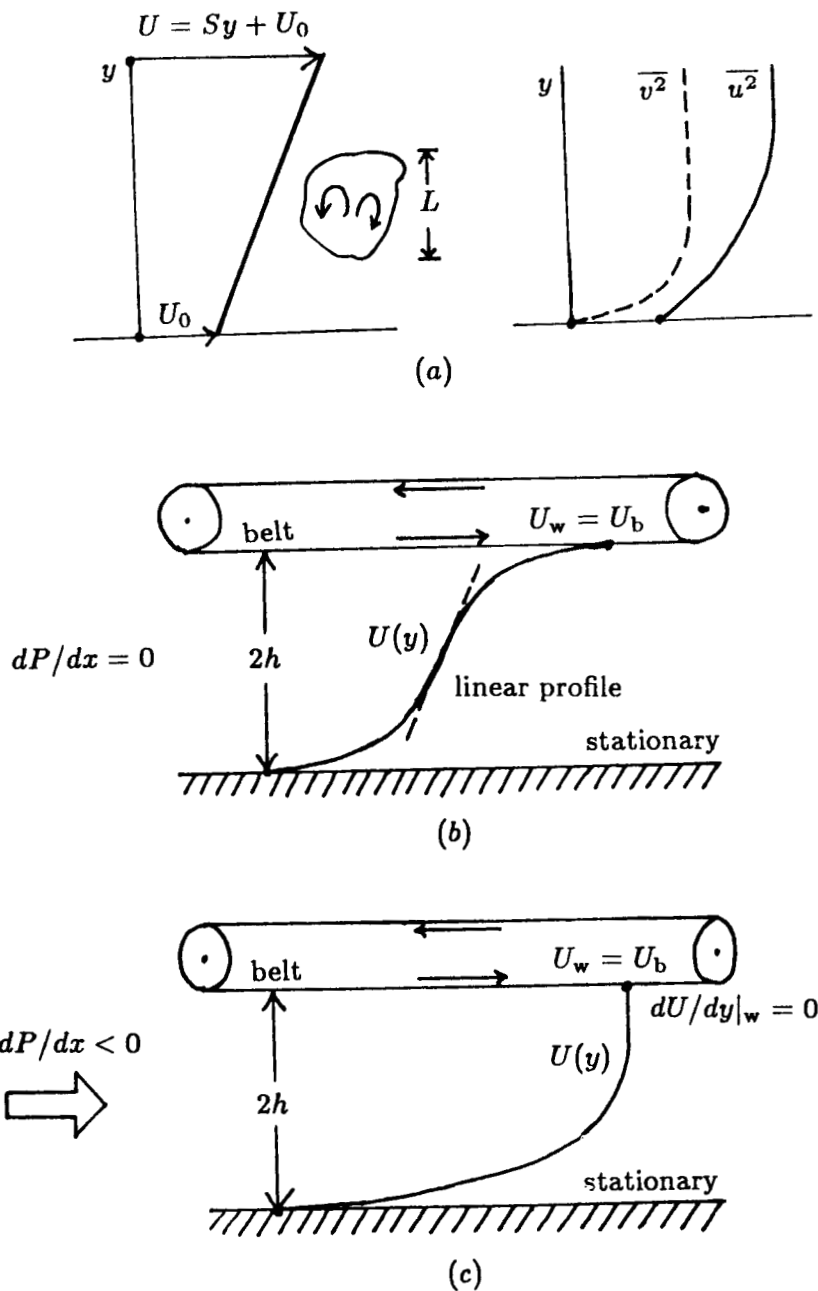


FIGURE 1. Schematic diagram of turbulent shear flows: (a) a uniform-shear boundary layer (USBL); (b) plane Couette flow (PCF); (c) shear-free channel flow (SFCF).

carried out for the evolution and distribution of turbulence by using rapid distortion theory (RDT). Particular emphasis is placed on the differences between the shear-free boundary layer (see Uzkan & Reynolds 1967; Hunt & Graham 1978; Hunt 1984) in redistributing turbulence near the surface by the blocking effect.

The plane Couette flow (PCF) and shear-free channel flow (SFCF) projects were motivated by a need to generate numerical databases of turbulent wall-bounded flows with a constant total shear stress $\tau(y) = \mu dU/dy - \rho \overline{uv} = \tau_w$ across the boundary layer (PCF) and zero mean velocity gradient near a wall (SFCF), respectively. These two cases are considered as building-block flows since most turbulence models are based on the wall-layer similarity with a constant shear stress τ (Townsend 1976, §§5.4, 5.7–5.9). It is of our interest to characterize organized turbulence structures in the near-wall regions at different mean shear rates and to examine the capability of the current scaling laws (or turbulence models) in describing turbulence characteristics of such flows (cf. El Telbany & Reynolds 1980, 1981).

The purpose of Project B is to investigate the behavior of homogeneous turbulence subjected to axisymmetric distortion (contraction and expansion) and dilatation (Lee 1988). Closed-form solutions obtained by using RDT are compared with the numerical simulations (Lee & Reynolds 1985). The theoretical results are then used to develop a model for the pressure-strain-rate term $T_{ij} = (2/\rho) \overline{ps_{ij}}$. A 'simple' model for the pressure-strain-rate term shows that the 'history effect' (total strain) is important.

Project C is to explore detailed processes of the pressure-strain energy transfer in a turbulent shear flow (Brasseur & Lee 1987, 1988). Relationships between a local energy transfer event and the nearby vortical structures are studied by looking into instantaneous flow fields from numerical simulations of homogeneous shear flow (Rogers *et al.* 1986). For a kinematical description of the process, the energy transfer is classified into six classes according to the instantaneous directionality of the energy transfer between components. This concept of the energy transfer class can be applied to the statistical quantities such as the average value and probability density function (pdf). In this project, we are also interested in exploring the energy transfer across the different scales (e.g. spectral energy transfer) and its relationship with the intercomponent energy transfer.

2. Accomplishments

2.1. Project A: Wall Turbulence

2.1.1. USBL Project

The USBL project (Lee & Hunt 1988) convincingly demonstrates that the streak generation is entirely due the high shear rate, and that the surface blocking, in fact, prohibits formation of the streaks. As shown by Lee, Colonius &

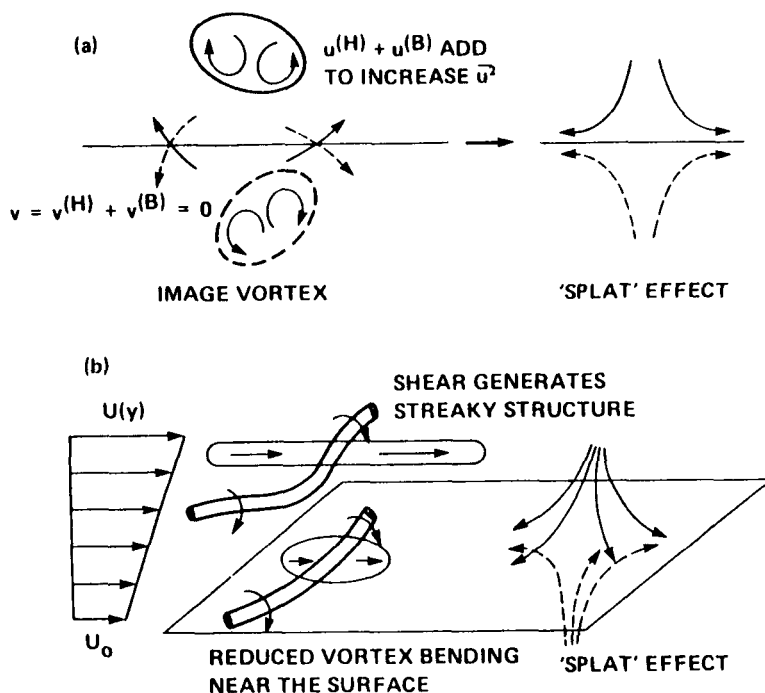


FIGURE 2. Schematic diagram to show difference between the mechanisms for (a) shear-free boundary layer, where image vortex below $y = 0$ induces irrotational velocity $u^{(B)}$ above $y = 0$; and (b) uniform-shear boundary layer, where reduced vortex bending near the surface reduces \bar{u}^2 while splat effect increases \bar{u}^2 .

Moin (1988), the streaks consist of eddies of large streamwise velocity fluctuations and turbulent shear stress $-uv$, and hence they are energy-producing eddies. The vorticity field associated with the streaks is found to be corrugated sheet vortex which has large spanwise and normal vorticity fluctuations, ω_x and ω_y , but relatively weak streamwise vorticity, ω_z . Near a solid surface, the corrugated vortex sheet becomes flat (less corrugated) due to the blocking effect of the surface, thus reducing the dominance of the streamwise fluctuations (see figure 2).

Figure 3 shows the energy spectra of the streamwise velocity $E_{11}(\kappa_3; y)$ as a function of the spanwise wavenumber κ_3 and total shear $\beta = St$ at $y/L = 0$ and 1 (L is the energy integral scale at $\beta = 0$). While there is no evident sign of the streaks at the surface $y = 0$ (fig. 3a), the spectra away from the surface ($y/L = 1$) show peaks that develop significantly with shear (fig. 3b). The fact that the streaks exist in sheared turbulence, independent of the presence of a solid boundary, but not in a shear-free boundary layer (Uzkan & Reynolds 1967), strongly supports the assertion that the main mechanism of generating

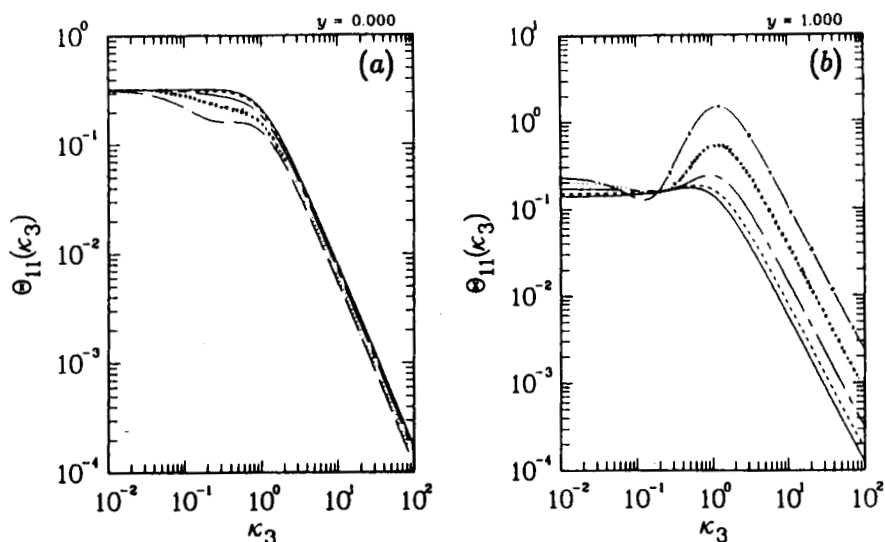


FIGURE 3. Variation with shear of the spanwise one-dimensional energy spectra $\Theta_{11}(\kappa_3)$ of the streamwise fluctuation: (a) $y = 0.0$; (b) $y = 1.0$. —, $\beta = 0$; ----, $\beta = 1$; — — —, $\beta = 2$; ·····, $\beta = 4$; — · —, $\beta = 8$.

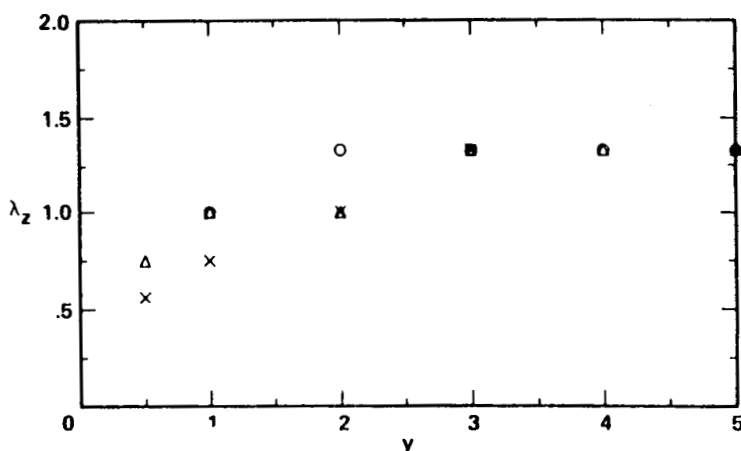


FIGURE 4. Variation with the distance from the boundary of the mean streak spacing, λ_z . The mean streak spacing is determined from the spanwise wavenumber at which $\Theta_{11}(\kappa_3; y)$ peaks. ○, $\beta = 2$; △, $\beta = 4$; ×, $\beta = 8$.

the streaks is the mean shear but not the wall blocking (Lee *et al.* 1987).

Notice that the peaks within a narrow band of κ_3 are indicative of the existence of the streaks in the flow. The mean spanwise spacing λ_z of the streaks can be estimated from the wavenumber at which the spectrum peaks: $\lambda_z = 1/\kappa_3^*$. In

figure 4, the variation of the mean streak spacing shows an increase with y . This study reinforces our earlier work (Lee, Kim & Moin 1987), namely, that the generation mechanism of the streaks is essentially *inviscid* and *linear*.

2.1.2. PCF Project

The PCF and SFCF projects make use of numerical databases from direct simulations. We have completed numerical simulation of plane Couette flow (PCF) with a wall moving at a speed U_w parallel to the stationary wall. The computation was performed on a $128 \times 129 \times 128$ grid and a passive scalar field ($Pr = 0.71$) with constant boundary conditions was included in the computation. The flow Reynolds number Re based on the wall velocity U_w and half the channel width h is 6,000, and that based on the shear velocity $U_\tau = (\nu dU/dy|_w)^{1/2}$ is about 200. Other major aspects of the computation are similar to those in the Poiseuille flow of Kim *et al.* (1987). The computation has been conducted for a period of about $100 h/U_w$ that corresponds to about ten (10) computational box lengths.

In figure 5(a), the computed mean velocity profile across the channel is compared with the experimental results conducted at different flow Reynolds numbers ($Re = 2,900$, Reichardt 1959; $Re \simeq 2 \times 10^4 - 4 \times 10^4$, El Telbany & Reynolds 1980). It should be noticed that at high Reynolds numbers the velocity profile changes rapidly within a narrow region near the walls ($|y| \geq 0.8$), and that there exists a constant slope over half the channel width around the center ($|y| \leq 0.5$). The mean velocity gradient at the boundary $dU/dy|_w$ grows significantly with the Reynolds number. The near-wall profile made dimensionless by the viscous units (U_τ and $\ell_v = \nu/U_\tau$) is in good agreement with the classical law of the wall (fig. 5b).

The turbulence intensities ($u'^{++}, v'^{++}, w'^{++}$) scaled by the shear velocity U_τ in figure 6 also show good agreement with the experimental results at higher Reynolds numbers (El Telbany & Reynolds 1981). Compared with those in a plane Poiseuille flow at comparable Reynolds numbers (Kim *et al.* 1987; Kreplin & Eckelmann 1979), the intensities in PCF are significantly higher over most of the channel, except in the vicinity of the wall ($y \leq 30$) where the PCF values are only slightly higher. This marked contrast is a direct consequence of the constancy of total shear stress $\tau/\rho = \nu dU/dy - \overline{uv}$ across the channel in PCF. (In a plane Poiseuille flow, the total shear stress has a linear profile $\tau/|\tau_w| = -y/h$, and $dU/dy = 0$ and $\overline{uv} = 0$ at the channel center, $y = 0$, by symmetry.)

The turbulence structure exhibits strong anisotropy; even in the core region, $\overline{u^2} : \overline{v^2} : \overline{w^2} \simeq 6 : 1 : 2$. The linear mean velocity profile (i.e. constant mean shear rate) in the core region is indicative of the existence of homogeneous turbulence, where the turbulence statistics are approximately constant (see figure 6).

2.1.3. SFCF Project

In order to achieve zero mean shear rate in the wall region of shear-free channel flow (SFCF), one needs to determine the speed of the moving wall U_w and the

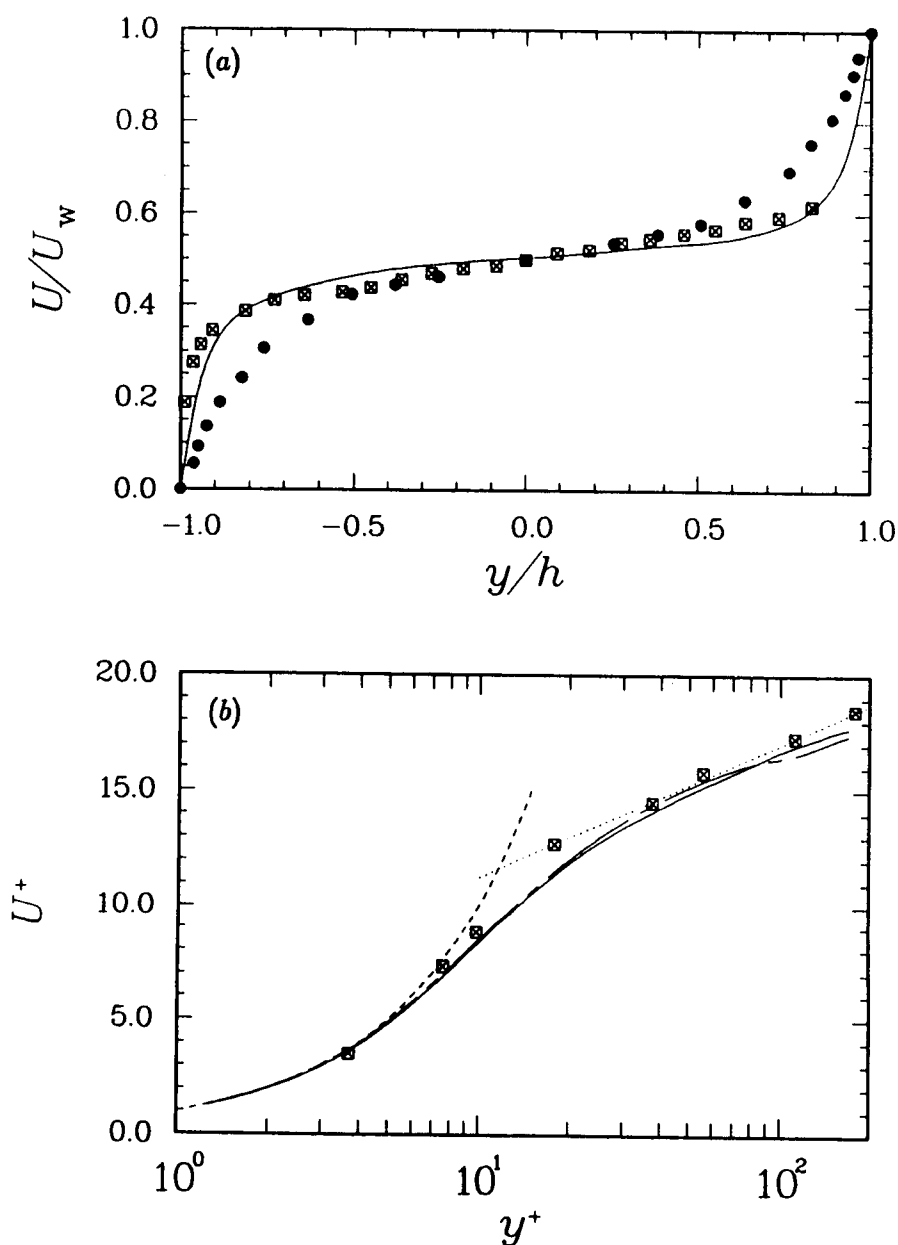


FIGURE 5. Mean velocity profile in plane Couette flow: (a) global profile, U/U_w vs. y/h ; (b) near-wall profile, U^+ vs. y^+ . —, present result; ●, Reichardt (1959); □, El Telbany & Reynolds (1980); ----, $U^+ = y^+$; ·····, $U^+ = (1/\kappa) \ln y^+ + B$ ($\kappa = 0.4$ and $B = 5.5$); In (b), the solid and chain-dashed lines are results for the lower and upper walls, respectively.

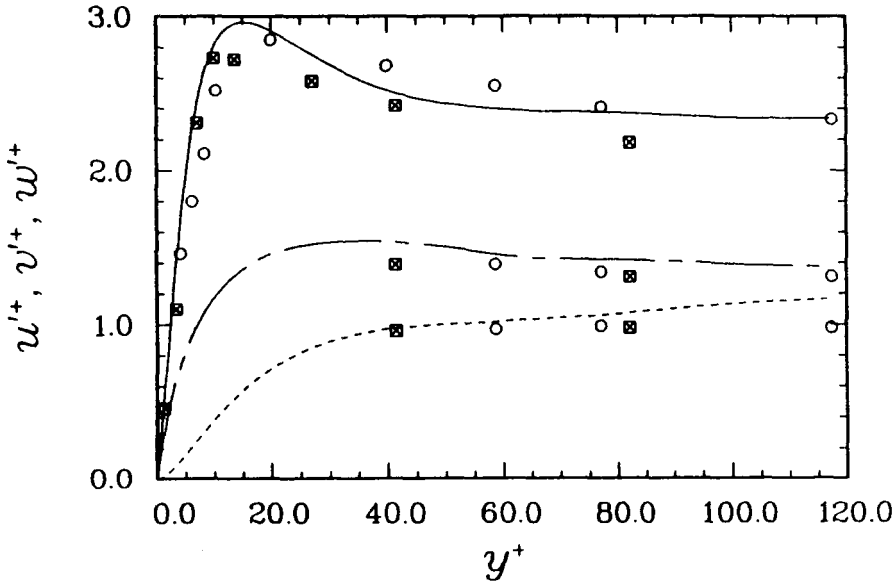


FIGURE 6. Near-wall profiles of the turbulence intensities in plane Couette flow: (u'^+, v'^+, w'^+) vs. y^+ . Lines are present computation: —, u'^+ ; ----, v'^+ ; — · —, w'^+ . Symbols are from El Telbany & Reynolds (1981): \circ , $Re = 19,000$; \boxtimes , $Re = 29,000$.

constant pressure gradient dP/dx (see figure 1), which can be obtained only by solving the equations. Preliminary calculation on a $64 \times 129 \times 64$ grid has been carried with a developed plane Couette flow field as its initial condition; the value of the pressure gradient was varied at each timestep to obtain zero mean shear on the moving wall, and the response of the flow to the varying pressure gradient was found to be slow. Full-scale computation on a $128 \times 129 \times 128$ grid is planned.

2.2. Project B: Axisymmetric-strain/Dilatation RDT

Exact expressions for turbulence structural quantities, such as the Reynolds stresses and vorticity correlations, were obtained in closed form by using rapid distortion theory (Lee 1988). Comparison with the numerical simulations (Lee & Reynolds 1985) at a high strain rate shows remarkable agreement for all the quantities considered. Differences in effects of the two opposite, axisymmetric strain modes (contraction and expansion) on turbulence structure were investigated in detail. For example, axisymmetric contraction produces much higher fluctuation in velocity and vorticity ($R_{ij} = \overline{u_i u_j}$ and $V_{ij} = \overline{\omega_i \omega_j}$, respectively) as well as their anisotropy ($b_{ij} = R_{ij}/R_{kk} - \delta_{ij}/3$ and $v_{ij} = V_{ij}/V_{kk} - \delta_{ij}/3$, respectively) than does axisymmetric expansion. Figures 7(a, b) show comparison of anisotropy development during axisymmetric distortion.

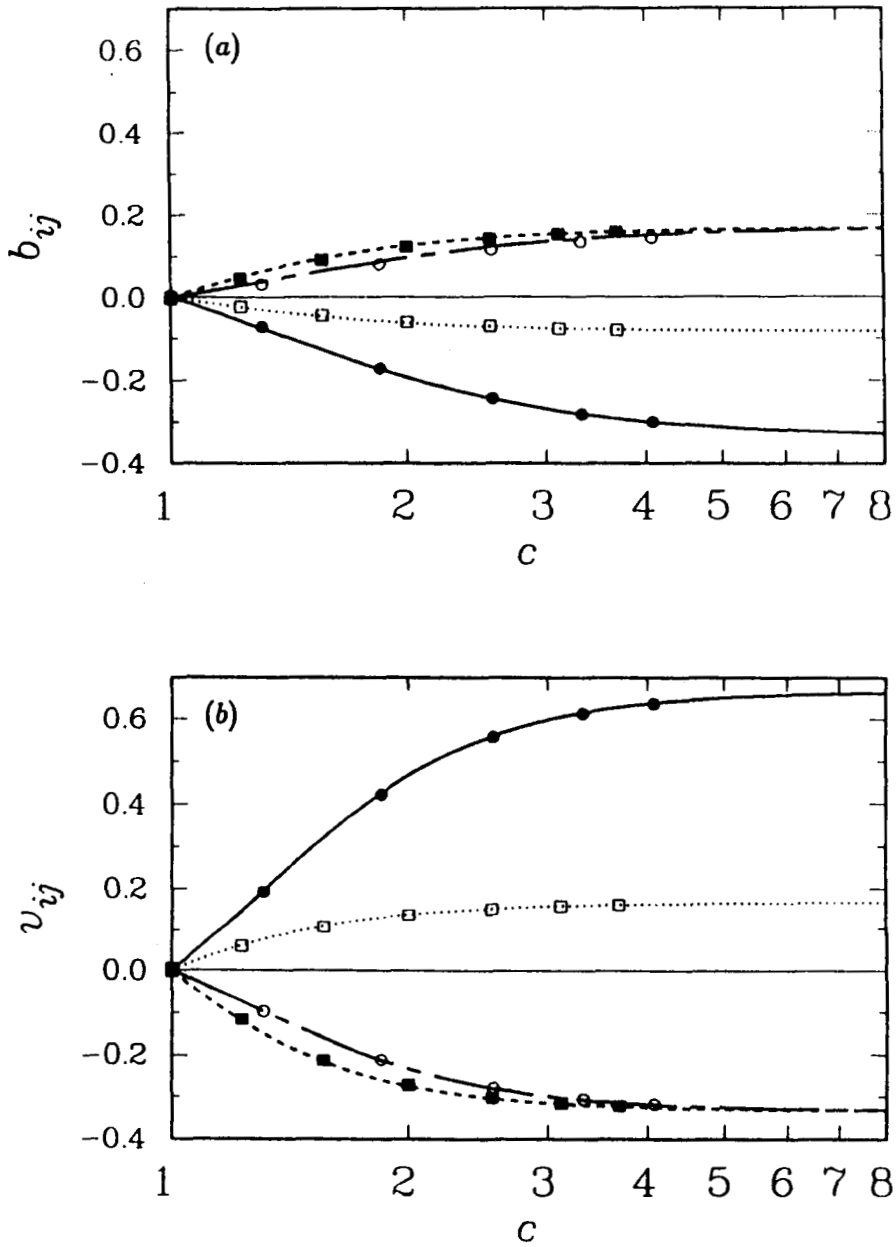


FIGURE 7. Evolution of anisotropy in axisymmetric strain flows (AC, axisymmetric contraction; AE, axisymmetric expansion): (a) Reynolds-stress anisotropy b_{ij} ; (b) vorticity anisotropy, v_{ij} . Lines are RDT results: AC, —, $i=1, j=1$; ---, $i=2, j=2$; AE, ----, $i=1, j=1$; ·····, $i=2, j=2$. Symbols are from numerical simulations (Lee & Reynolds 1985): AC, ●, $i=1, j=1$; ○, $i=2, j=2$; AE, ■, $i=1, j=1$; □, $i=2, j=2$.

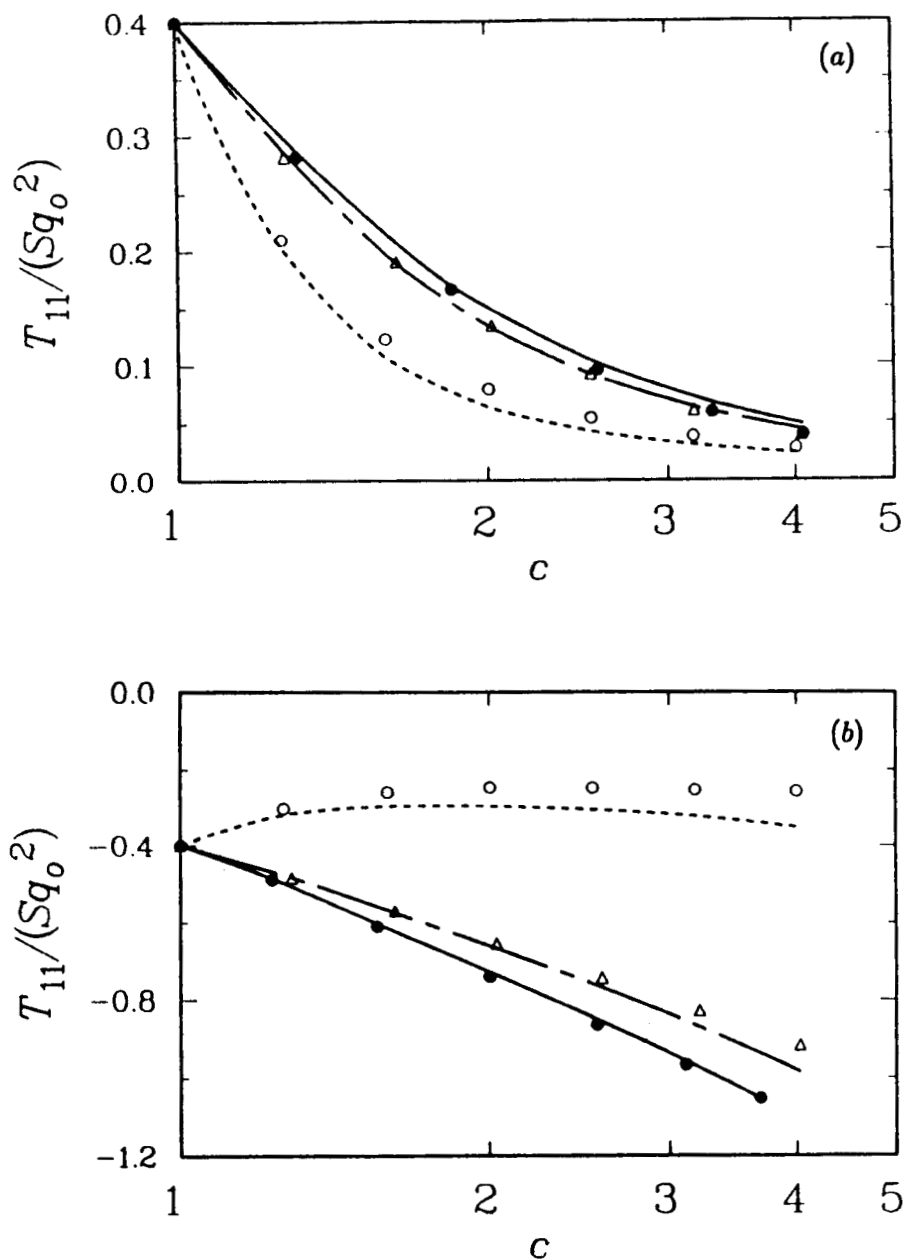


FIGURE 8. Test of the present model against different strain-rate cases, $T_{11}/(Sq_0^2)$: (a) axisymmetric contraction ($S_{11} > 0$); (b) axisymmetric expansion ($S_{11} < 0$). Lines are prediction of the present model and symbols are from numerical simulations (Lee & Reynolds 1985): — and ●, $S^* \approx 100$; --- and △, $S^* \approx 10$; and ○, $S^* \approx 1$.

The effect of mean-field dilatation on turbulence is also of interest. It is shown that, for flows of uniform, time-dependent density $\rho(t)$ at low turbulence Mach number, the statistical correlations, such as the 'Reynolds stress' $R_{ij} = \overline{u_i u_j}$, are related to those in the equivalent incompressible flow by a decomposition of mean strain-rate tensor, e.g. $R_{ij}(\mathbf{e}) = (\rho/\rho_0)^{2/3} R_{ij}^*(\mathbf{e}^*)$ where $\mathbf{e}_{ij} = \int_0^t U_{i,j}(t') dt'$ is the total-distortion tensor and \mathbf{e}_{ij}^* is the corresponding incompressible distortion (ρ_0 is the initial density). Similarly, the vorticity correlation $V_{ij} = \overline{\omega_i \omega_j}$ is given by $V_{ij}(\mathbf{e}) = (\rho/\rho_0)^{4/3} V_{ij}^*(\mathbf{e}^*)$. It was also found that the rate of dilatation does not contribute to pressure fluctuation.

Terms in the transport equation for R_{ij} were evaluated for axisymmetric strain flow, and existing models for the pressure-strain-rate term were examined. It was shown that improvements can be made for the model by incorporating structural parameters based on the linear analysis (RDT) of axisymmetric strain flows. Prediction of the improved model agrees quite well with the numerical simulations, even in cases at lower strain rates (figure 8). This study indicates that a turbulence model should reflect 'history effect,' since a state in nonstationary turbulence depends not only on the instantaneous quantities (e.g. the Reynolds stresses) but also on the memory effect (e.g. total strain) accumulated during a distortion.

2.3. Project C: Energy Transfer Process

A detailed study of the intercomponent energy transfer processes by the pressure-strain-rate in homogeneous shear flow has been carried out by using a numerical database by Rogers *et al.* (1986). In the previous study (Brasseur & Lee 1987), it was found that the rapid and slow parts of fluctuating pressure are uncorrelated, i.e. $\overline{p_r p_s} / (\overline{p_r^2} \overline{p_s^2})^{1/2} \ll 1$, and their scales are widely separated, providing a strong justification for current modeling procedure in which the pressure-strain-rate term is split into the corresponding parts. It was shown that local intercomponent energy transfer processes are associated with high vorticity regions. We limit our discussion to the 'slow' pressure-strain-rate $\phi_{ij} = (2/\rho) \overline{p_s s_{ij}}$.

Our recent study (Brasseur & Lee 1988) of probability density functions (pdf's) and contour plots of the pressure-strain-rate shows that the energy transfer processes are extremely peaky (figure 9), with high-magnitude events dominating low-magnitude fluctuations, as reflected by very high flatness factors (30–40). The concept of the energy transfer class is defined as

$$C^{\pm\pm\pm} = \{\phi_{ij}(\mathbf{x}, t) \mid \phi_{11} \gtrless 0, \phi_{22} \gtrless 0, \phi_{33} \gtrless 0\}.$$

For example, C^{-++} denotes the class of ϕ_{ij} in which energy leaves u ($\phi_{11} < 0$) and enters v and w ($\phi_{22} > 0, \phi_{33} > 0$). Note that this classification of the energy transfer is unique and there are six possible classes which are disjoint (or mutually exclusive). The classification has been applied to investigate details of

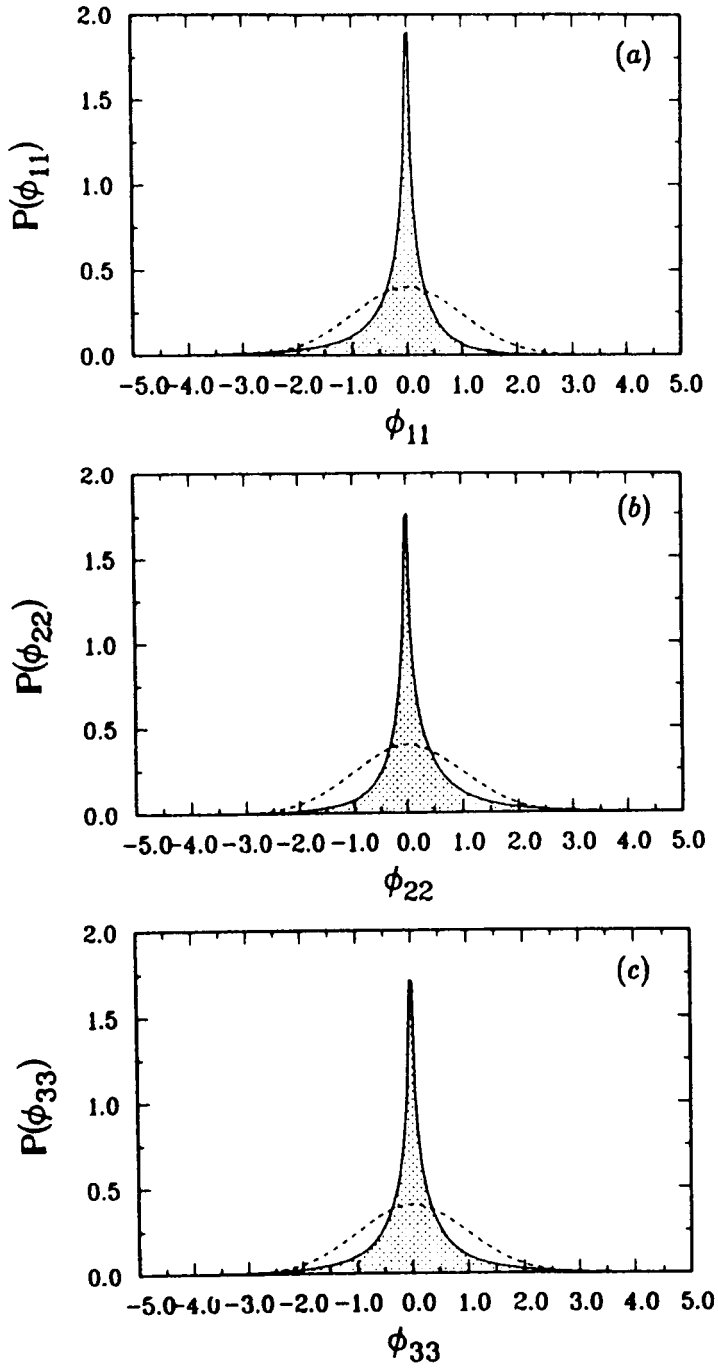


FIGURE 9. Pdf's of the diagonal elements of the slow pressure-strain-rate $\phi_{ij} = ps_{ij}$: (a) $P(\phi_{11})$; (b) $P(\phi_{22})$; (c) $P(\phi_{33})$. ----, Gaussian distribution.

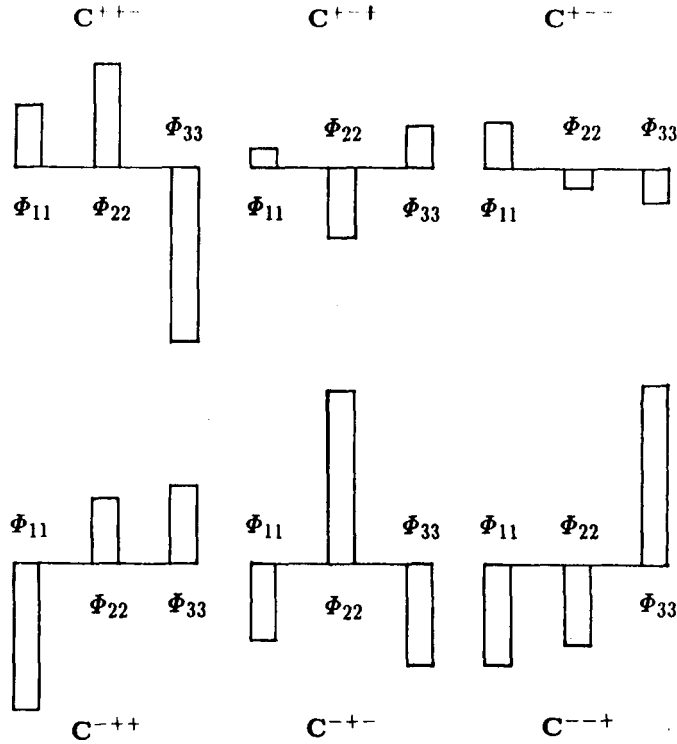


FIGURE 10. Schematic of the intercomponent energy transfer processes, representing contributions from all magnitudes of ϕ_{ij} events. The schematic shows that the four classes C^{++-} , C^{-++} , C^{-+-} and C^{--+} are dominant.

the direction as well as magnitude of the energy transfer processes. Examination of contours in an instantaneous field, pdf's and weighted pdf's of the pressure-strain-rate indicates that in the low-magnitude regions (defined as where $|\phi_{\alpha\alpha}| < 1.5$ r.m.s. $\phi_{\alpha\alpha}$) all six classes are important, but in the high-magnitude regions four classes C^{++-} , C^{-++} , C^{-+-} and C^{--+} dominate. The contribution to the average slow pressure-strain-rate from the high-magnitude fluctuations is only 50% or less, indicating complexity of the problem. However, when summed over all magnitudes, the same four classes of energy transfer dominate as shown by the schematic in figure 10.

3. Future Plan

3.1. Project A: Wall Turbulence

3.1.1. USBL Project

We plan to look into other aspects of the blocking effect of the boundary by examining the two-point correlations between the vertical velocity component

and the streamwise and vertical components. Here, we are interested in assessing the degree of self-similarity of these correlations and seeking possible scaling laws that can be used to develop near-wall turbulence models.

3.1.2. PCF Project

It is anticipated to learn a great deal about how the turbulence structure changes across the interface between the homogeneous core region and inhomogeneous wall region. We are especially interested in examining the structure of *stationary, homogeneous, sheared turbulence* in the core region. The *stationarity and homogeneity* in this flow are generated in a *natural* way, unlike in flows where artificial forcing techniques are used.

3.1.3. SFCF Project

The SFCF project complements the USBL and PCF studies in many respects. While the USBL and PCF projects focus on the role of the mean shear rate in affecting structure of turbulence in wall layer, the SFCF study is designed to study the kinematical nature of the presence of a boundary, i.e. the inquiry into how turbulence is suppressed by the boundary. We expect to learn details of physical mechanisms involving energy redistribution near the boundary, and comparison will be made between the RDT study of shear-free boundary layer, a special case of USBL at $\beta = 0$ (Lee & Hunt 1988). Another impetus to carry out the SFCF project is that this flow allows a unique opportunity to develop a turbulence model for the transport terms, since, in the shear-free wall layer, the transport terms balance the dissipation term in the equation for turbulent kinetic energy.

3.2. Project C: Energy Transfer Process

Inspection of the energy transfer processes depicted in figure 10 poses an interesting question about the kinematic structure of the energy transfer. It appears that the dominant energy transfer to or from one component is provided by the other two components. If the off-diagonal components in ϕ_{ij} are negligible, then most of the energy transfer takes place within axisymmetric flow regimes. The answer awaits invariant analysis of the tensorial structure of the pressure-strain-rate (and strain rate).

In parallel with the intercomponent energy transfer, energy transfer between scales in a flow with coherent vortical structures is also important. In an attempt to generate coherent structures in grid turbulence, Michard *et al.* (1987) used a grid with propellers which give rise to spectral disturbances. Their study showed that the initially strong anisotropy near the grid due to spectral disturbances relaxes to an axisymmetric state. Numerical simulation is planned to investigate such a flow. We are interested in looking into how the disturbances are transferred between components as well as between scales.

Acknowledgements

I would like to acknowledge support from the Center for Turbulence Research. I have been benefitted from many helpful discussions with J. G. Brasseur, J. C. R. Hunt, J. Kim, P. Moin and W. C. Reynolds.

REFERENCES

- BRASSEUR, J. G. & LEE, M. J. 1987 Local structure of intercomponent energy transfer in homogeneous turbulent shear flow. *Proc. Summer Program 1987*, pp. 165–178. Ctr. for Turb. Res., Stanford Univ. and NASA-Ames Res. Ctr.
- BRASSEUR, J. G. & LEE, M. J. 1988 Pressure-strain-rate events in homogeneous turbulent shear flow. *Proc. Summer Program 1988*, pp. 143–156. Ctr. for Turb. Res., Stanford Univ. and NASA-Ames Res. Ctr.
- EL TELBANY, M. M. M. & REYNOLDS, A. J. 1980 Velocity distributions in plane turbulent channel flows. *J. Fluid Mech.* **100**, 1–29.
- EL TELBANY, M. M. M. & REYNOLDS, A. J. 1981 Turbulence in plane channel flows. *J. Fluid Mech.* **111**, 283–318.
- HUNT, J. C. R. 1984 Turbulence structure in thermal convection and shear-free boundary layers. *J. Fluid Mech.* **138**, 161–184.
- HUNT, J. C. R. & GRAHAM, J. M. R. 1978 Free-stream turbulence near plane boundaries. *J. Fluid Mech.* **84**, 209–235.
- KIM, J., MOIN, P. & MOSER, R. D. 1987 Turbulent statistics in fully developed channel flow at low Reynolds number. *J. Fluid Mech.* **177**, 133–166.
- KLINE, S. J., REYNOLDS, W. C., SCHRAUB, F. A. & RUNSTADLER, P. W. 1967 The structure of turbulent boundary layers. *J. Fluid Mech.* **30**, 741–773.
- KREPLIN, H. & ECKELMANN, H. 1979 Behavior of the three fluctuating velocity components in the wall region of a turbulent channel flow. *Phys. Fluids* **22**, 1233.
- LEE, M. J. 1988 Distortion of homogeneous turbulence by axisymmetric strain and dilatation. (Manuscript in preparation for publication.)
- LEE, M. J., COLONIUS, T. & MOIN, P. 1988 The vorticity field associated with the streaks in turbulent shear flows. *Bull. Amer. Phys. Soc.*, **33**(10), 2229.
- LEE, M. J. & HUNT, J. C. R. 1988 The structure of sheared turbulence near a plane boundary. *Proc. Summer Program 1988*, pp. 221–241. Ctr. for Turb. Res., Stanford Univ. and NASA-Ames Res. Ctr.

- LEE, M. J., KIM, J. & MOIN, P. 1987 Turbulence structure at high shear rate. In *Sixth Symp. on Turbulent Shear Flows*, Toulouse, France, Sept. 7-9, 1987 (ed. F. Durst *et al.*), pp. 22.6.1-22.6.6.
- LEE, M. J. & REYNOLDS, W. C. 1985 Numerical experiments on the structure of homogeneous turbulence. *Dept. Mech. Engng. Rep.* TF-24, Stanford University: Stanford, California.
- MICHARD, M., MATHIEU, J., MOREL, R., ALCARAZ, E. & BERTOGLIO, J. P. 1987 Grid-generated turbulence exhibiting a peak in the spectrum. *Advances in Turbulence*, Proc. First Euro. Turb. Conf., Lyon, France, July 1-4, 1986 (ed. G. Comte-Bellot & J. Mathieu), pp. 163-169. Springer-Verlag: Berlin.
- REICHARDT, H. 1959 Gesetzmäßigkeiten der geradlinigen turbulenten Couetteströmung. *Mitt. Max-Planck-Inst. Strömungsforschung und Aerodynamischen Versuchsanstalt*, No. 22.
- ROGERS, M. M., MOIN, P. & REYNOLDS, W. C. 1986 The structure and modeling of the hydrodynamic and passive scalar field in homogeneous turbulent flows. *Dept. Mech. Engng. Rep.* TF-25, Stanford University: Stanford, California.
- TOWNSEND, A. A. 1976 *The structure of turbulent shear flows*. 2nd edn. Cambridge University Press: Cambridge, England.
- UZKAN, T. & REYNOLDS, W. C. 1967 A shear-free turbulent boundary layer. *J. Fluid Mech.* **28**, 803-821.

Direct numerical simulation of compressible free shear flows

By S. K. LELE

Abstract

Direct numerical simulations of compressible free shear layers in open domains are conducted. Compact finite-difference schemes of spectral-like accuracy are used for the simulations. Both temporally-growing and spatially-growing mixing layers are studied. The effect of intrinsic compressibility on the evolution of vortices is studied. The use of convective Mach number is validated. Details of vortex roll up and pairing are studied. A simple explanation of the stabilizing effect of compressibility is offered. Acoustic radiation from vortex roll up, pairing and shape oscillations is studied and quantified.

1. Introduction

Direct numerical simulations have been used to study several incompressible turbulent flows. These studies have ranged from the simulations of homogeneous turbulence (Rogallo, 1981, Lee and Reynolds, 1985, and Rogers, Moin and Reynolds, 1986), to the turbulence in channel flows, (Moser and Moin, 1987, and Kim, Moin and Moser, 1987), boundary layers, (Spalart, 1988), and free shear flows, (Corcos and Sherman, 1984, Corcos and Lin, 1984, Riley and Metcalfe, 1980, Metcalfe et. al., 1987, Lowery and Reynolds, 1986, and Sandham and Reynolds, 1987). The results obtained from the simulations have been extensively compared with the experimental measurements (Kim, Moin and Moser, 1987, Spalart, 1988) and are being used as databases for developing and testing turbulence models (Mansour, Kim and Moin, 1988, and Center for Turbulence Research, 1987), studying the structure and dynamics of organized motions in turbulent flows (Center for Turbulence Research, 1987 and 1988), and testing the accuracy of experimental techniques by Moin and Spalart (1987). On the other hand, the study of compressible turbulent flows is relatively less mature. Most simulations of compressible flows have been limited to the simulation of the large scales of the flow (Winkler et. al., 1987, Smarr et. al., 1984, Woodward, 1984, and Boris, 1988), with some notable exceptions (Feiereisen, Reynolds and Ferziger, 1981, and Passot and Pouquet, 1987). Comparisons with experimental measurements are less detailed in part due to the 'large scale' and two-dimensional nature of most simulations and lack of experimental data on turbulent fluctuations in compressible flows. The renewed interest in the high speed flows, as well as the need to develop turbulence models which incorporate the compressibility effects provide the motivation for the present work. This

paper provides a brief account of results obtained from direct simulations of compressible free shear layers. The simulations resolve all the relevant scales of motion and in particular do not employ any form of filtering or artificial dissipation. Simulations are conducted for both two-dimensional and three-dimensional flows. Most results presented are based on the two-dimensional simulations.

2. Numerical Method

The numerical method used in the study is a compact finite difference scheme of spectral-like accuracy. The details of the numerical scheme have been described in detail elsewhere (Lele, 1988a). The full unsteady equations for mass, momentum and energy conservation are solved for an ideal gas. The Newtonian viscosity law (zero bulk viscosity), and Fourier law of heat conduction are used. Variation of viscosity and thermal conductivity with temperature is permitted. Conservation equation for of a passive scalar (mass fraction) is also solved. Time advancement is carried out by a compact storage third order Runge-Kutta scheme developed by Wray (1987).

The main features of the finite-difference scheme are summarized. The finite difference approximation f'_i to the first derivative $\frac{df}{dx}(x_i)$ at the node i is evaluated by solving a tridiagonal system of the form:

$$\alpha f'_{i-1} + f'_i + \alpha f'_{i+1} = b \frac{f_{i+2} - f_{i-2}}{4h} + a \frac{f_{i+1} - f_{i-1}}{2h}. \quad (1.1)$$

The relations between the coefficients a, b and α are derived by matching the Taylor series coefficients of various order. With

$$a = \frac{2}{3}(\alpha + 2), b = \frac{1}{3}(4\alpha - 1) \quad (1.2)$$

a family of fourth order schemes is obtained. It may be noted that as $\alpha \rightarrow 0$ this family merges into the well known fourth order central difference scheme. Similarly for $\alpha = \frac{1}{4}$ the classical Pade' scheme is recovered. Furthermore for $\alpha = \frac{1}{3}$ the leading order truncation error coefficient vanishes and the scheme is formally sixth order accurate. Most of the simulations presented here use this sixth order scheme. The spectral-like accuracy of the scheme follows from the nature of the dispersive errors associated with (1.1). It may be shown that compared to the traditional finite difference schemes the scheme (1.1) reduces the dispersive errors over a wider band of the length scales represented on the grid. This characterization of the dispersive errors is presented in figure-1. The straight line on the figure represents a spectrally accurate scheme (i.e. exact for all the wavenumbers represented on the mesh). The improved representation of the shorter spatial scales by the present scheme is evident from the figure.

If the dependent variables are periodic then the system of relations (1.1) written for each node can be solved together as a linear system of equations. The

general non-periodic case requires additional relations appropriate for the near boundary nodes. These are described in Lele (1988a). The relation (1.1) along with a mathematically defined mapping between a non-uniform physical mesh and a uniform computational mesh provides derivatives on a non-uniform mesh.

The second derivatives are evaluated by solving a system similar to (1.1), viz.

$$\alpha f_{i-1}'' + f_i'' + \alpha f_{i+1}'' =$$

$$b \frac{f_{i+2} - 2f_i + f_{i-2}}{4h^2} + a \frac{f_{i+1} - 2f_i + f_{i-1}}{h^2}, \quad (1.3)$$

where f_i'' represents the finite difference approximation to the second derivative at node i . With

$$a = \frac{4}{3}(1 - \alpha), b = \frac{1}{3}(-1 + 10\alpha), \quad (1.4)$$

a one parameter family of fourth order schemes is obtained. Again as $\alpha \rightarrow 0$ this family coincides with the well known fourth order central difference scheme. For $\alpha = \frac{1}{10}$ the classical Pade' scheme is recovered. For $\alpha = \frac{2}{11}$ a sixth order tridiagonal scheme is obtained. This scheme with

$$\alpha = \frac{2}{11}, a = \frac{12}{11}, b = \frac{3}{11} \quad (1.5)$$

is used for the simulations presented here. It may also be noted that the schemes (1.3) provide an accurate evaluation of the second derivative over a wide range of length scales. The error associated with the second derivative evaluation for a variety of schemes is shown on figure-2. The spectrally accurate evaluation corresponds to the parabola on the figure. The improvement of the present scheme in representing the shorter scales is again evident from this figure.

Simulations are conducted for both spatially-evolving and temporally-evolving mixing layers. In both cases non-reflecting boundary conditions (Thompson, 1987) are employed at the top and bottom boundaries of the computational domain. In the spatially-evolving case non-reflecting boundary conditions are also used at the inflow and outflow boundaries. The computational grid is uniformly spaced in x (mean flow direction) and z (spanwise direction) and non-uniform in y (transverse to the mean flow). Typically a hyperbolic tangent mapping is used for the non-uniform mesh (in y) with the maximum grid spacing about 2-4 times the minimum grid spacing.

3. Mixing Layer Flows

Direct numerical simulations of mixing layer forming between two streams flowing with speeds U_1 (faster stream) and U_2 were conducted. The two streams were matched in static pressure but, in general, had different fluid densities. Such two stream mixing layers were studied by Brown and Roshko (1974) and subsequently by other investigators. They noted that while the density ratio of the

two streams had a noticeable effect on the spreading rate of the mixing layer it was not enough to explain the slow spreading rate of supersonic mixing layers. Papamoschou and Roshko (1986) (referred to as PR from hereon) showed that this compressibility effect on the spreading rate could be parameterized in terms of a single Mach number, the *Convective Mach Number* M_c , viz. the Mach number defined in a frame of reference moving with the dominant eddies of the flow. They also derived an expression for M_c in terms of the flow conditions of the two streams. Bogdanoff (1983) also suggested the same 'intrinsic Mach number' by a different argument. Recent experiments (Papamoschou, 1988, and Samimy and Elliott, 1988) stability analyses (Sandham and Reynolds, 1989, Ragab and Wu, 1988, Zhuang et. al., 1988) and numerical simulations (Soetrisno et. al., 1988, Lele 1988b) have provided further support to the this notion. Numerical simulations are used to test the notion of the convective Mach number in a fundamental way. Simulations were conducted for three types of mixing layer flows: A) Mixing of streams of equal entropy, B) Mixing of streams of equal stagnation enthalpy, and C) Mixing of streams of equal Mach number. These different classes of mixing layer flows allowed us to vary the Mach number of the individual streams while keeping the convective Mach number fixed. It is thus possible to look for the influence of factors other than the convective Mach number. The spatially evolving simulations presented here were forced at the inflow by adding a v-velocity disturbance velocity of small amplitude (typically with a peak of 1%) to the inflow profiles. This disturbance was confined to the shear layer by means of a Gaussian shape function. It is possible to refine the forcing by using the linear stability eigenfunctions of the inflow profiles. Such a approach was used by Sandham and Reynolds (1987) in simulating incompressible mixing layers. The inflow disturbance contained the most unstable frequency and its first two subharmonics.

In the temporally evolving simulations the initial condition provided the source of disturbance. Small amplitude incompressible disturbances were added to the tangent hyperbolic mean flow profile. Two groups of simulations were conducted. 1) Organized initial conditions - the disturbance contained a small number (typically two) of fourier modes with prescribed phase relations, and 2) Random initial conditions - the disturbance had a white noise wavenumber spectrum with very small (typically 10^{-4} or smaller) amplitude. Both 2-d and 3-d simulations were conducted with the random initial conditions.

The simulations had specific heat ratio, $\gamma = 1.4$, Prandtl number, $Pr = 3/4$, and Reynolds number $R = \frac{\rho_1(U_1 - U_2)\delta_{w_0}}{\mu_1}$ in the range 100-500, where subscripts 1 and 2 refer to the high speed and low speed streams, respectively, and δ_{w_0} is the initial vorticity thickness.

4. Intrinsic compressibility

The definition of a convective Mach number requires one to specify the speed of propagation of the dominant eddies. This speed of propagation was determined

in the numerical simulations from plots of the location of local pressure extremas against time. The pressure maxima correspond to the stagnation points between the vortices, and the pressure minima correspond to the vortex centers. The propagation speed is taken as the slope of these trajectories. An example of such a plot is shown in figure 3 for a class-A flow. For this particular case the Mach numbers of the two streams are 2.0 and 1.2 and the inflow disturbance contains the fundamental and its first two subharmonics. The trajectories of the stagnation points are shown in figure 3a. The location of the vortex centers are displayed in figure 3b. Two generations of pairing events can be seen in these figures. It may be noted that even with the pairing events the stagnation points move with a relatively uniform speed. During the pairing events the downstream vortex slows down while the upstream vortex speeds up. As the vortices pair the stagnation point in their middle is lost. It is also seen that the lower subharmonics tend to modulate the location of upstream pairing events. Varying the frequency of the fundamental disturbance did not alter the propagation speed of the vortices.

PR presented a formula for the vortex propagation speed based on the physical argument that the static pressure at the stagnation point is related to the stagnation pressures in the two streams by the isentropic relation. This convection speed formula was tested against the numerical simulation results at three different velocity ratios and several convective Mach numbers. The agreement between the observed speed and the formula is excellent in all the simulations (discrepancy of 1 – 2 %). It may be noted that when the specific heat ratio of the two gases is the same, the PR formula reduces to the formula proposed by Dimotakis (1984) for the propagation speed of vortices in incompressible shear layers. Thus fluid compressibility appears to have very little influence on the propagation of two-dimensional vortices.

The spatial growth rate of the mixing layer depends both on the growth measured in the convected frame of reference (temporal growth) and the convection speed of the vortices. Having verified that the convection speed is independent of the compressibility, compressibility effects in the spatial growth of the layer are studied. Figure 4 shows an example of the downstream evolution of three measures of mixing layer thickness. These are: 1) Thickness based on the Reynolds-averaged mean flow profile, 2) Thickness based on the Favre-averaged mean flow profile, and 3) Thickness based on the mean potential vorticity profile. For the example displayed, the layer was forced at the most unstable frequency with a 5 % forcing amplitude. The three cases (one from each class) have M_c of about 0.4 and the same velocity ratio $\frac{U_2}{U_1}$ of 0.6. The thickness is normalized by the initial thickness and the downstream distance is normalized by $10 \delta_{w_0}$. It may be seen when M_c is the same the spatial growth rate for the three cases is similar but not identical. The differences that remain arise from the dependence of the nondimensional convection speed $\frac{U_c}{U_1}$ on the density ratio $\frac{\rho_2}{\rho_1}$. Case C has the slowest propagation speed giving the fastest spatial growth, while case B has

the fastest propagation speed and the slowest growth. A visual picture of the spatially evolving mixing layers is presented in figure-5. Contours of vorticity are plotted for three simulations with M_c about 0.4. The simulations were forced with the fundamental and two subharmonics. Vortex pairing events noted in figure-3 can be visually seen in these contours. It may also be noted that the vortices are most evolved in case C (slowest propagation speed).

Results obtained from the vortex roll up in temporally growing mixing layers are presented to further verify this density ratio effect on $\frac{U_c}{U_1}$. The temporal simulations are conducted in a frame of reference moving with $U_c = \frac{a_1 U_2 + a_2 U_1}{a_1 + a_2}$, a_1 and a_2 being the sound speeds in the two streams. In this way the density ratio effect is removed. The initial amplitude in all the temporal simulations is 1 %. In figure 6 two examples are shown with M_c of about 0.4. The first case has streams with equal static temperature, i.e. $T_2 = T_1$ (class A) and the second case has streams with equal total temperature, i.e. $h_{01} = h_{02}$ (class B). Thickness measures (1) and (2) defined above are displayed against time normalized by $\frac{10\delta_{\omega 0}}{U_1 - U_c}$. It may be noted that the time histories are almost identical.

Experiments have documented the reduction in the growth rate of compressible shear layers as M_c is increased (PR). This reduction is most easily understood in terms of the behavior of the temporally-evolving layer. In figure 7 we show the time history of thickness measure (2) for several different M_c . The stabilizing influence of M_c is clearly seen. It has been suggested that the slow growth arises primarily due to the reduced linear instability growth rate (PR and Sandham and Reynolds, 1989).

In the next section we present a physical argument for this stabilizing effect.

5. Evolution of the vorticity field

The linear instability process leads to a reorganization of the vorticity field. The inviscid vorticity equation for the two dimensional flow may be written as:

$$\frac{\partial \omega}{\partial t} + U_c \frac{\partial \omega}{\partial x} = -(u - U_c) \frac{\partial \omega}{\partial x} - v \frac{\partial \omega}{\partial y} - \omega \nabla \cdot \vec{u} + \frac{\nabla \rho \times \nabla p}{\rho^2}$$

showing that the rate of change of vorticity observed by an observer moving at speed U_c is due to three effects. 1) Advection relative to the observer (first two terms on the r.h.s.), 2) Change due to compression of fluid elements (third term), and 3) Baroclinic change (fourth term). The individual terms for a class A mixing layer at M_c of 0.4 are shown in figure 8. It may be noted that the most important term causing the vorticity redistribution is the advection term. Advection may be seen as moving vorticity away from the stagnation region and bringing it to the vortex centers. This is precisely the incompressible instability mechanism causing the shear layer instability. The compression term, while not dominant at $M_c = 0.4$, provides clues on how the stabilizing effect associated

with compressibility arises. A simple explanation of the stabilizing effect of compressibility is presented below. In figure 10 a schematic picture of the flow field around the vortices is presented in a frame of reference moving with speed U_c , the speed of the vortices. As shown earlier the 'stagnation points' between the vortices also move at the same speed and thus are stationary in this frame. Fluid moving away from the stagnation points expands as it accelerates towards the vortex center. Past this point the flow compresses and decelerates towards the other stagnation point. This expansion and compression process may be seen in the characteristic quadrupole pattern of the dilatation field. The expansion and compression cycle has the effect of increasing the vorticity near the stagnation points and reducing it near the vortex center. This is exactly opposite of the redistribution arising from the advection term (the driving cause of instability). The numerical simulations show that as M_c is increased the vorticity compression effect becomes comparable in magnitude to the advection term.

In class A flows, the baroclinic change is an order of magnitude smaller than the other terms. In class B and C flows, the density of the two streams are unequal and this generates strong baroclinic torques. This is essentially an incompressible effect and arises whenever a density gradient exists across the shear layer. As the roll up proceeds this density interface remains sharp at the 'braids' and the pressure maximum (at the stagnation point in the convected frame) produces regions with dynamically significant baroclinic torque. For class B flows, the density of the low speed stream is always lower, thus the baroclinic torques tend to enhance the vorticity in the lower part of the braid and cause suppression of vorticity in the upper part of the braid. For class C flows, the density of the high speed stream is lower and a reversal of the situation just described takes place. The vortices evolving in class B and class C flows have a layered vorticity distribution. The baroclinic effect strongly modifies the vorticity distribution in the vortices. This mechanism of generation of baroclinic torques is shown in figure 9 for a class C flow. The net circulation of the vortices, however, remains relatively uninfluenced by this redistribution.

6. Flows with eddy shocklets

For M_c around 0.7 and larger, the flow fields develop eddy shocklets. These shocks remain attached to the vortices and travel with them. For $M_c = 0.7$ the shocks arise during the vortex pairing events, but the flow field is otherwise shock free. For $M_c = 0.8$ the shocklets are produced during the roll up. An example of flow fields with eddy shocklets is displayed in figure 11. Just as observed at lower M_c the flow accelerates and decelerates around the vortices. Now, however, there are local regions where the relative Mach number of unity is exceeded, and near the vortex this supersonic flow slows down by first going through a shock, becoming subsonic, and then decelerating further by compressing towards the stagnation points. The regions of expansion are now more spread out and the regions of compression more compact (essentially

within the eddy shocklets). The increase of the vorticity due to the compression in the shock, as well as the increase in entropy is clearly observed. This flow field is remarkably similar to typical transonic flow past an airfoil. The induced velocity pattern associated with the fluid expansion and compression opposes the entrainment velocity induced by the clumped vorticity field. This may cause a further reduction in the entrainment of fluid into the layer.

7. Acoustic radiation from vortex evolution

Numerical simulations have been used to study the acoustic radiation arising from the unsteady processes of vortex roll up, pairing, shredding, and shape oscillations. The acoustic efficiency for these processes has been studied at several Mach numbers. At low Mach number less than 0.1% of the energy extracted from the mean flow is radiated. This fraction increases to 1-2 % at M_c of 0.6. A full account of these studies will be presented elsewhere (Lele and Ho, 1989). Here we present one example to illustrate the behavior. The example chosen corresponds to a temporally-growing mixing layer. The computation uses non-reflecting boundary conditions based on characteristic variables. These allow the acoustic waves to leave the computational domain. The example discussed here has $M_c = 0.6$, a value for which we find significant departures from the low Mach number aero-acoustic theory. The computational domain contains two wavelengths of the most unstable disturbance. The layer first rolls up to form two vortices which later pair to form a larger vortex. After the pairing the vortex continues to undergo shape oscillations for several cycles. This behavior is illustrated in figure 12 where the time history of layer thickness is plotted. The corresponding time history of pressure, velocity component normal to the layer, and the acoustic flux of energy leaving the domain near the bottom are also shown in this figure. Pressure is normalized as $\frac{p/p_\infty - 1}{M_c^2}$, velocity as $\frac{v/a_1}{M_c}$, and acoustic flux in terms of these normalized values. The roll up, pairing and nutation processes can be identified in these figures. The roll up and pairing cause the layer thickness to increase and generate a compression wave. Subsequent to pairing, the nutation of the vortices causes a periodic energy exchange between the vortices and the mean flow. This process generates a series of compression and expansion waves which carry acoustic energy away from the layer. The numerical simulations show that the nutation frequency is close to $\frac{\omega}{2}$, where ω is the peak vorticity.

In figure-13 the acoustic radiation for three different cases are compared. All case were for $M_c = 0.4$, but differed in the initial disturbance. Case-1 contained only the fundamental disturbance (case-1), case-2 only the subharmonic disturbance, and case-3 contained both the fundamental and the subharmonic. It is evident (as anticipated by Laufer (1974)) that in case-3 the vortex merger produces the strongest acoustic radiation (8 times that in case-1 and twice that of case-2). In the time history of the acoustic signal the signals arising from the rollup and pairing can be separately identified. The acoustic signal from rollup

contains a compression wave followed by a more spread out expansion wave while the acoustic signal from pairing generates more symmetric compression and expansion waves.

8. Simulations with random initial conditions

Temporally evolving mixing layer flows were simulated starting from very low level (peak amplitude 10^{-4}) white noise (equal amplitude to all fourier modes with uncorrelated phases). Both two-dimensional and three-dimensional simulations were conducted. The computational box was chosen to be 12 times the most unstable wavelength (based on the initial profile). The initial evolution of the disturbances corresponded to the predictions of the linear stability analysis. In figure-14 the exponential growth rates obtained from two such simulations are shown. The two cases correspond to $M_c = 0.4$ and $M_c = 0.8$. The wavenumber and the growth rate are scaled with the local values of the vorticity thickness. The time scale is normalized by $\frac{\delta_w}{U_1 - U_2}$ in this figure. During this phase of exponential amplification the layer grew in a laminar fashion. As the disturbances became nonlinear the harmonics of the linearly unstable disturbances began to amplify. With significant vorticity clumping the growth rates became larger than the 'laminar instability' estimates. The nonlinear process generated a broadband spectrum. In this regime a linear spreading of the mixing layer was observed. In figure-15 data from three simulations are presented. It may be seen that for $M_c = 0.4$ and $M_c = 0.6$ a constant spreading rate was observed, with slower growth for $M_c = 0.6$. It was verified that for M_c lower than 0.4 the growth rate was not further increased. The temporal growth rate obtained for $M_c = 0.4$ is close to 0.1 a value consistent with previous incompressible simulations Lesieur (1987). For $M_c = 0.8$ the growth was slow and dominated by a laminar process. Later in time (outside the time range shown) vortices formed in the layer but the computational domain contained too few of them to constitute an adequate statistical sample. The convective Mach number concept was also tested with random initial conditions. In figure-16 the time evolution of two run with the same M_c of 0.4 but different density ratios are compared. The temporal growth rates were quite close (though not identical).

In figure-17 snapshots of the vorticity field are displayed for the case with $M_c = 0.4$. The frames are equally separated in time. It may be seen that the linear instability process selects a length scale for the vortices. This length scale does not correspond to the most unstable wavelength of the initial profile. This is because the initial disturbance level was very low, allowing the layer to viscously thicken ($Re_{\delta_{w_0}} = 400$). The length scale chosen by the flow corresponds to the most unstable wavelength at a later time (end of the laminar spreading regime in fig. 15). After the vortices form they undergo the merging instability. Since the vortices had a phase jitter the merging is also randomized. Figure-18 presents similar snapshots for the mixing layer at $M_c = 0.6$. It maybe noted that the length scale selected by the flow is larger. This is consistent with the

linear instability behavior. The phase jitter in the vortices is again visible. Such phase jitter allows the turbulence statistics to evolve in a self-similar manner. Figure-19 presents some of these statistics at four instants in the evolution (from the linearly spreading regime). The y-coordinate in the plots is scaled with the instantaneous vorticity thickness and the fluctuations are scaled by half the velocity difference across the layer. The mean velocity profiles are closely self-similar. The Reynolds stress is also close to being self-similar. The r.m.s. u and r.m.s. v (titled as u prime and v prime) have larger departure from self-similarity. Later in the evolution as the second pairing takes place the computational box contains too few vortices ('independent' samples) and the layer departs from self-similarity. As noted earlier the nonlinear process generate higher harmonics and create a broadband spectra. In figure-20 spectra of the fluctuating fields are plotted at various times. The spectra were obtained by fourier decomposing the fields in the periodic direction. The wavenumber was normalized with the initial vorticity thickness. The plots show the spectra obtained by integrating the energy associated with each fourier mode across the layer. The simulation start from a low level white noise. Linear instability selectively amplifies the unstable modes. Later in time the spectra fill up in the harmonics and finally become broadband. It is possible to see a shift in the peak of the spectra to low wavenumbers (since the layer grows in time). Even at late times the energy level of the broadband fluctuations is quite low. Previous studies of incompressible mixing layer (Lesieur, 1987) have suggested a -4 slope in the broad band portion. Such a spectral slope may be seen in the present simulations. Interestingly the low wavenumber portion of the pressure spectrum is very much like the velocity spectrum, but at higher wavenumber the pressure spectrum drops more rapidly.

This work was presented at the AIAA meeting in Reno, 1989. It is available as AIAA paper AIAA-89-0374 from AIAA.

REFERENCES

- BOGDANOFF, D. W. 1983 *AIAA J.*, **21**, 926-927.
- BORIS, J. P. 1988 in Proceedings of the conference on 'Physics of Compressible Turbulent Mixing', Princeton. (see also Oran, E.)
- BROWN, G. L. AND ROSHKO, A. 1974 *J. Fluid Mech.*, **64**, 775-816.
- CENTER FOR TURBULENCE RESEARCH 1987 *Studying Turbulence using Numerical Simulation Databases*, Proceedings of the 1987 Summer Program, Report CTR-S87, Stanford University.
- CENTER FOR TURBULENCE RESEARCH 1988 *Studying Turbulence using Numerical Simulation Databases - II*, Proceedings of the 1988 Summer Program, Report CTR-S88, Stanford University.
- CORCOS, G. M. AND SHERMAN, F. S. 1984 *J. Fluid Mech.*, **139**, 29-65.

- CORCOS, G. M. AND LIN, S. J. 1984 *J. Fluid Mech.*, **139**, 67-95.
- DIMOTAKIS, P. E. 1984 AIAA paper, AIAA-84-0368.
- FEIEREISEN, W. J., REYNOLDS, W. C. AND FERZIGER, J. H. 1981 Dept. of Mech. Engrg., Stanford University, Report No. TF-13.
- KIM, J., MOIN, P. AND MOSER, R. D. 1987 *J. Fluid Mech.*, **177**, 133-166.
- LAUFER, J. 1974 *Omaggio a Carlo Ferrari*, 451-464.
- LEE, M. J. AND REYNOLDS, W. C. 1985 Dept. of Mech. Engrg., Stanford University, Report No. TF-24.
- LELE, S. K. 1988a submitted to *J. Comput. Phys.*
- LELE, S. K. 1988b in Proceedings of the conference on 'Physics of Compressible Turbulent Mixing', Princeton.
- LELE, S. K. AND HO, C. M. 1989 in preparation.
- LESIEUR, M. 1987 *Turbulence in fluids*, M. Nijhoff Publishers, Chapter 8, p253.
- LOWERY, P. S. AND REYNOLDS, W. C. 1986 Dept. of Mech. Engrg., Stanford University, Report No. TF-26.
- MANSOUR N. N., KIM, J. AND MOIN, P. 1988 *J. Fluid Mech.*, **194**, 15-44.
- METCALFE ET. AL. 1987 *J. Fluid Mech.*, **184**, 207-243.
- MOIN, P. AND SPALART, P. R. 1987 NASA TM-100022.
- MOSER, R. D. AND MOIN, P. 1987 *J. Fluid Mech.*, **175**, 479-510.
- PAPAMOSCHOU, D. AND ROSHKO, A. 1986 AIAA paper, AIAA-86-0162.
- PAPAMOSCHOU, D. 1988 in Proceedings of the conference on 'Physics of Compressible Turbulent Mixing', Princeton.
- PASSOT, T. AND POUQUET, A. 1987 *J. Fluid Mech.*, **181**, 441-466.
- RAGAB, S. A. AND WU, J. L. 1988 AIAA paper, AIAA-88-0038.
- RILEY, J. J. AND METCALFE, R. W. 1980 AIAA paper,
- ROGALLO, R. 1981 NASA TM-81315.
- ROGERS, M. M., MOIN, P. AND REYNOLDS, W. C. 1986 Dept. of Mech. Engrg., Stanford University, Report No. TF-25.
- SAMIMY, M. AND ELLIOTT, G. S. 1988 AIAA paper 88-3054A.
- SANDHAM, N. D. AND REYNOLDS, W. C. 1989 AIAA paper, AIAA-89-0371.
- SANDHAM, N. D. AND REYNOLDS, W. C. 1987 in *Turbulent Shear Flows - VI*, Toulouse, France.
- SMARR, L. L., NORMAN, M. L. AND WINKLER, K-H. A. 1984 *Physica D*, **12**, 83-106.

- SOETRISNO, M., EBERHARDT, S., RILEY, J. J., AND MCMURTY, P.
1988 AIAA paper, AIAA-88-3676.
- SPALART, P. R. 1988 *J. Fluid Mech.*, **187**, 61-98.
- THOMPSON, K. W. 1987 *J. Comput. Phys.*, **68**, 1-24.
- WINKLER ET. AL. 1987 *Phys. Today*, October, 28-37.
- WOODWARD, P. 1984 L. L. L. preprint UCRL-90662.
- WRAY, A. A. 1987 submitted to *J. Comput. Phys.*
- ZHUANG, M., KUBOTA, T. AND DIMOTAKIS P. 1988 in Proceedings of the
1st National Fluid Dynamics Conference, Cincinnati. 88-3583-CP.

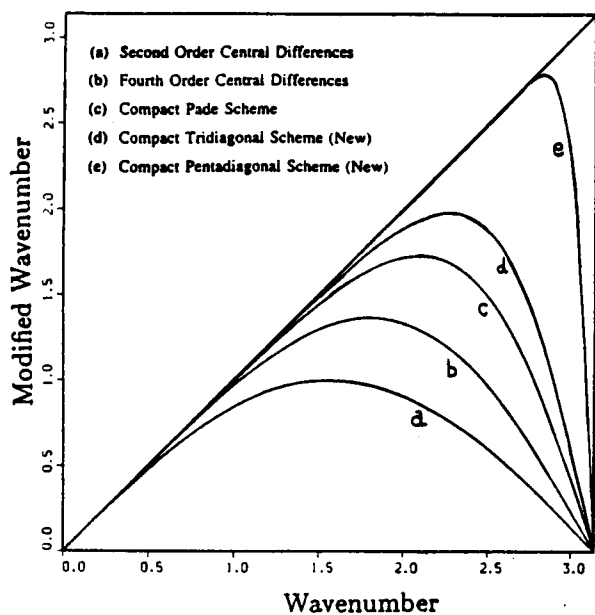


Figure 1 Modified wavenumber analysis for the approximations to the first derivative.

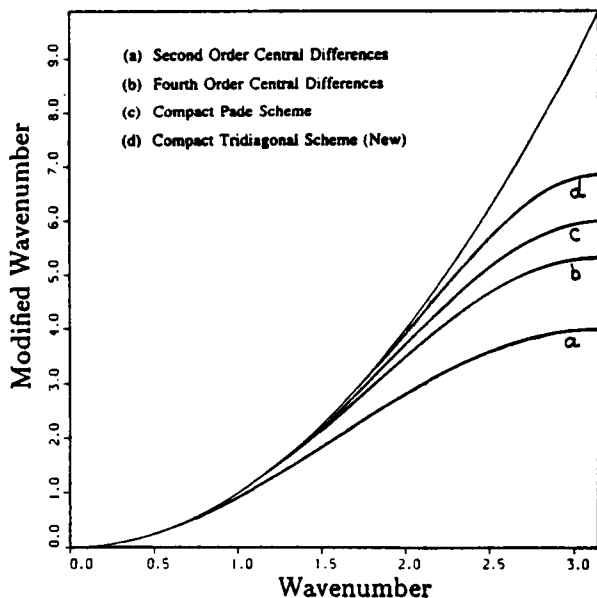


Figure 2 Modified wavenumber analysis for the approximations to the second derivative.

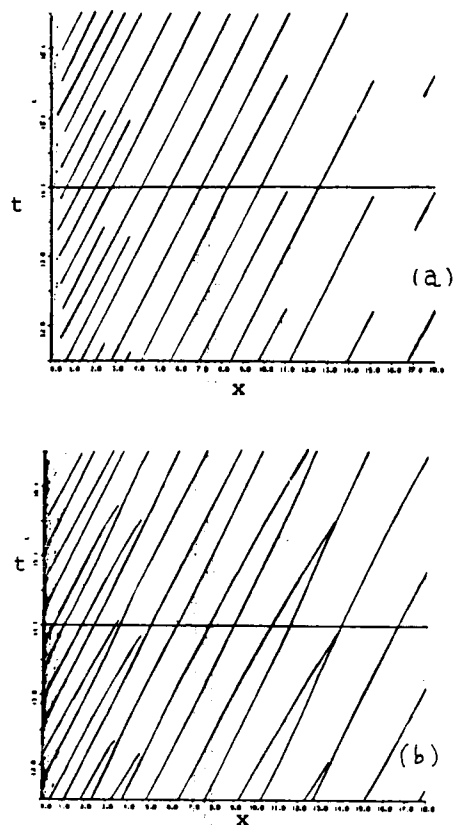


Figure 3 Trajectories of pressure extrema in a spatially evolving mixing layer. Pressure maxima shown in a) correspond to the stagnation points in the convected frame and pressure minima shown in b) correspond to the vortex centers.

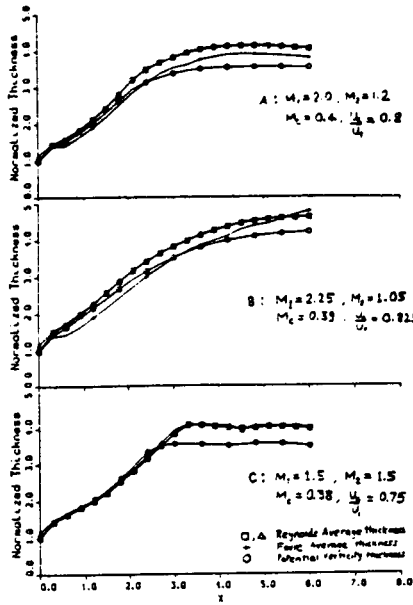


Figure 4 Streamwise evolution of mixing layer thickness measures. All cases have U_1/U_2 of 0.8, M_c about 0.4 and the same inflow forcing. The difference in the growth rates is due to the different density ratios. A) $T_1 = T_2$, B) $T_{01} = T_{02}$, C) $M_1 = M_2$.

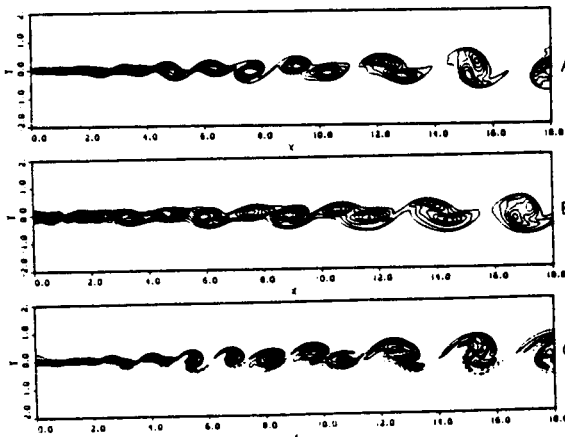


Figure 5 Vorticity contours in spatially evolving mixing layers. All cases have U_1/U_2 of 0.8, M_c about 0.4 and the same inflow forcing. A) $T_1 = T_2$, B) $T_{01} = T_{02}$, C) $M_1 = M_2$.

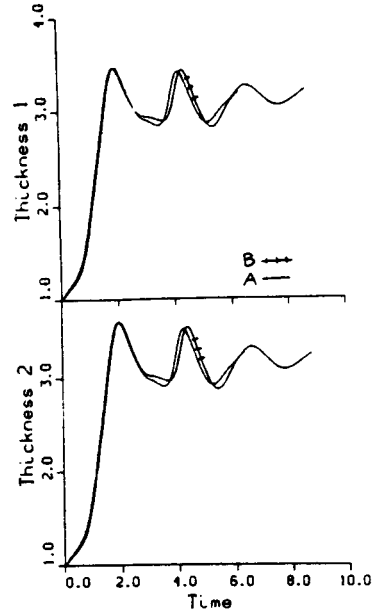


Figure 6 Temporal evolution of mixing layer thickness measures. Both cases have the same $M_c = 0.38$, A) $T_1 = T_2$, B) $T_{01} = T_{02}$.

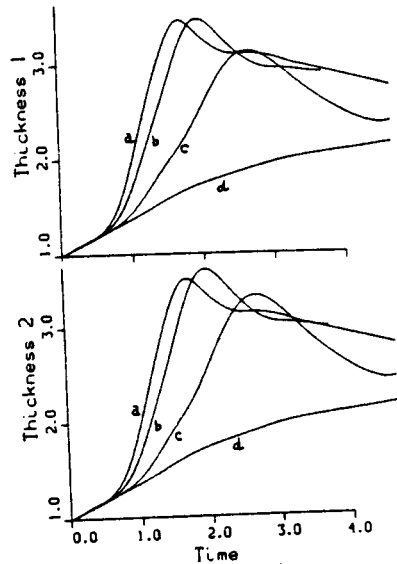


Figure 7 Temporal evolution of mixing layer thickness measures for different M_c . All cases are from class A: a) $M_c = 0.2$, b) $M_c = 0.38$, c) $M_c = 0.6$, d) $M_c = 0.8$.

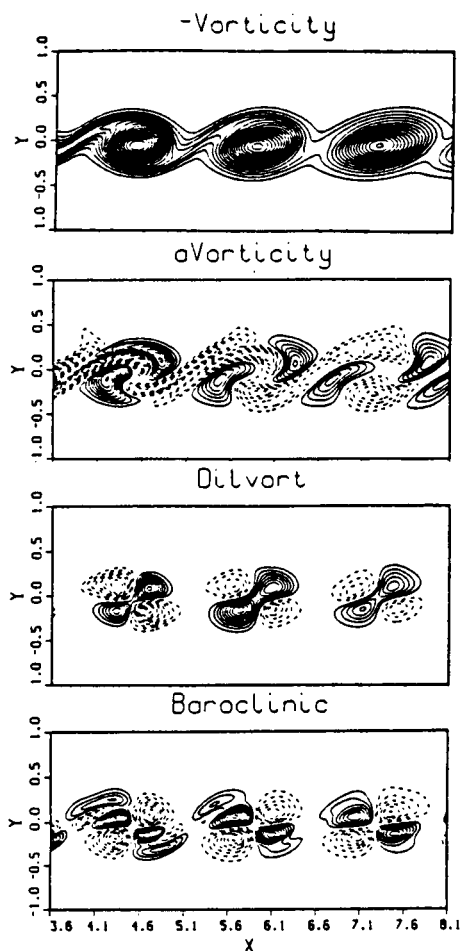


Figure 8 Vorticity evolution for class A mixing layer. $M_1 = 2.0$, $M_2 = 1.2$, $M_c = 0.4$. The panels are : vorticity field, advection term in moving frame (-0.91 to 0.76), vorticity compression term (-0.22 to 0.25), and baroclinic term (-0.03 to 0.04), respectively.

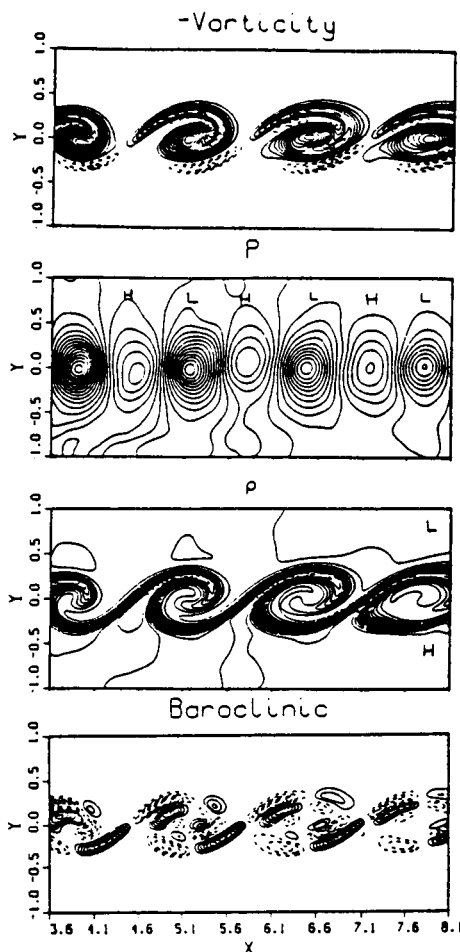
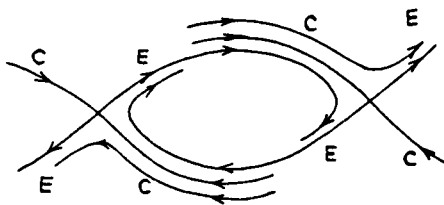


Figure 9 Vorticity evolution for class C mixing layer. $M_1 = 1.5$, $M_2 = 1.5$, $M_c = 0.38$. The baroclinic terms are comparable to the vorticity advection and produce the layered vorticity profiles. The panels are : vorticity field, pressure field, density field, and the baroclinic term, respectively.



E : Expansion
 $\nabla \cdot \mathbf{u} > 0$
C : Compression
 $\nabla \cdot \mathbf{u} < 0$

Figure 10 A schematic of the flow field in a frame of reference moving with the vortices.

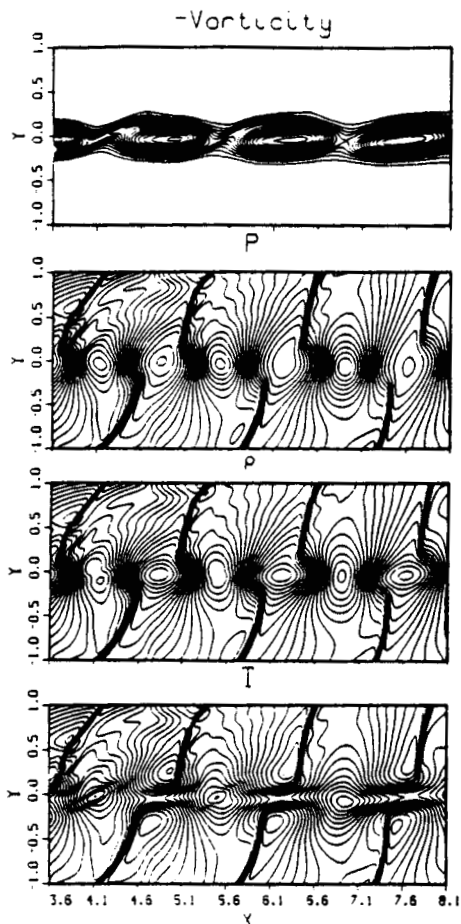


Figure 11 Vortex evolution with eddy shocklets. The example shown is for class A mixing layer. $M_1 = 4.0$, $M_2 = 2.4$, $M_c = 0.8$. The panels present the vorticity field, pressure field, density field, and temperature field, respectively.

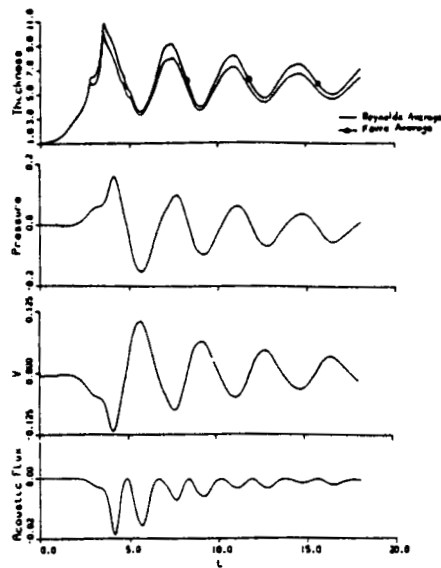


Figure 12 Acoustic radiation from vortex pairing and shape oscillation. $M_c = 0.6$. Time history of mixing layer thickness measures, normalised pressure, normalised v velocity, and normalised acoustic flux at the bottom boundary.

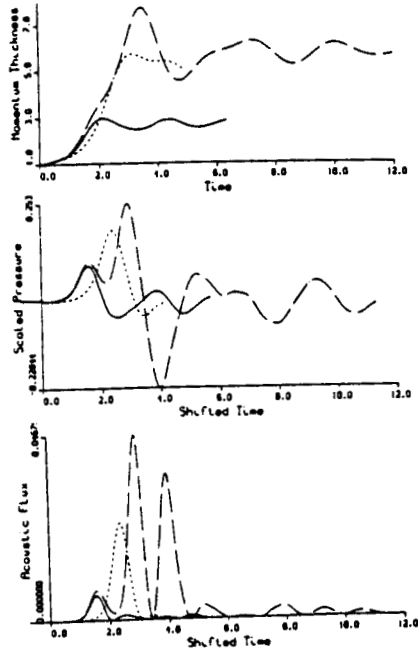


Figure 13 Acoustic radiation from vortex evolution. All cases have $M_c = 0.4$. Case-1 (solid) has only the fundamental disturbance, 2) only the subharmonic disturbance (dashed) and 3) both together (chain). The normalised pressure signal in the far-field and normalised acoustic flux at the top boundary are shown.

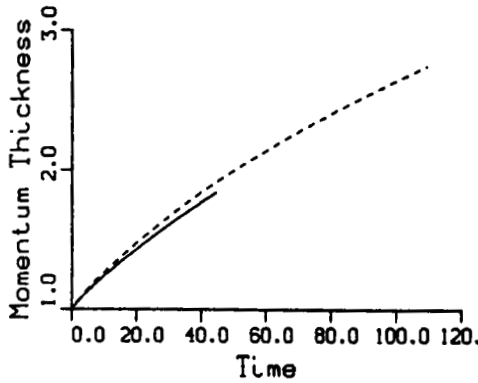
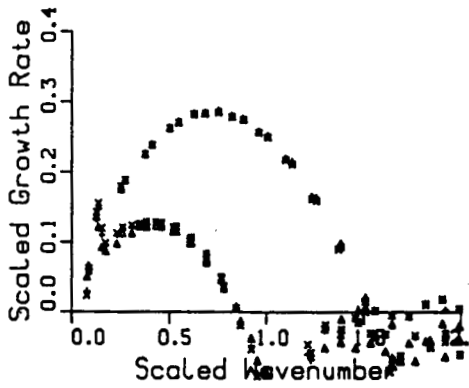


Figure 14 Growth rates for different fourier modes for $M_e = 0.4$ (solid) and $M_e = 0.8$ (dashed). During this phase laminar spreading is observed.

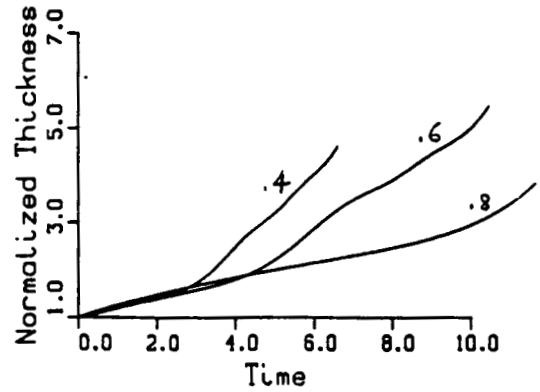


Figure 15 Mixing layer growth for different M_e . The curves correspond to $M_e = 0.4, 0.6$ and 0.8 .

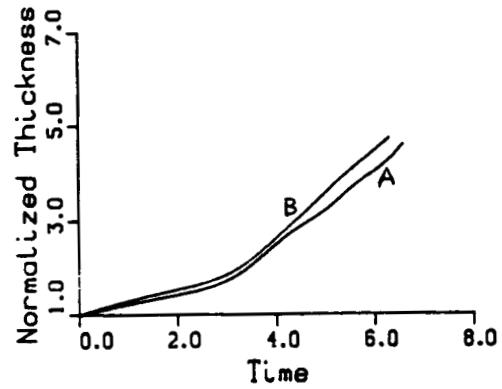


Figure 16 Mixing layer growth at $M_e = 0.4$. A) $T_1 = T_2$, B) $T_{0,1} = T_{0,2}$.

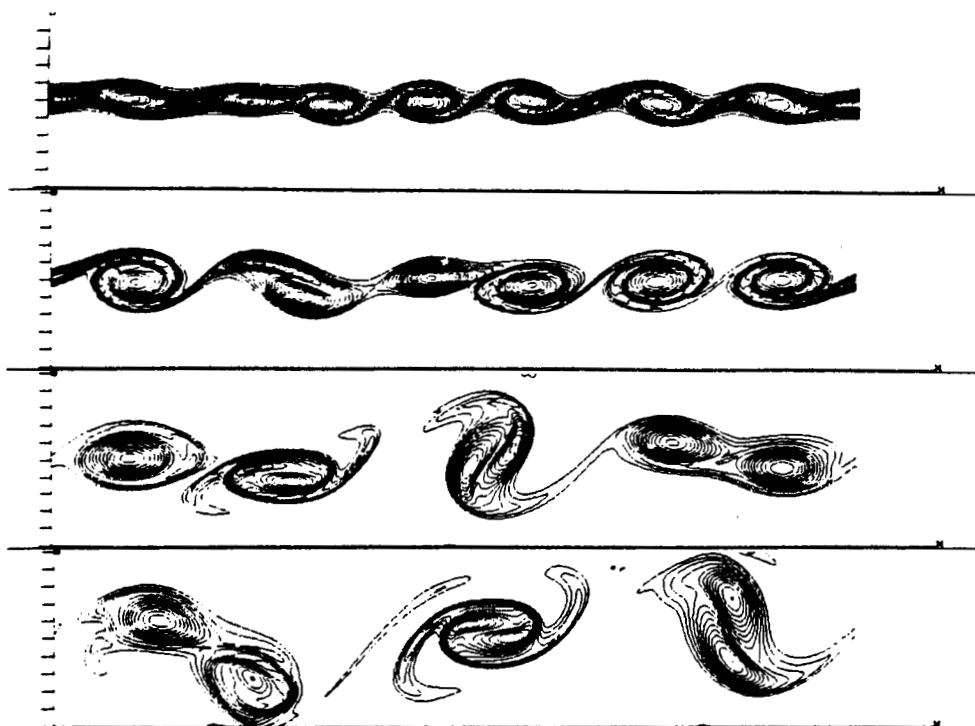


Figure 17 Snap shots of mixing layer evolution at $M_c = 0.4$. Contours of vorticity are shown.

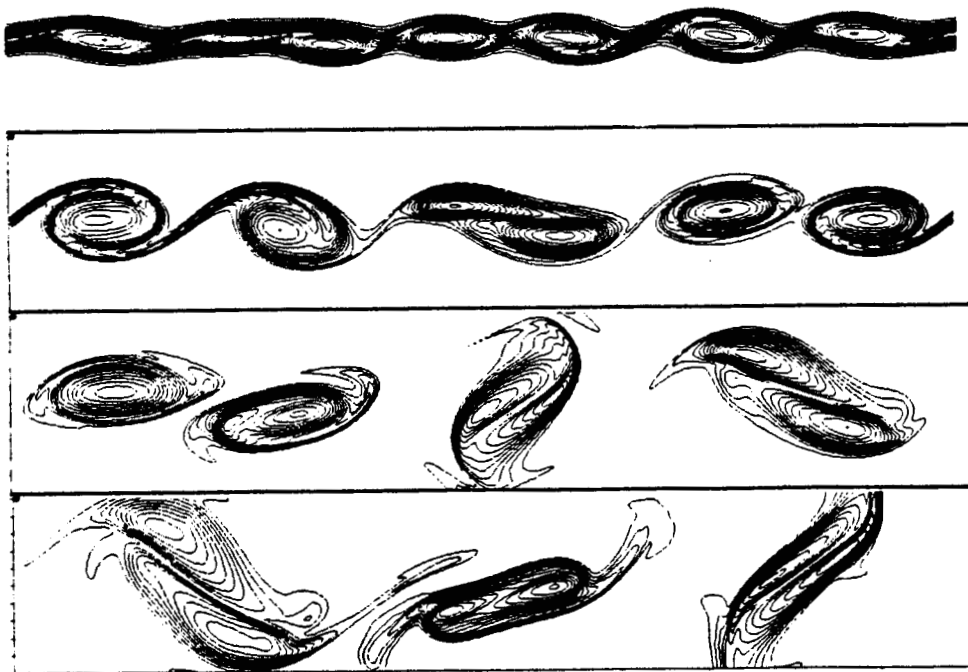


Figure 18 Snap shots of mixing layer evolution at $M_c = 0.6$. Contours of vorticity are shown.

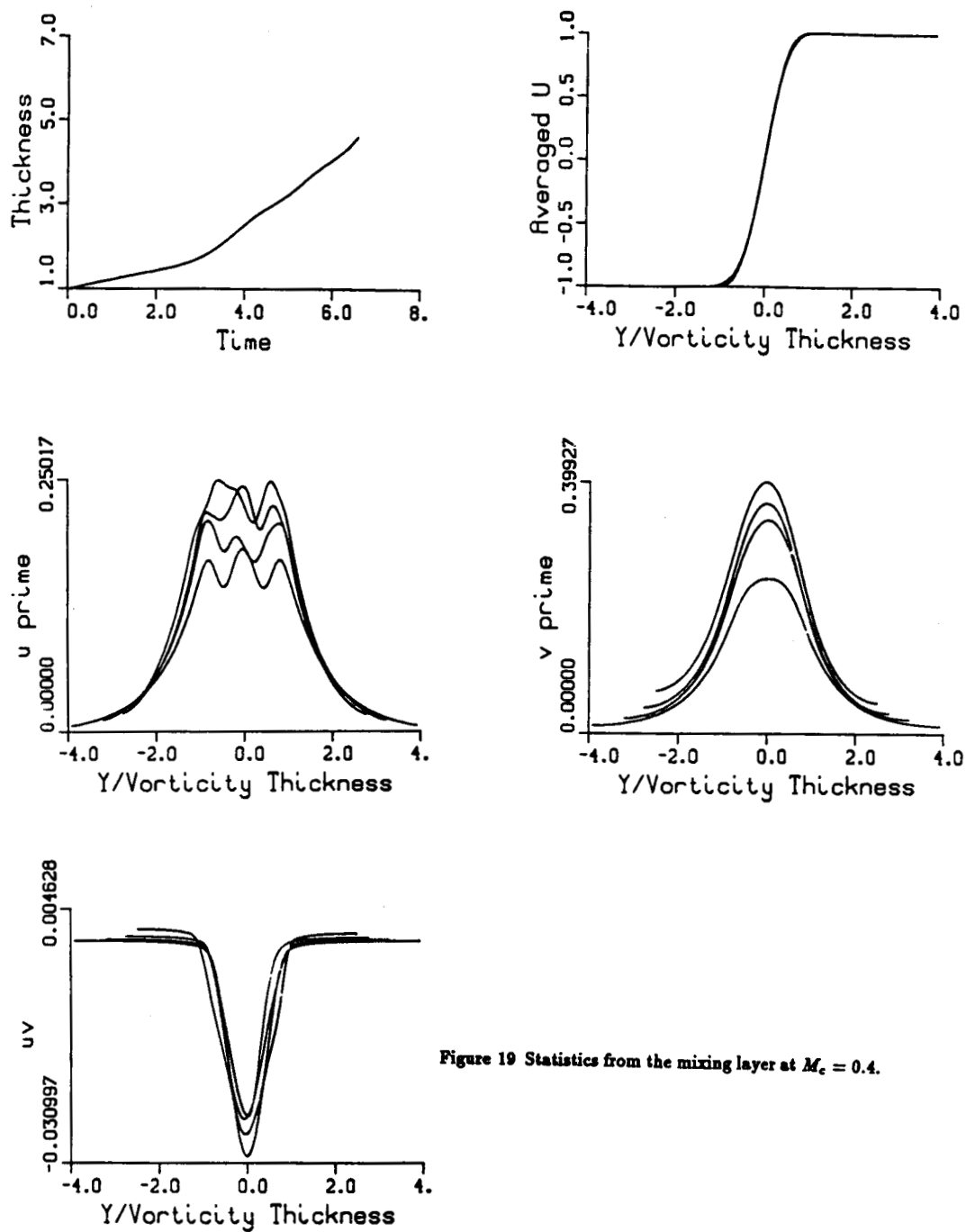


Figure 19 Statistics from the mixing layer at $M_c = 0.4$.

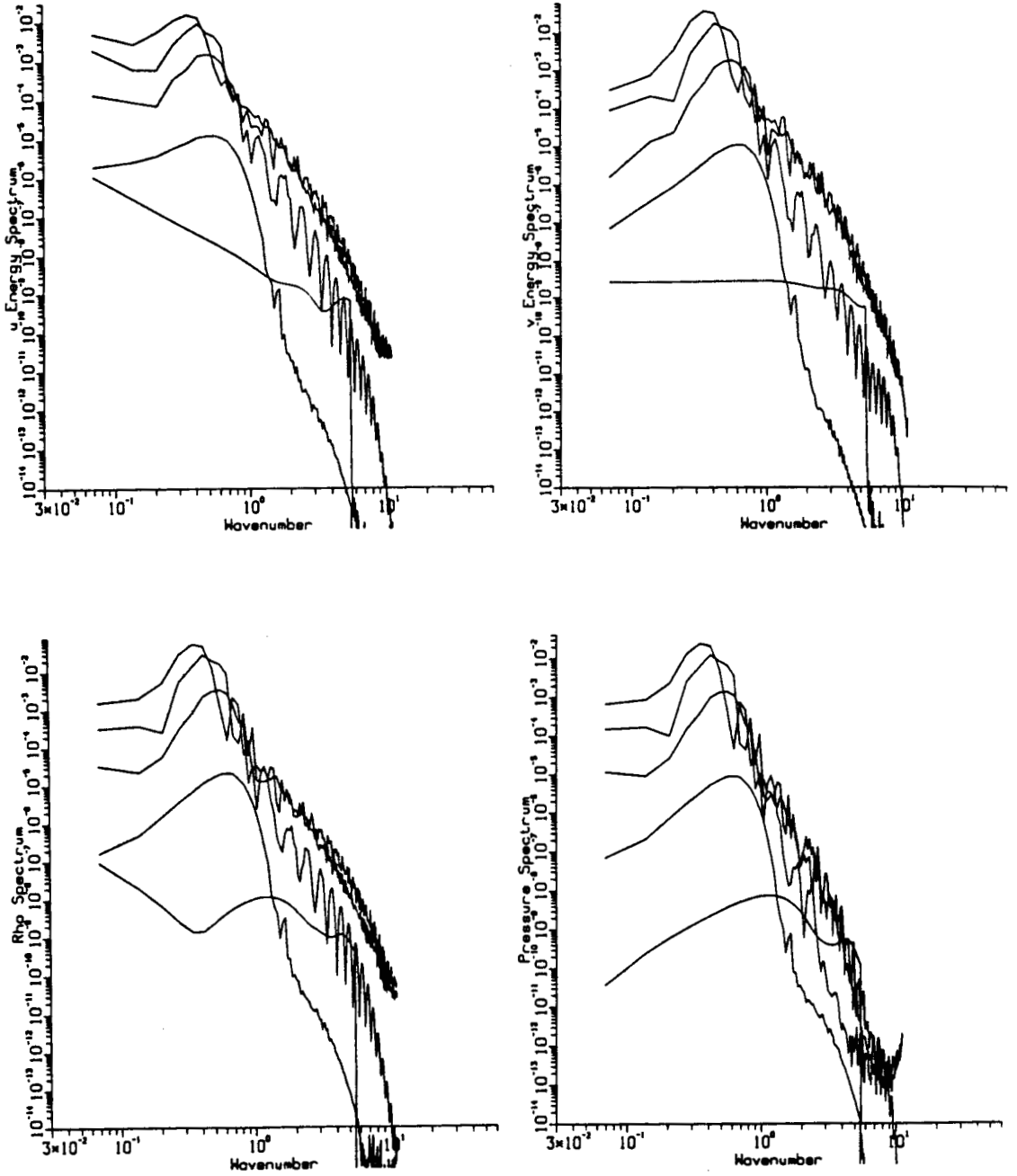


Figure 20 Spectra of fluctuations in mixing layer at $M_c = 0.4$.

Direct simulation of compressible reacting flows

By T. J. POINSOT

Summary

A research program for direct numerical simulations of compressible reacting flows is described. Two main research subjects are proposed: the effect of pressure waves on turbulent combustion and the use of direct simulation methods to validate flamelet models for turbulent combustion. The interest of a compressible code to study turbulent combustion is emphasized through examples of reacting shear layer and combustion instabilities studies. The choice of experimental data to compare with direct simulation results is discussed. A tentative program is given and the computation cases to use are described as well as the code validation runs.

1. Introduction

A considerable part of progress to be made in future years in the field of turbulent combustion studies might be achieved through direct simulation methods. These methods have already demonstrated their possibilities in the case of non-reacting flows, and there is little doubt that they will be as powerful in the case of reacting flows. However, such progress will require considerable improvements of existing direct simulation codes to account for specific phenomena occurring in reacting flows. One of the most important issues in this field is to take into account the compressibility effects. This should be done at different levels by incorporating the following effects:

- 1- *density variations generated by heat release*
- 2- *acoustic waves*
- 3- *strong compressibility effects due to high relative Mach numbers*

These three steps represent growing complexity. It is rather obvious that *density variations* generated by heat release strongly modify the velocity field and the strain rates, changing the turbulent field and, therefore, the combustion rate itself. Therefore, direct simulations aimed at studying cold flames (essentially flames with constant density) can not predict the behavior of real flames. This does not mean that these simulations are not interesting: they retain many features of real flames like chemical and diffusive mechanisms. Building a code for direct simulation of flames with non constant density does not necessarily mean using a compressible code. Random vortex methods as well as spectral methods can provide such capacity without taking compressibility effects into account (Ghoniem and Sethian 1987, Riley et al 1986, Givi and Metcalfe 1986).

Nevertheless, ability to include compressibility is highly desirable because it fulfills not only criterion 1 but also the two others: computing acoustic waves and mean pressure gradients.

Experimental results suggest that *acoustic waves* are of primary importance for combustion problems (Poinso et al 1986, Darabiha et al 1985) but also for non-reacting flows. Non-reacting shear layers exhibit phenomena where acoustic waves play an important role by introducing a feedback loop through which phenomena occurring downstream (for example a vortex coalescence) can send information upstream (to the vortex shedding region) and create a locking phenomenon (Ho and Huerre 1984, Ho and Huang 1982). This locking may be weak or strong. We will call it weak when it does not lead to an instability where the acoustic field becomes intense. This is the case in most ducted shear layers. It should not be concluded that *weak coupling means no effect of acoustic waves*: even if the acoustic field is not intense, vortex shedding can be very sensitive to pressure waves, and this point is seldom taken into account in direct simulation methods.

In non-reacting shear layers the coupling may become strong as, for example, in the case of the edgetone experiment. Placing an obstacle in the shear layer can amplify the acoustic feedback and lead to the production of a highly coherent and intense sound generated by the coupling between coherent structures in the shear layer, their impact on the obstacle, and the acoustic waves in the flow (Ho and Nosseir 1981, Tang and Rockwell 1983, Knisely and Rockwell 1982).

When combustion takes place, the coupling is even enhanced by the reaction taking place in the flow structures. Experimentally, this coupling is strong enough in many situations to induce very large oscillations of all the flow parameters and lead to complete extinction by blow off or flash back of the flames. Although it does not always lead to such extreme instabilities, we have to suppose that this coupling can be an important part of the global behavior of turbulent reacting flows and, therefore, incorporate acoustic waves in our model.

It is possible to ask whether we really need direct simulation codes to study interactions between combustion and acoustic waves and whether we could simplify the problem and for example assume that acoustic waves and turbulence act independently on the flow. Acoustic waves in usual systems have large wavelengths compared to the reaction zone thickness, and we might try to disconnect the effects of pressure waves and those of turbulence. Such attempts have been made to compute combustion instabilities in the 'Thin Flame' models proposed by Yang and Culick (1986) or Poinso and Candel (1988). In these models the interaction between combustion and turbulence is represented simply by a turbulent flame speed while all interactions between the flame movements and the acoustic field are explicitly computed. Poinso and Candel (1988) show that these models are unable to predict any turbulent combustion instability if the turbulent flame speed does not depend on the local turbulence or on the local

pressure. This shows that pressure waves and turbulence have strong interactions and that this coupling must be explicitly taken into account. This requires the use of a direct simulation code (for turbulence estimation) which must be compressible (for acoustic waves computation).

The last case requiring compressible computations is clearly obtained for flows exhibiting *high relative Mach numbers* such as supersonic reacting flows. Compressibility is not limited to the flow perturbations (as it was for acoustic waves) in these cases but is a basic characteristic of the mean flow itself. Compressible calculations are obviously required for this situation.

Looking at all these cases is far beyond the scope of this work. Therefore, I have chosen to concentrate this study on two generic cases of compressible reacting flows which offer a very wide range of interests:

- ▷ *Effect of acoustic waves on reacting and non-reacting shear flows*
- ▷ *Validation of flamelet models for turbulent combustion*

2. Effect of pressure waves on turbulent combustion

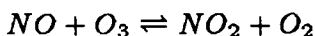
Acoustic waves play an important role in non-reacting as well as reacting flows. As most experiments are performed in ducts, the acoustic modes of these ducts are first choice candidates to excite the flow to study. Therefore, many experimental shear layers are controlled mainly by acoustic excitations (Ho and Huerre 1984). We will start this work by looking at the effects of acoustics in the non-reacting mixing layer and afterwards proceed to the reacting case. In these two situations, the questions addressed will be essentially the same:

- How should excitation be introduced in the direct simulation to correspond to experiments? Exciting the shear layer at its most amplified hydrodynamic frequency is clearly not compatible with all experimental data: many experiments exhibit a sensitivity to acoustics that must be considered (Masutani et al 1986, Poinso et al 1987). Exciting the flow with an acoustic frequency of the duct might be an interesting alternative, but the best technique would be to introduce initial perturbations on different oscillation modes (acoustic and random modes) and let the system evolve without other excitation (Poinso and Candel 1988). The use of reflecting boundary conditions for acoustic waves should insure that the flow keeps being excited by its own oscillations. It is interesting to note that this method has already been used successfully to predict coalescence in free shear layers (Grinstein et al 1987) and theoretically confirm the feedback law proposed by Laufer (see Ho and Huerre 1984).

- What acoustic modes are involved in the locking phenomena?
- How does the flow respond to acoustic excitations, and what kind of locking can be isolated from the results? For this study, the reacting case might be simpler than the non-reacting case because of generation of acoustic disturbances by non steady combustion in vortices.

Many experiments have been conducted on shear layers and could be used to validate the results obtained from direct simulation. After a preliminary study,

however, the experiment of Masutani and Bowman (1986) on a reacting shear layer appears as a good choice because it was performed in the premixing domain where three dimensional effects are reduced and for Reynolds numbers which are accessible to direct simulation. All computations will be two dimensional. One of the streams will contain nitrogen and nitric oxide while the other contains nitrogen and ozone. Either reactant (nitric oxide or ozone) can be injected in the high speed side. The Reynolds number based on the vorticity thickness and the velocity difference will vary between 300 and 2000. The chemistry can be represented by only one reaction namely:



This paper provides many experimental data such as mean profiles, RMS profiles, PDFs and power spectra density at different locations for reacting and non reacting cases. These data should constitute a good and critical basis for code testing.

3. Validation of flamelet models for turbulent combustion

Flamelet models for turbulent combustion are the subject of growing interest. In these models, turbulent combustion is modelled as a collection of small laminar flamelets which are convected, stretched, and quenched by turbulence without losing their laminar structure. These assumptions allow a computation of the mean turbulent reaction rate using only two informations:

- 1- the laminar flame speed of the flamelets
- 2- the topology of the flamelets ensemble

Computing the laminar speed and the extinction limits of stretched flames has become a relatively easy task (Giovangigli and Smooke 1987) and different data bases giving flame speeds for various flow parameters are or will be available in the near future. Defining the topology of the flamelets is a much more difficult task and constitutes the basic problem of flamelet modelling.

A powerful flamelet model has been proposed by Marble and Broadwell (1977) and developed by S. Candel and coworkers (1988) (see also Darabiha et al 1987). In this model called the *Coherent Flame Model (CFM)* the topology of the flamelets is described only by their surface Σ , the flame front surface per unit mass of gas (the flame front surface per unit volume of gas $\rho\Sigma$ is more convenient to use). This approach requires the chemical time to be smaller than the turbulent times so that the flame is essentially wrinkled and stretched by turbulence but that it remains a continuous interface separating burnt and fresh gases. An equation is written for this flame surface and coupled with the flow properties: turbulence field, chemical data, etc. The laminar flame speed is obtained from a data base containing computations of strained laminar flames at stagnation point with complete chemistry. The interesting feature in the model is its ability to handle chemical problems on one side to obtain the local flame

speed of the flamelets and the turbulence-combustion interaction on the other side through the flame surface equation. Although the CF model has already been successfully applied in different practical combustion systems, its complete validation will certainly be easier if direct simulation is used to ascertain most of the assumptions made to obtain the *flame surface equation*. This equation describes the evolution of the flame surface in each computational cell. Like the equations derived in turbulence modelling for the turbulent kinetic energy or the dissipation rate, this equation requires modelling of many physical mechanisms (Marble and Broadwell 1977, Candel et al 1988):

- convection of the flamelets by the mean flow
- diffusion of the flamelets by turbulence
- flamelet stretching by the turbulent field (which is a source term for the flame surface equation)
- annihilation of flamelets by mutual interactions (which is a sink term for the flame surface equation).

$$\frac{\partial \rho \Sigma}{\partial t} + U \frac{\partial \rho \Sigma}{\partial x} + V \frac{\partial \rho \Sigma}{\partial y} = E \rho \Sigma + \text{Diffusion Term} - \text{Annihilation Term}$$

The term $E \rho \Sigma$ represents the flame surface increase due to the stretching of the flame front by the turbulent flow and is the dominant term in the flame surface equation. E is the stretch rate and might be easily obtained as $\sqrt{\varepsilon/\nu}$ if chemistry was infinitely fast and the flame was an infinitely thin interface (ε is the turbulent dissipation rate and ν is the kinematic viscosity). This is not the case, and because of chemical effects, most flamelets will be quenched if they are submitted to high stretch rates. Therefore, one of the first difficulties is to give a proper estimate of E taking into account all possible interactions between the flame front and the turbulent field. Assumptions are usually made for each of these terms, but very few validations of these hypotheses exist. For example, Marble and Broadwell (1977) estimated E in a reacting shear layer to be of the order of $\frac{\partial U}{\partial y}$ which is a proper estimate of the stretch rate of the large eddies in the layer but does not include any chemical effects. The interaction of a laminar flame and a vortex has already been studied analytically (Cetegen and Sirignano 1987) and numerically (Candel and Laverdant 1987) but recent direct simulation results performed on the structure of premixed flames interacting with a vortex show more complete and promising results (Rutland and Ferziger 1989).

We intend to extend these studies to test and improve some of the modelling assumptions used in flamelet models by studying simple interactions between a laminar flame front and an imposed vorticity field. This will be done on a diffusion flame in a shear layer or on a laminar premixed flame propagating in a duct and submitted to a vortex. In these two cases, the initial flame structure will be that of a laminar flame and the objective will be to study how this structure interacts with the vorticity field generated by the shear layer or by

the isolated vortex. The flame surface will be tracked and compared to the computation given by the flame surface equation of the CF model using the same input values for strain rates. The computations will be two dimensional. The main parameters will be the Damkohler number based on the chemical time and the roll up time of the eddy. Following problems will be more precisely considered:

- In which range of Damkohler numbers does the initial flame retain its laminar structure? (In other words can we use the flamelet concept to describe turbulent combustion at this Damkohler number?)

- What are the local values of the strain rates, and is there any evidence of flame extinction by strain?

- How must the CF model equation for the flame surface be modified to predict correctly results given by the direct simulation? How is the effective stretch rate E given by the direct simulation related to the flow vorticity and to the flame chemical time?

- What is the effect of eddies smaller than the flame front thickness? (High values of Damkohler numbers). Can the flamelet concept be extended to regimes where turbulence does not only wrinkle and stretch the flame but also thickens it?

One may note that acoustic waves are not a first order phenomenon in this part of the work but that variable density effects certainly are. Density variations will affect the flow and hence will modify the flamelet strain rate which is one of the major parameters in flamelet models. It is also clear that all issues cited above might not be completely treated in the limited time devoted to this study.

4. Program

This work will be done starting with the code developed by Dr. S. K. Lele at NASA Ames. This code is fully compressible and it will be modified and used in two different versions:

- Version 1 will have essentially the same base than the original code, will deal only with non-reacting flows, and will specifically address the effects of acoustic waves on vortex shedding and growth. It will also be used for the implementation of new boundary conditions and excitation methods adapted to acoustic treatments and different validation tests.

- Version 2 will have chemical reactions. This will require different modifications of the code and also some basic validation tests such as computation of laminar flames.

These two versions will be developed and used together. Since September 1st., Version 1 has been modified to provide easy pre- and postprocessing and is presently used to test the code performances on acoustic waves computations and implement more complex boundary conditions. Version 2 is being modified at the same time but will not be used before first validation tests of Version 1 will be finished.

REFERENCES

- CANDEL S., MAISTRET E., DARABIHA N., POINSOT T., VEYNANTE D. & LACAS F. 1988 *Marble Symposium* August 1988, CALTECH, Pasadena.
- CANDEL S. & LAVERDANT A. 1987 *AIAA Paper 87-1779* San Diego, California.
- CETEGEN & SIRIGNANO 1987 *AIAA Paper 87-* San Diego, California.
- DARABIHA N., GIOVANGIGLI V., TROUVE A., CANDEL S. & ESPOSITO 1987 *US-France Joint Workshop on Turbulent Reactive Flows* Rouen, France.
- DARABIHA N., POINSOT T., CANDEL S. & ESPOSITO E. 1985 *Progress in Astro. and Aero.* 283-295.
- GHONIEM A. F. & SETHIAN J. A. 1987 *AIAA J.* 25.
- GIVI P., JOU W. H. & METCALFE R. W. 1986 *21st Symp. (Int) on Combustion* 1251-1261.
- HO C. M. & HUERRE, P. 1984 *Ann. Rev. Fluid Mech.* 16, 365-424.
- HO C. M. & HUANG L. S. 1982 *J. Fluid Mech.* 119, 443-473.
- HO C. M. & NOSSEIR N. S. 1981 *J. Fluid Mech.* 105, 119-161.
- GRINSTEIN F. F., ORAN E. S. & BORIS J. P. 1987 *AIAA J.* 25, 1, 92-98.
- GIOVANGIGLI V. & SMOOKE M. 1987 *J. of Comp. Physics* 6, 327-345.
- KNISELY & ROCKWELL 1982 *J. Fluid Mech.* 116, 157-186.
- MAHALINGAM S., CANTWELL B. J. & FERZIGER J. 1989 *AIAA Paper 89-0661* Reno, Nevada.
- MARBLE F. E. & BROADWELL J. 1977 *Project Squid Headquarters Tech. Report* TRW.
- MASUTANI S. M. & BOWMAN C. T. 1986 *J. Fluid Mech.* 172, 93-126.
- POINSOT T., TROUVE A., ESPOSITO E. & CANDEL S. 1987 *Turbulent Shear Flows* Toulouse, France.
- POINSOT T. & CANDEL S. M. 1988 *Comb. Sci. Tech.* in press.
- POINSOT T., TROUVE A., VEYNANTE D., CANDEL S. & ESPOSITO E. 1986 *J. Fluid Mech.* 177, 4, 265-292.
- RILEY J. J., METCALFE R. W. & ORSZAG S. A. 1986 *Phys. of Fluids* 29, 406.
- ROCKWELL & SCHACHENMANN 1982 *J. Sound Vib.* 85, 3, 371-382.
- RUTLAND C. & FERZIGER J. 1989 *AIAA Paper 89-0127* Reno, Nevada.
- TANG & ROCKWELL 1983 *J. Fluid Mech.* 126, 187-204.
- YANG V. & CULICK F. E. C. 1986 *Comb. Sci. Tech.* 45, 1-25.

ZIADA & ROCKWELL 1982 *J. Fluid Mech.* **118**, 79-107.

ZIADA & ROCKWELL 1982 *J. Fluid Mech.* **124**, 307-334.

Turbulent transport in the solar nebula

By K. W. THOMPSON

1. Problem Description

It is likely that turbulence played a major role in the evolution of the solar nebula, which is the flattened disk of dust and gas out of which our solar system formed. Relevant turbulent processes include the transport of angular momentum, mass, and heat, which were critically important to the formation of the solar system. This research will break new ground in the modelling of compressible turbulence and its effects on the evolution of the solar nebula. The computational techniques which have been developed should be of interest to researchers studying other astrophysical disk systems (e.g. active galactic nuclei), as well as turbulence modelers outside the astrophysics community.

2. Objectives/Milestones

The work currently being performed system is closely connected with that of Cabot, Hubickyj, and Pollack (hereafter CHP), who have been using the turbulent channel flow code of Kim, Moin, & Moser (1987) to investigate incompressible turbulence in the solar nebula. The turbulence simulation code developed for this project will ultimately replace the central elements of the channel flow code, while incorporating many of the useful analysis tools developed for the latter.

The objectives of this project fall into two categories:

1. To advance the understanding of the role of *compressible* turbulence in the evolution of the solar nebula by carrying out a series of numerical experiments to evaluate the Reynolds stress tensor, turbulent heat transfer rate, turbulent dissipation rate, and turbulent energy spectrum for conditions relevant to the solar nebula;
2. To advance the state of the art in turbulence simulation techniques by exploring new computational methods which are expected to be both efficient and flexible.

The field of solar nebula physics is one of much current interest, as seen, for example, in the contributions to *Protostars and Planets II* (Black & Matthews 1985). The field of turbulence is also one of much current interest.

2.1 Scientific Objectives

The first objective is scientific and largely astrophysical in nature. Turbulent processes are believed to have been important in the evolution of the solar nebula, which was a rarefied disk of gas and dust, out of which the planets, asteroids, and

comets formed. This disk circled the Sun during and shortly after its formation. The nebula is in turn thought to have formed out of the contraction of a much larger and even more diffuse molecular cloud. The nebula's central star, our Sun, also formed out of the molecular cloud matter, and it is the Sun's gravity which held the nebula together and kept it from flying apart. The combination of the Sun's gravitational field, the initial angular momentum of the molecular cloud (retained by the nebular material), and radiative cooling is believed to have confined the solar nebula to a thin disk, rather than a cloud. (The formation and evolution of protostellar disks continue to occur in active star formation regions in our galaxy, and this research is relevant to nebular problems in general, not only to our solar system.)

Anticipated sources of turbulence include thermal convection (driven by temperature gradients), vertical shear in the angular velocity (due to the nonuniform deviations from the central plane orbital motion of the gas with altitude), and the large velocity differential between the rotating disk matter and the infalling (non-Keplerian) molecular cloud material. Turbulent convection is expected to be strongly dependent on the compressibility of the flow; hence, the study of compressible turbulent flow is crucial to this project.

The effects of turbulence on the solar nebula are many. Turbulent dissipation causes a loss of orbital energy and, therefore, an inward flow of mass toward the central star. The inflow of mass must be accompanied by an outflow of specific angular momentum in order to conserve total angular momentum. The inward transport of mass feeds most of the nebular matter to the Sun, while the outward transport of angular momentum causes the nebula to expand. Turbulence will also transport heat, both radially (parallel to the central disk plane) and vertically (in the perpendicular direction). Turbulent dissipation, mentioned above, is expected to be a major (perhaps dominant) source of heat for the nebula. Turbulent dissipation converts kinetic energy to heat, which is then radiated away to space, reducing the total energy of the system and making the nebula more tightly bound to the Sun.

The greatest obstacle to the accurate modeling of the solar nebula is the fact that the length scales on which viscous dissipation takes place (and on which the turbulent kinetic energy is turned into heat) is many orders of magnitude smaller than the size of the disk. Consequently, it is not currently possible to create a single computational model which accurately simulates both the large scale structure and the small scale turbulent dissipative processes. The objective of this project is to simulate numerically the turbulent processes on a small scale and obtain a parameterization of these processes which may be used in other attempts to model the large scale evolution of the nebula. Much of this work is being done by other researchers (CHP), but their efforts must be considered in the developments described below, as the results of their research will be incorporated into this model.

Several issues need to be addressed in order to produce a realistic model for

the solar nebula. The most obvious of these is the Sun's gravity, which forces the gas to follow nearly Keplerian velocity profiles in its rotation about the Sun. Radial shear is, therefore, produced in the flow, as the orbital angular velocity decreases with distance from the Sun.¹

The Keplerian flow velocities are highly supersonic in the rest frame of the central star. A direct simulation of the flow in the star's rest frame is impractical, as the flow velocities dictate unworkably small time steps. A better approach is to work in a coordinate system which is comoving with the average flow in the model volume, so that the velocities are subsonic in the model's coordinate system, and the time steps are more reasonable.

A coordinate transformation based on the work of Rogallo (1981) will be used to represent the radial shear in a form which permits the use of periodic boundary conditions in the radial direction. The Rogallo transformation eliminates the need to devise boundary conditions which properly advect turbulent flow in and out of the radial boundaries.

A second type of shear exists due to the matter falling in from the collapsing molecular cloud onto the disk. The radial and angular velocity components of the infalling material will be quite different from those of the rotating disk. While the vertical velocity component of the infalling matter will be reduced by the accretion shock at the cloud-disk interface, it will remain nonzero, providing a downward directed ram pressure on the disk material. In addition, the radial and angular velocity components of the infalling matter will not be affected by the shock and will create a large velocity shear relative to the disk material. This is an important question, and new techniques may have to be developed to study it. The effects of these factors on nebular turbulence could be important.

A subtler gravitational effect is the vertical variation of gravity within the disk. The disk is very thin compared to its radial dimensions; therefore, a fluid element a distance z above the central disk plane experiences a downward-directed gravitational force (due to the central star) which is proportional to z . This linear variation of gravity is expected to have a significant effect on the convective flow. Convection in the Earth's atmosphere takes place in an altitude range over which the gravitational acceleration is essentially constant. The nebular problem has a variable acceleration with altitude, which may give rise to flow patterns not seen in constant gravity environments and is expected to affect turbulent transport.

Another major issue is the compressibility of the fluid. The computational technique of Kim *et al*, as currently implemented by CHP assumes an incompressible fluid, but the solar nebula is strongly stratified and is, therefore, expected to behave like a compressible gas. Thus it is necessary to use the compressible fluid equations. Most of the work on turbulent flow in the past has

¹ Note: the radial shear by itself is stable and will not directly cause turbulence. Turbulence must be induced by other effects such as viscous heating and vertical shear.

concentrated on incompressible flows.

The channel flow code assumes flow between two parallel plates, for which the fluid velocities go to zero at the plates. The no-slip boundary condition makes sense for flow in a channel but is not valid for flow in the solar nebula. It is desirable to replace these no-slip wall boundary conditions with conditions which are representative of the solar nebula. The nonreflecting boundary conditions of Thompson (1987a) are being used for this purpose. These conditions allow material to flow across the boundaries and allow outward propagating waves to leave the computational domain without generating reflections.

2.2 Improvements to Turbulence Simulation Techniques

The second category of objectives, which may have applications outside of astrophysics (e.g. the aeronautical community), focuses on the improvement of turbulence simulation techniques in general.

The computer code currently in use is very flexible and is able to adjust to a wide variety of boundary conditions and computational techniques. It is designed to be easily modified so that new features may be added and different computational techniques incorporated as needed. For example, the spatial derivative methods can be modified at will (e.g. from finite difference to pseudospectral) by altering only that section of the code which computes these derivatives.

The techniques in use are described in section 3.

2.3 Milestones Passed

The work performed so far has been concerned with analyzing alternative computational methods, developing a suitable computing strategy, and validating the computer simulation. Early design and testing focused on simple linear and nonlinear wave simulations, for which error analysis and convergence testing could be performed easily. The later stages have involved the full set of compressible fluid equations. Successful tests have validated the design of the computer code and are described below. One of these tests has had the added benefit of generating a significant new research project in its own right, as described below.

The major program tests are:

1. Rarefaction wave.
2. Oscillating atmospheric column.
3. Hydrodynamic escape.
4. Unstable shear flow (Kelvin-Helmholtz instability).

2.3.1 Rarefaction Wave

The rarefaction wave is the well known solution to the adiabatic expansion of a uniform gas into a vacuum in the absence of gravity. The exact solution to this problem has been given in many places, (e.g. Landau & Lifshitz 1959,

Thompson 1986). Time dependent numerical simulations of the continuous part of the rarefaction wave were highly accurate and exhibited the proper fourth order convergence with grid refinement.

2.3.2 Oscillating Atmospheric Column

This problem describes a column of atmosphere in a constant gravitational field. The density and pressure drop off exponentially with altitude z , as $e^{-z/h}$, where h is the vertical scale height. This is a one dimensional problem, as the solution does not depend on x or y . The initial state is isothermal and is stable.

Just as in an organ pipe, one can set up standing waves at certain discrete frequencies. I have set up an adiabatic perturbation to excite the lowest frequency mode of the column for problems ranging from 1 to 50 vertical scale heights in extent. In all cases the time dependent solution accurately reproduced the expected oscillatory mode and displayed the correct fourth order convergence. The exponential dependence of the unperturbed state makes this problem an obvious choice for solution by the methods of section 3.1.

2.3.3 Hydrodynamic Escape

This problem is also one dimensional but spherically symmetric. It describes the escape of a planetary atmosphere into space. Gravity obeys the inverse square law, and the flow velocity goes smoothly from highly subsonic near the planet's surface to highly supersonic at large distances. Steady state solutions have been known analytically for some time (Bondi 1952). It is an interesting fact that the same equations describe the solar wind and the accretion of gas onto a protostar embedded in a spherically symmetric cloud.

Although the analytic solution is known, this problem presents special problems for numerical techniques (Zahnle 1988). I have found it to be a challenging problem (and a useful one for uncovering some subtle boundary condition problems) but can now produce stable and accurate solutions. The problem contains enormous pressure and density gradients near the lower boundary, and the density and pressure vary by several orders of magnitude in the model volume. This problem is rendered tractable by the logarithmic techniques described in section 3.1. Previous attempts to solve this problem numerically with more standard methods have failed.

The more general problem of hydrodynamic escape of planetary atmospheres which are affected by thermal conductivity and solar heating is of considerable interest to researchers in the field. The successful solution of the more basic problem will serve as a starting point for further research on this subject by Zahnle, my co-investigators, and myself.

2.3.4 Unstable Shear Flow

This is a well known problem in the atmospheric sciences, and one which is two dimensional in nature. We have an initially isothermal atmosphere whose

density and pressure vary exponentially with altitude z as $e^{-z/h}$ (rectangular coordinates). The atmosphere contains a shear flow with velocity components $(U(z), 0, 0)$, where $U(z) = U_0 \tanh(z/d)$, $d < h$, and U_0 is subsonic. We perturb the flow field by adding small velocity perturbations $u(x, z)$ and $w(x, z)$ so that the perturbed velocity is $(U + u, 0, w)$. Perturbation theory (Chandrasekhar 1961) shows that the stability of the flow is determined by the *Richardson number* $Ri = gd^2/hU_0^2$. A Kelvin-Helmholtz instability arises if $Ri < 1/4$, while the flow is stable if $Ri > 1/4$.

Calculations performed with Richardson numbers of 0.05 and 0.15 do indeed give rise to unstable flow. These calculations show that the initially small perturbations grow and create a vortex. Similar calculations with Richardson numbers of 0.35 and 1.25 are stable and do not lead to vortex formation. These results are consistent with the predictions of linear stability analysis.

3. Technical Approach

The equations to be solved are the compressible Navier Stokes equations. They describe the time evolution of a compressible fluid in three dimensions and incorporate the effects of a variable gravitational field, radial shear, molecular viscosity, thermal conductivity, and internal heat sources. The solution process is made challenging by the large variation in density and pressure which occurs in this problem. A new technique has been developed to handle the range problem as described below.

The purpose of this calculation is to study relatively small scale turbulence in order to characterize the effects of turbulence on the overall flow without resorting to *ad hoc* turbulent viscosity approximations. Therefore, the actual volume to be simulated consists of a small "box" of nebular material in the disk of relatively small radial and angular extent as seen from the Sun.² The box includes one to several scale heights of pressure variation in the direction perpendicular to the disk midplane. Periodic boundary conditions are used at the boundaries facing "sideways" into the disk material (i.e. the ϕ boundaries). The r boundaries make use of Rogallo's method (Rogallo 1981) to specify periodic boundary conditions. The θ (vertical) boundaries require non-trivial boundary conditions and are currently handled by the nonreflecting conditions described by Thompson (1987a).

3.1 The Range Problem

The density and pressure in the nebula fall off very rapidly with altitude above the nebula midplane, roughly as $e^{-(z/h)^2}$, where h is a scale height.³ Thus the density and pressure may vary by orders of magnitude throughout the model volume, which poses a difficult challenge to conventional numerical techniques.

² The spherical coordinate system is assumed for this discussion.

³ The unusually rapid falloff is due to the variable gravity, which increases with altitude.

I have developed a technique to deal with scalar fields which vary over such a large range by using the logarithms of density and pressure instead of the basic quantities themselves. For example, the one dimensional continuity equation,

$$\frac{\partial \rho}{\partial t} + \frac{\partial}{\partial x}(\rho u) = 0,$$

is replaced by

$$\frac{\partial \ln \rho}{\partial t} + u \frac{\partial \ln \rho}{\partial x} + \frac{\partial u}{\partial x} = 0,$$

and similarly for the energy equation. Thus an exponential dependence of ρ on x is reduced to a polynomial dependence of $\ln \rho$ on x , which the numerical scheme can cope with more readily. All derivatives of density, pressure, and thermal energy may be replaced by their logarithmic forms as above, leading to a more tractable system. An added benefit is that the density and pressure cannot become negative with this approach.

3.1.1 The Numerical Techniques

The current code uses standard fourth order finite difference formulas to evaluate spatial derivatives in all directions (see, for example, Thompson 1987b).⁴

Time integration is handled by the usual fourth order explicit Runge-Kutta method, which is simple to implement and has excellent stability properties. This combination of spatial derivative and time integration methods provides global fourth order convergence. The fourth order convergence rate has been verified repeatedly on a large number of test runs and implies that this code requires significantly fewer grid points than a second order code to achieve a given level of accuracy.

The choice of an explicit method over an implicit method stems from the need to resolve the smallest features present in the flow. At the smallest length scales, viscosity dominates the evolution of the flow. Since we need to simulate the dissipation of kinetic energy to heat accurately at these scales, the grid spacing and time steps necessary are set by the properties of the flow and are the same whether explicit or implicit methods are used. The optimal grid spacing and time step are those for which the propagation and viscous Courant numbers are equal. Consequently, the simpler (and faster) explicit approach has been selected.

⁴ Compact difference formulas of the compact (Padé) type (Rubin & Koshla 1977) have been evaluated but have not been found to offer significant improvements over the standard fourth order formulas.

REFERENCES

- BLACK, D.C. & MATTHEWS, M.S. (EDITORS) 1985 *Protostars and Planets II*, University of Arizona Press, Tucson, Arizona.
- BONDI, H. 1952 On Spherically Symmetrical Accretion. *Monthly Notices of the Royal Astronomical Society*, **112**, No. 2, 195.
- CHANDRASEKHAR, S. 1961 *Hydrodynamic and Hydromagnetic Stability*, Oxford University Press (reprinted by Dover Publications, New York NY).
- KIM, J., MOIN, P. & MOSER, R. 1987 Turbulence statistics in fully developed channel flow at low Reynolds number. *Journal of Fluid Mechanics*, **177**, 133.
- LANDAU, L.D. & LIFSHITZ, E.M. 1959 *Fluid Mechanics*, Pergamon Press, Elmsford NY.
- ROGALLO, R. 1981 *Numerical Experiments in Homogeneous Turbulence*, NASA Technical Memorandum 81315.
- RUBIN, S.G. & KOSHLA, P.K. 1977 Polynomial Interpolation Methods for Viscous Flow Calculations. *Journal of Computational Physics*, **24**, 217.
- THOMPSON, K.W. 1986 The Special Relativistic Shock Tube. *Journal of Fluid Mechanics*, **171**, 365.
- THOMPSON, K.W. 1987a Time Dependent Boundary Conditions for Hyperbolic Systems. *Journal of Computational Physics*, **68**, 1.
- THOMPSON, K.W. 1987b *Lecture Series in Computational Fluid Dynamics*, NASA Technical Memorandum 10010.
- ZAHNLE, K. 1988 Private communication.

Transition to turbulence in laminar hypersonic flow

By J. VAN DER VEGT

1. Introduction

This report gives a short discussion of the progress in a recently started project aimed at the prediction of transition to turbulence in hypersonic flow. The prediction of transition to turbulence is a very important issue in the design of space vessels. Two space vehicles currently under investigation, namely the aeroassisted transfer vehicle (AOTV) and the trans-atmospheric vehicle (TAV), suffer from strong aerodynamic heating. This heating is strongly influenced by the boundary layer structure. These aerospace vehicles fly in the upper atmospheric layer at a Mach number between 10 and 30 at very low atmospheric pressures. At very high altitudes the flow is laminar, but when the space vessel returns to a lower orbit, the flow becomes turbulent and the heating is dramatically increased.

The prediction of this transition process is commonly done by means of experiments. The experimental facilities available nowadays cannot model the hypersonic flow field accurately enough by limitations in Mach and Reynolds number. These facilities also have a large free stream disturbance level which makes it very difficult to investigate transition accurately. An alternative approach is to study transition by theoretical means. Up to now numerical studies of hypersonic flow only discussed steady laminar or turbulent flow. The project discussed in this report tries to extend this theoretical approach to the study of transition in hypersonic flow by means of direct numerical simulations and additional theoretical investigations to explain the mechanisms leading to transition. This report gives a brief outline of how we plan to carry out this research.

2. Important Physical Phenomena

There are several important new physical phenomena in hypersonic flow which are not important in supersonic flow. The flow exhibits extreme heating, especially in the stagnation point region. This causes non-equilibrium chemical reactions, dissociation, and ionization, which have to be taken into account. Also, the effect of radiation cannot be neglected. The gas is rather dilute, so the limits of the continuum approach are reached, but with slight modifications, the Navier-Stokes equations still can be used.

3. Transition to Turbulence

There are several techniques for studying the transition phenomena. The

most widely used technique is linear stability theory, using the normal mode approach in both space and time coordinates. This technique is, however, not very reliable for the prediction of the position and behavior of the actual transition phenomena and, in many cases, additional empirical information is necessary for accurate prediction. This empirical information is very scarce in hypersonic flow so accurate numerical solutions are necessary.

The main reason for the failure of linear stability theory can be attributed to the fact that finite amplitude disturbances, requiring non-linear stability theory, cannot be neglected. This is demonstrated by experiments on a cone conducted by Stetson (1988). A more general valid theory describing the transition process is given by Ruelle and Takens (1971). It assumes that the change from a laminar to a turbulent state takes place by means of a finite number of bifurcations. Studying these bifurcations by theoretical means and direct numerical simulations can give more detailed information about the transition process. This method allows large disturbances and gives more freedom than a linear theory.

Direct numerical simulations of hypersonic flow accurate enough to predict transition will be very time consuming. An additional problem with direct numerical simulations is caused by the fact that there are so many independent parameters that it is hardly possible to investigate all relevant situations by this method. It is, therefore, necessary to study the transition problem by means of a coupled theoretical and numerical approach. The aim of this study is to obtain detailed information on the actual mechanisms leading to transition in hypersonic flows and to obtain information useful for engineers.

4. Achievements

The project started in September 1988, so there are only limited results. During this period, the literature and basic phenomena in hypersonic flow were studied. The results of this study are to be used to make a project proposal for the study of hypersonic transition.

5. Proposal for the Calculation of Transition to Turbulence in Laminar Hypersonic Flow

General: The main purpose of this research is to get insight in the phenomena which lead to transition from laminar to turbulent hypersonic wall bounded flows. In order to accomplish this goal, two main tools will have to be developed:

- An accurate code for the direct numerical simulation of time dependent hypersonic flows.
- A mathematical model for investigating the stability and bifurcation phenomena leading to transition in hypersonic flow.

Due to the facts that we have to start from scratch and that there are large uncertainties about the method, it is very important to follow a stepwise procedure. This approach is summarized below:

-A Solution of Two-Dimensional Navier-Stokes Equations for a Flat Plate

The first step will be to make a computer model for the viscous supersonic two-dimensional flow on a flat plate at low Mach number ($M \leq 3$) using a finite difference method.

It is assumed that there are no shocks in the flow field. The numerical model, however, must solve the Navier-Stokes equations in conservation form together with the ideal gas equation of state. The use of a conservative formulation provides the opportunity of shock capturing in a later stage of the project. The numerical method has to be at least partially implicit in time in order to be able to add a chemistry model for the reacting gas flow while avoiding serious restrictions on the time step due to stiffness. Possible numerical methods are the implicit Mc Cormack and Beam and Warming schemes which are second order accurate in time and space (Anderson, Tannehill and Pletcher 1984).

Due to the geometric simplicity a new program will be written instead of using an existing general purpose computer program which would need modifications to be efficient for a flat plate.

- The purpose of this part is:

1. Obtain experience with these type of calculations. Although existing numerical methods will be used, it is important to test these methods on a relatively simple problem and especially to investigate the effect of numerical parameters like time step, number of grid points, stability, and numerical diffusion.
2. Test the accuracy of the numerical algorithm by comparing the growth rate of an Orr-Sommerfeld wave with the prediction obtained with linear stability theory by Mack (1984).
3. The direct numerical simulations will be used to compute the evolution of finite amplitude disturbances and study the effect of wall temperature.

-B Three-Dimensional Direct Numerical Simulations of the Flow on a Flat Plate

There is a severe restriction on using a two-dimensional model for direct numerical simulations because, at high Mach numbers, oblique waves become more

unstable than two-dimensional waves. In order to investigate this phenomenon, the numerical model will be extended to three-dimensional flow on a flat plate.

- This part of the research should give a more accurate representation of the flow field and offer the opportunity to investigate three-dimensional effects. It can also be used for a thorough investigation of the accuracy of the e^N method widely used in engineering applications.

-C The Effects of Chemistry

The effects of chemistry on transition are not very clear. In order to investigate these phenomena, both with respect to their effects on the numerical algorithm and on the flow field, they will be added to the two-dimensional numerical model. Initially the chemical model for non-equilibrium chemistry of Candler (1988) will be used. This model is a seven species chemical model for N_2 , O_2 , NO , N , O , NO^+ and e^- . The effects of ionization will be neglected in this stage, so the rate equations for NO^+ and e^- will not be used.

- This part of the research should give information about the effects of the chemical reactions on transition phenomena and velocity profiles.

-D Further Study of Transition

In the investigation of the phenomena leading to transition, linear stability theory is not always accurate enough. The most important reason is the fact that linear stability theory gives no information about finite amplitude disturbances. A non-linear stability study will be conducted to investigate these effects.

- This part of the study would give more detailed information about the actual phenomena leading to transition and they can be further investigated with the numerical model.

-E The Effects of Internal Energy and Ionization

At higher temperatures, energy associated with internal degrees of freedom and ionization effects become important. These effects are incorporated by adding an additional energy equation for the vibrational energy and an equation for the electron translational energy. At this stage, it is supposed that there are three relevant temperatures, viz. a translational temperature, a vibrational temperature and electron temperature.

- This part of the research should give information about the internal energy and ionization effects on transition.

-F Direct Numerical Simulation of the Flow Field around a Cone

The procedure discussed for the flat plate can also be used to investigate the flow field around a cone. The calculation of the flow field around a cone is more difficult, so it is advantageous to start this research when more experience is obtained with the flat plate. An interesting phenomenon in this flow is the interaction between the boundary layer and a shock. The shock has a strong effect on the flow field. However, it requires a high resolution which is probably difficult to obtain in three-dimensional flows. The study will, therefore, start with an axisymmetric model.

- This part of the research can provide more information about the effects of interaction between shock and boundary layer on transition.

REFERENCES

- STETSON, K. F. 1988 On Nonlinear Aspects of Hypersonic Boundary-Layer Stability. *AIAA Journal*. **26**, 883-885, 1988.
- ANDERSON, D. A., TANNEHILL, J. C., & PLETCHER, R. H. 1984 *Computational Fluid Mechanics and Heat Transfer* Hemisphere Publishing Corporation.
- CANDLER, G. V. 1988 The Computation of Weakly Ionised Hypersonic Flows in Thermo-Chemical Non-Equilibrium PhD Thesis, Stanford University.
- MACK L. M. 1984 Boundary-Layer Linear Stability Theory, Von Karman Institute Belgium.
- RUELLE, D. & TAKENS F. 1971 On the Nature of Turbulence. *Comm. Math. Physics*. **20**, 167, also 1971 **23** 343, 1971.

Direct numerical simulations of turbulent convection with a variable gravity and Keplerian rotation

By W. CABOT

1. Motivation

Thermal convection has been proposed as a possible mechanism for generation and maintenance of turbulence in the inner accretion disk regime of the primordial solar nebula. Resulting Reynolds stresses would produce a torque on the disk, causing "viscous" spreading and the eventual dispersal of the gas component of the disk; this process was coeval with and coupled to the formation of the planetesimals and, ultimately, planets. Turbulent convection under solar nebula conditions has been described to date by *ad hoc* and mostly untested models of thermal convection and turbulence. The models of Lin & Papaloizou (1980) and Cabot *et al* (1987), in particular, give vastly different results in terms of the vertical distribution and intensity of turbulence, the efficiency of convection, and structural stability properties. There are yet few, if any, conclusive astronomical observations of solar nebula analogues, nor does indirect evidence from planetary compositions provide clear constraints on these models. It is, therefore, of fundamental interest to design experiments with the basic physical features of the solar nebula in order to constrain old and new models. Although solar nebula conditions cannot be reproduced in the laboratory, numerical simulations of hydrodynamic flows, which have been very successful in describing aerodynamic flows, can be suitably modified to provide "experimental" data for solar nebula modelling.

2. Objectives

The goals of this project are (1) to modify an extant, "proven" hydrodynamics code with the most important features of the solar nebula and other thin accretion disks: buoyancy terms to generate convection, internal heating representing the release of gravitational potential energy, a variable gravity linearly proportional to the distance from the vertical midplane due to centrifugal balance, rapid rotation with axis aligned with gravity, and Keplerian rotational shear; (2) to determine the effect that these features have on the turbulent convection by introducing them individually and to determine the cumulative nature of the turbulent convection for accretion disk conditions; and (3) to model the convection (*viz.*, the convective heat flux) and the turbulence (*viz.*, turbulence intensities, heat dissipation, and Reynolds stresses). In this manner, prior solar nebula models can be tested and their deficiencies rectified.

3. Work to Date

Uniform rotation. The code for direct numerical simulations of a incompressible flow in a semi-infinite channel (Kim, Moin & Moser, 1987) was modified to include buoyancy in the Navier-Stokes equation in the Boussinesq approximation, the variable gravity, and uniform rotation. Both no-slip and no-stress boundary conditions on the vertical walls were implemented (the latter being more realistic for the solar nebula). Sequences of simulations with varying rotation rates were performed, from no rotation to rates approaching the limit of stability. A linear analysis was performed to determine theoretical critical rotation rates for marginal stability. It was found that the convective fluxes in the numerical simulations become negligible between the marginal limits of stationary and oscillatory convection, and there may also be finite amplitude effects occurring in this rotation regime.

The turbulence intensities and efficiency of the convection were found to be virtually undiminished in the midchannel region where buoyancy vanishes; this region posed a major uncertainty in prior solar nebula modelling, and this result not only clarifies the nature of the turbulence there but allows some simplification in modelling. An extension of the standard stellar mixing length model for convective heat fluxes and speeds was developed to include viscosity and rotation and was found to agree qualitatively with the rotational dependence of the simulation results, although convective fluxes and speeds in the model were found to be a factor of 3 too low for standard values of coefficients. Canuto & Goldman's (1985) turbulence model, used in Cabot *et al*'s (1987) solar nebula model, also gave a qualitatively similar dependence of convective heat flux and speed on rotation, but gave convective fluxes that were *30 times too low*.

The vertical distribution of convective buoyancy production of turbulence kinetic energy has a bimodal shape with peaks on either side of midchannel and vanishing at midchannel. For low rotation rates, nonlinear diffusion (primarily by convective transport) redistributes the turbulence so that it is dissipated with a flat interior profile. For high rotation rates, the overall diffusion is suppressed (with diffusion by pressure fluctuations now dominating) such that dissipation near midchannel is depressed. This result further supports the assumption made by Cabot *et al* (1987) that heat dissipation is evenly distributed throughout the convective region, than it does the model by Lin & Papaloizou (1980), in which the turbulence intensities and dissipation is sharply peaked at the midplane. Since the heat dissipation is ultimately the heat source in the solar nebula, it is important to assess the sensitivity of the heat dissipation distribution to that of the internal heat source. Tests with centrally concentrated internal heating show that the interior heat dissipation profile is very insensitive to that of the heat source, which is again consistent with the assumption that the dissipation will have a relatively flat interior distribution.

Rotational shear. Linear rotational shear is treated in the numerical integration by working in a cosheared reference frame, in which the governing equations remain horizontally homogeneous, and implementing Rogallo's (1981) remeshing transformation in the homogeneous horizontal directions, which allows one to circumvent the tendency of the numerical grid to become overly distorted as it follows the sheared flow. The remeshing transformation was implemented in the channel code and has been extensively tested. The tendency of the streamwise length scales to become elongated and the spanwise length scales (in the direction of the shear) to become compressed requires balancing horizontal box and mesh sizes in the simulations in order to optimize the numerical resolution, and runs are currently under way in order to determine the optimal numerical domain(s). Several simulations were carried out with less than optimal but acceptable resolution, which have provided the preliminary results subsequently quoted.

Linear stability analysis predicts that the rotation profile is centrifugally stable if the specific angular momentum gradient increases with distance from the rotation axis ($S > -2\Omega$, where S is the shear rate and Ω the rotation rate). This limit was tested and verified with the numerical code with no buoyancy forces in effect. This indicates that the rotational shear flow for Keplerian rotation ($S = -3\Omega/2$) is centrifugally stable and, by itself, cannot maintain the turbulence in accretion disks. Another verification of this proposition was found by allowing a convecting, rotationally sheared flow simulation with well developed Reynolds stresses due to the shear to decay when the internal heating was extinguished; both the convective and shear production rates decayed to zero, indicating that it is convection alone that drives the turbulence in this flow and indirectly maintains Reynolds stresses by the "catalytic" effect of the rotational shear.

Preliminary results for Keplerian rotation at a moderate rotation rate with both no-slip and no-stress (coshearing) vertical walls show well developed Reynolds stresses in the horizontal components ($-\overline{uw}$). The corresponding shear correlation coefficient was found to be 0.21 for no-stress walls and 0.23 for no-slip walls, compared to 0.45 for homogenous, unidirectional, plane shear flows (Townsend, 1956); these values were very uniform across the channel, even at the walls. The shear production rate of kinetic energy was about 16% of the convective production rate. Simulations at different rotation rates are needed to determine the robustness of these results. For uniform rotation with the same inertial frequency, the rms vertical velocity (v_{rms}) was found to exceed the equal streamwise (u_{rms}) and spanwise (w_{rms}) components by about 1.4, because it is the component directly receiving the production by convective buoyancy. For the Keplerian rotational shear case, $v_{rms} \approx 1.3 w_{rms}$ and $w_{rms} \approx 1.4 u_{rms}$, compared to the result for unidirectional, plane shear flow of $u_{rms} > v_{rms} > w_{rms}$. Because convective buoyancy is driving the turbulence in the numerical simulation, one expects v_{rms} to still be the largest. The discrepancy in the

horizontal components may be due to rotation: The production rate in the streamwise component is $-(2\Omega + S)\overline{uw} = -\Omega/2\overline{uw} < 0$, rather than $-S\overline{uw} > 0$ without rotation, and the spanwise production rate is $2\Omega\overline{uw} > 0$.

4. Future Work

In upcoming work, numerical simulations using sequences of rotation rates with Keplerian shear will be constructed. The results will be used to test the robustness of the value of the shear correlation coefficient and the ratio of shear to convective production, or to suggest ways to model whatever variations arise. The stability behavior of the rotationally sheared flow at very rapid rotation rates will be compared with uniform rotation results to determine any effects of the shear; also the effect of shear on the modelling of convective fluxes and speeds will be examined. The interior distribution of kinetic energy dissipation with both convective and shear production will be examined for different rotation rates; modelling for the dissipation and the Reynolds stress will be attempted. Simulations with different Rayleigh and Prandtl numbers will be performed in order to assess their effects on the preceding key quantities with the viscosity-independent product of Rayleigh number and Prandtl number held close to solar nebula model values ($\sim 10^4$ to 10^5); lower Prandtl number simulations will allow higher, more realistic rotation rates to be accessed. At this stage, much more physical and realistic models and parametrizations of turbulent convection in thin accretion disk environments, such as the solar nebula, should be attainable than have been available heretofore.

In the realm of the more distant future are a number of modifications that would make the numerical simulations more realistic. The problem of unrealistic, impermeable vertical boundaries and the imposed vertical scale of the convective region can possibly be relaxed by introducing compressibility to the code, at least in the form of a variable vertical density. For coverage of many density scale heights, the vertical boundary region would be buffered by a convective stable region and the convective motions would select their natural vertical scale; however, implementation of this change will require extensive modifications of vertical integration scheme in the present code, probably requiring finite differencing rather than the present Chebyshev polynomial expansion. Since the dissipation of kinetic energy should properly be equated with the internal heat source, ways to make a self-consistent "bootstrap" will be explored; this will provide a self-consistent way to specify the energy source, and will indicate if the coupling between energy source and turbulence leads to any unanticipated behavior.

This work is being carried out in collaboration with the Space Science division at NASA/Ames (J.Pollack and P.Cassen) and with NASA/GISS in New York (O.Hubickyj and V.Canuto).

REFERENCES

- CABOT, W., CANUTO, V. M., HUBICKYJ, O., & POLLACK, J.B. 1987 The role of turbulent convection in the primitive solar nebula. *Icarus*. **69**, 387–422, 423–457.
- CANUTO, V. M. & GOLDMAN, I., 1985 Analytical model for large scale turbulence. *Phys. Rev. Lett.* **54**, 430–433.
- KIM, J., MOIN, P., & MOSER, R. 1987 Turbulence statistics in fully developed channel flow at low Reynolds number. *J. Fluid Mech.* **177**, 133–166.
- LIN, D. N. C. & PAPALOIZOU, J. 1980 On the structure and evolution of the primordial solar nebula. *Mon. Not. R. Astron. Soc.* **191**, 37–48.
- ROGALLO, R. S. 1981 Numerical experiments in homogeneous turbulence. *NASA Tech. Mem.* 81315.
- TOWNSEND, A. A. 1956 *The Structure of Turbulent Shear Flow*, Cambridge University Press.

Experimental investigation of flow over a backward facing step—progress report

By L. W. B. BROWNE¹

Introduction

This report is a brief statement of the work contributed by the author to the backward-facing step experimental facility located in Test Cell No. 3 in the FML Building, N-260, at the NASA-Ames Research Center, during his sojourn with the Center of Turbulence Research — 3rd February to 28th August 1988. The work was carried out in close cooperation with Dr. Srba Jović, but since this is not a formal report of the Center of NASA-Ames, it has only a single author.

1. Wind Tunnel

Figure 1 shows the sizes and arrangement of the wind tunnel used for these experiments.

The sizes shown are for the final arrangement of the tunnel. They give an area contraction ratio of 9.4, a tunnel aspect ratio (width/height) of 2.17 and a step aspect ratio (tunnel width/step height) of 11.0.

In order to use temperature as a passive marker of the flow, it was considered desirable to have the floor of the tunnel heated to a uniform temperature of about 10°C above the free-stream temperature. This was accomplished by placing 6.3mm thick aluminium plates, with heaters, on the tunnel floor. These rest on spacers placed on the original plexi-glass floor and occupy the 1690mm and 2310mm lengths shown in Figure 1. The aluminium sheets have thin-foil heaters glued to their underside — the heaters being arranged to cover the whole surface of the aluminium. Four heating zones were provided, the voltage to each zone being controlled manually using a variac.

Approximately 40v A.C. has been found to give the required 10°C temperature difference when the free stream velocity is 10.0m/s. The plate temperatures are monitored using 13 thermocouples located on the center-line of the plate in small holes drilled to a depth of 5mm. A temperature distribution with a variation of less than $\pm 0.2^\circ\text{C}$ over the whole plate can be achieved.

To provide a smooth entrance from the contraction section to the aluminium surface, the contraction section was raised until the aluminium surface and the contraction surface coincided. The resulting gap at the top of the tunnel was filled with a free-formed aluminium sheet held in place with duct tape.

1 Permanent Address: University of Newcastle

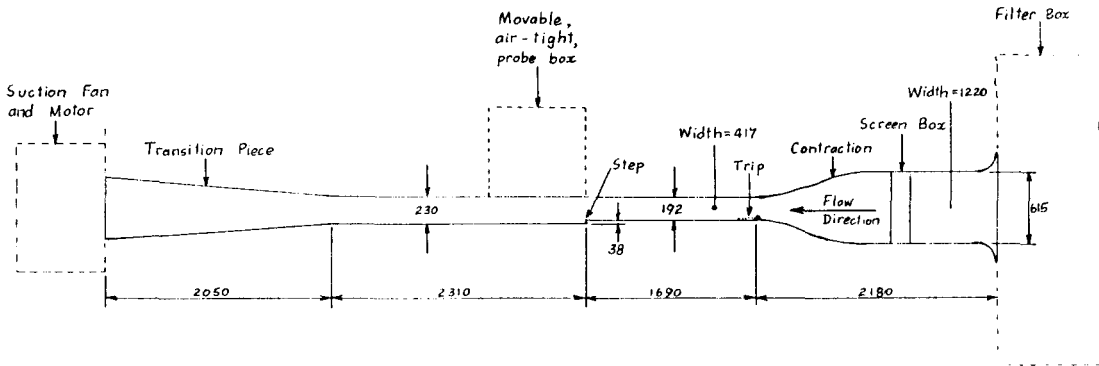


FIGURE 1. Layout and Sizes of Wind Tunnel

The flow was tripped, at the start of the aluminium plate, using a 1.6mm diameter rod followed by a 110mm width of 40 grit emery paper.

To provide an approximate zero pressure gradient flow, the sides of the tunnel were angled slightly outwards.

2. Air Flow

After the difficulties associated with trying to use the large (240,000 c.f.m.) FML compressor to provide a suction flow through a sonic nozzle, it was decided to install a standard suction fan system.

A general purpose fan, manufactured by the New York Blower Company, was purchased. This has a 460mm diameter fan wheel with airfoil-shaped blades capable of running at 2100 rpm. At a speed of about 800 rpm the required tunnel velocity of 10.0 m/s was achieved. As discussed later, this velocity provides an R_θ for the flow approaching the step of 1680. The fan is driven by an "Adjusto-Spede" eddy current clutch unit of the Eaton Corp. The motor (2 hp) runs at a constant 1130 rpm while a controlled current supply to the clutch provides variable speed at the output shaft. A model 3000 controller from the same company controlled the current.

Only 1/2 hp is required for the fan under our operating conditions, but the larger unit will allow other operating conditions to be considered. The single-turn potentiometer of the controller was replaced with a 10-turn unit with counter and was located adjacent to the experiment control area. This provides excellent speed control — the free stream velocity can be held steady, within $\pm 0.2\%$, over typically several hours of operation.

A transition piece between the end of the tunnel and the inlet to the fan was built (see Figure 1).

3. Cold-Wire Anemometers

Constant-current anemometers are commonly used with fine wires (typically $0.63\mu\text{m}$ diameter) to measure temperature fluctuations in turbulent flows. Ian

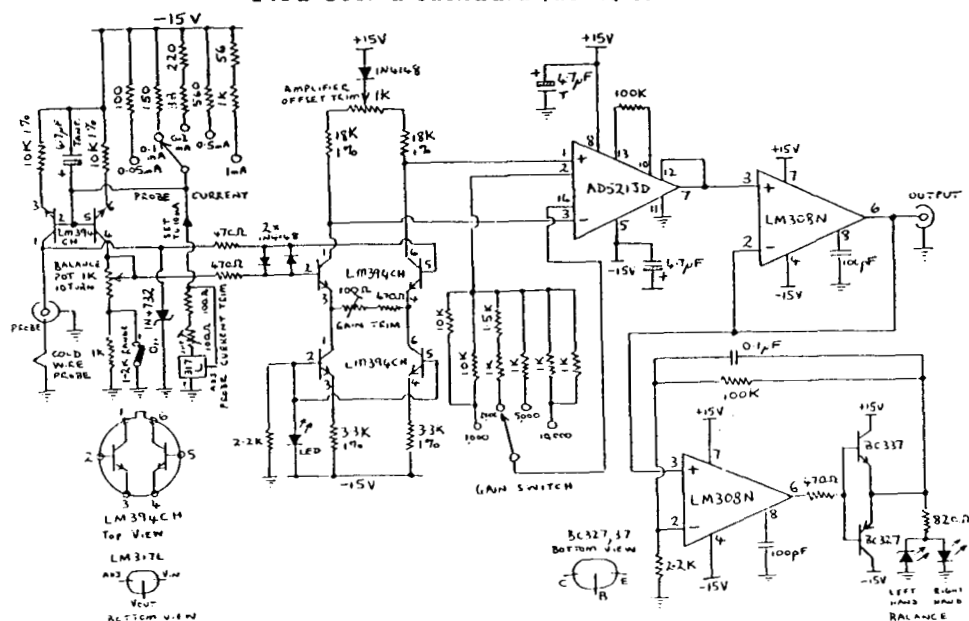


FIGURE 2. Circuit diagram of constant-current anemometer. (Designed by I. Miller — University of Newcastle, Australia)

Miller of the Dept. of Mechanical Engineering at the University of Newcastle has evolved, over the years, an excellent design for such units — See Figure 2.

Twelve circuit boards, one complete unit (to use as a guide), circuit diagrams, board layouts and instructions were supplied from Newcastle by Ian Miller and subsequently twelve constant-current anemometers were built at NASA-Ames. Some time was spent correcting problems (faulty components) but subsequent trials and use have shown the units to be operating very satisfactorily.

4. Hot-Wire Anemometers

Constant-temperature anemometers have also been developed by Ian Miller at the University of Newcastle — see Figure 3.

The signal to noise level of these units is as good as the best commercial units and their high frequency response ($\approx 25kHz$) is quite adequate, although not as high as can be achieved with the commercial units. Three complete units, five circuit boards, circuit diagrams, etc. were sent from Newcastle by Ian Miller. The three units are working very well, but due to parts supply problem, the other five units have not been completed. It may take another month to finish the five units. When these have been tested satisfactorily, the original three units will be returned to Newcastle.

5. Cold-Wire Rakes

Rakes of cold wires often provide the best means for the detection of coherent structures in a turbulent flow in which temperature has been added as a passive

Wollaston wire and attached directly to the prongs. Their L/d of 130 is a little small, but from other work, were considered to be satisfactory.

To allow for more accurate measurements in the high turbulence intensity regions of the flow, the included angle between the wires was made 140° rather than the usual 90° . The cold wire is $0.63\mu\text{m}$ Pt - 10% Rh etched from a 1mm length of Wollaston wire soldered to prongs that can be moved forward and away from the x -wires to provide for easiest replacement of the wires. In its operating position, the cold wire is located in front and at right angles to the hot wires and as close as possible to them. The etched length of 0.5mm does not interfere with the flow over the hot wires.

8. Software

A number of programs were developed. These relate to instrument calibration, data taking, and data processing.

9. Results

9.1. Mean Free-Stream Velocities

Using a Pitot-tube it was found that the free-stream velocity, of 10m/s, outside the boundary layers on all surfaces of the tunnel, was uniform at any x position with $\pm 0.2\%$. There was a slightly favorable pressure gradient from the trip to the step, the center-line-mean velocity increasing by 0.3m/s over that distance (1690mm). A reference point for measuring the free stream velocity was established at 300mm upstream of the step.

9.2. Spanwise Velocity Variations in Boundary Layer Upstream of Step

The spanwise velocity variations in the floor boundary layer were typical of wind tunnel flows. Figure 4 shows the velocity variations, obtained with a Pitot tube, at $x = -225\text{mm}$ (i.e. 225mm upstream from the step), at two distances from the wall.

The same patterns exist right through the boundary layer at any x position between the trip and the step (see Figure 5).

Note that the peaks and valleys of the variations occur consistently at the same z locations at all x positions and at any position in the boundary layer. It is also interesting to note that the same velocity variation patterns exist in the boundary layer before it arrives at the trip (see Figure 6).

Swearingen and Blackwelder (1987) found similar patterns of spanwise variations of the mean velocity in a wind tunnel boundary layer.

Bradshaw (1965) and Mehta and Hoffmann (1987) carried out investigations of this phenomena. The results they obtained changed whenever the last screen in the screen box was changed (or even when the last screen was vacuum cleaned), but the spanwise variations were always present. The best results obtained by

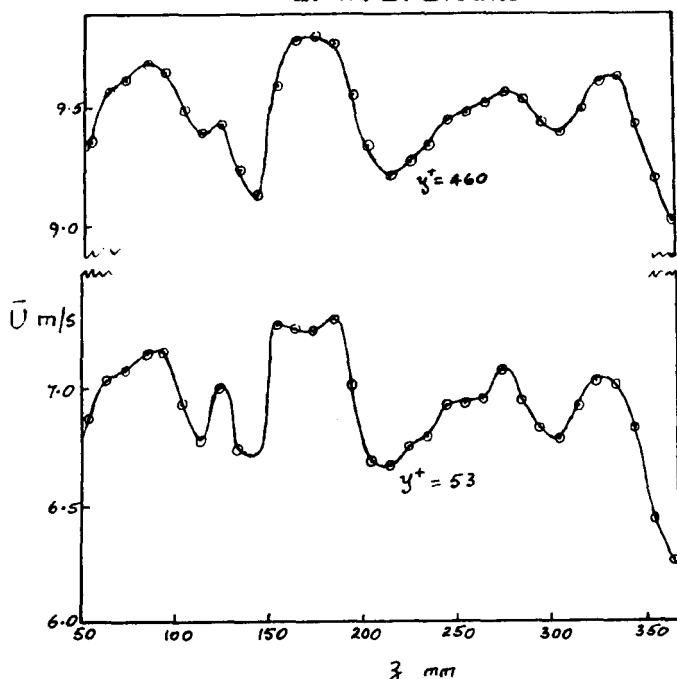


FIGURE 4. Spanwise distribution of mean velocities at $x = -225\text{mm}$ at two positions in the boundary layer.

Mehta and Hoffmann (1987) was a $\pm 5\%$ peak to peak variation in the spanwise values of C_f , although a $\pm 17\%$ variation with earliest screens had been measured. We obtained a $\pm 7\%$ variation in the spanwise values of C_f at $x/H \approx -6$ (H is the step height), see Figure 7, and considered this to be satisfactory.

It was decided to carry out all future measurements at a z of 252mm. This point was still near the centre-line position ($z = 208\text{mm}$) and lay on the C_f curve at a point where the values were not changing too rapidly.

Note that (Mehta, verbal communication), since the spanwise variations are due to the final screen, (essentially there is some agglomeration of the streamwise vortices formed by the screen) a boundary layer developed on a plate placed centrally in the wind tunnel still has similar spanwise variations in the velocity and C_f values.

Recently, at a Berlin Conference (Second European Turbulence Conference, Aug. 30-Sept. 2, 1988, Technische Universität Berlin) Dengel and Fernholz (1988) reported that they had reduced C_f variations, caused by screens, from $\pm 15\%$ to 1% by using special "well behaved and carefully selected screens." Their final screen was produced by stamping rectangular holes in a piece of sheet metal — the sheet being about 0.5mm thick and the holes having a size of about 8mm \times 5mm with their centre-lines being on a grid of about 11mm \times 8mm. The solidity was thus about 0.4 - close to the norm for wind tunnel design.

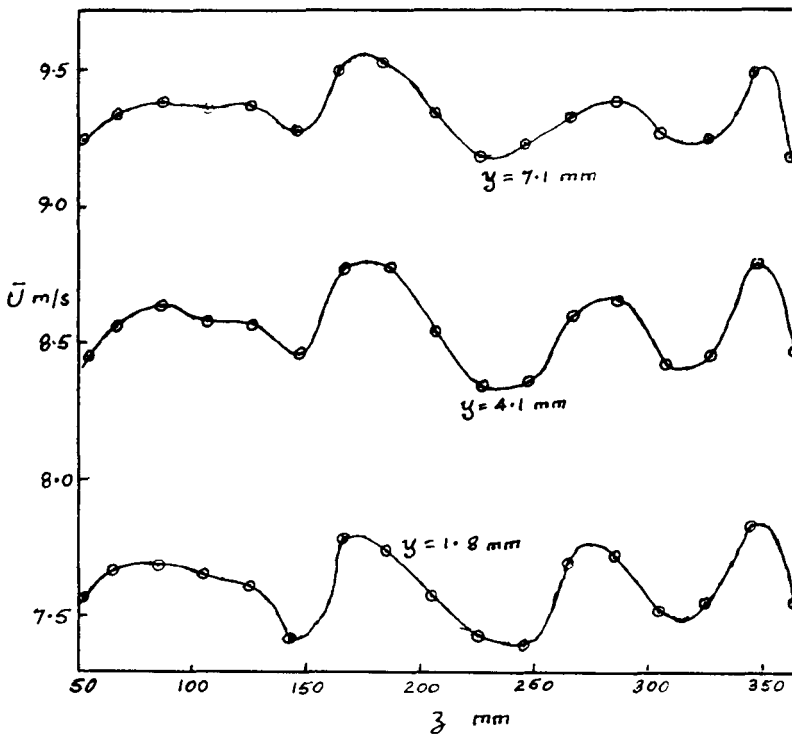


FIGURE 5. Spanwise distribution of mean velocities 355mm downstream of the trip at three positions in the boundary layer.

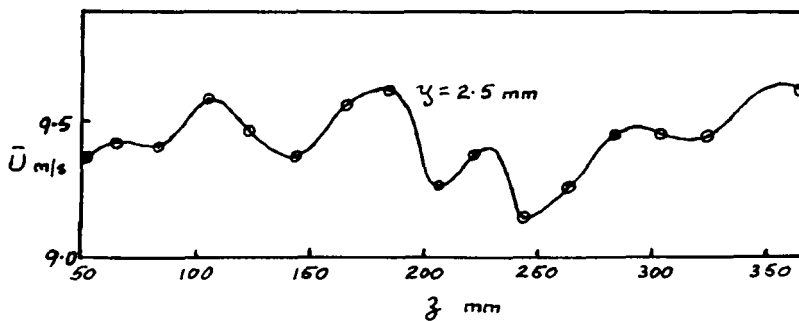


FIGURE 6. Spanwise distribution of mean velocities 10mm upstream of the trip at one position in the boundary layer.

9.3. Fully-Developed Nature of the Flow Upstream of the Step

In order to determine whether the flow had become "fully developed" as it approached the step, and also to check some of the instrumentation, it was decided to obtain profiles through the boundary layer at $x/H \approx -6$ (actual x position was -225mm) using a Pitot tube, a single hot wire, the miniature X-probe and a standard Disa X-probe (wire $d = 5\mu\text{m}$, $l = 1.25\text{mm}$). To ensure that there was no upstream influence of the step at this point, the step was later

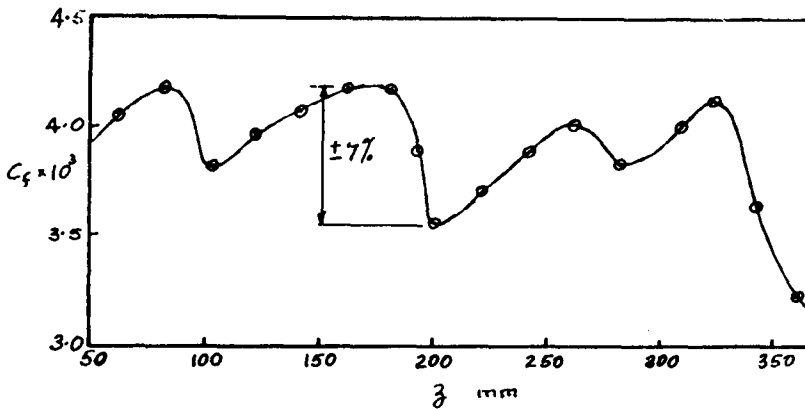


FIGURE 7. Spanwise distribution of C_f values at $x/H \approx -6$

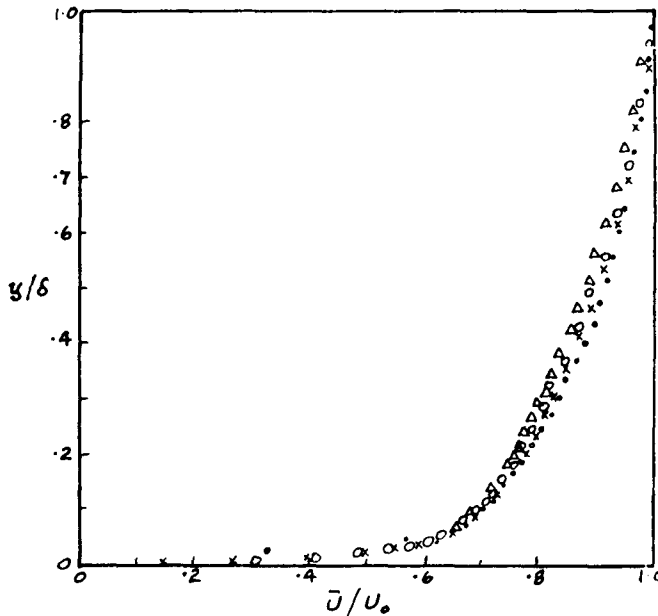


FIGURE 8. Mean velocity distribution across the boundary layer at $x/H \approx -6$.
 · Pitot; × Single hot wire; o Miniature X-probe; Δ Disa X-probe.

“removed” by placing a length of ply-wood, in the downstream section of the tunnel, level with the upstream section, and the profile measurements were then repeated.

All mean velocity \bar{U} profiles, plotted using outer layer values for non-dimensionalizing, gave good agreement — Figure 8.

To compare the velocity profiles using wall variables, it was necessary to determine the local C_f value. This was obtained by three different methods:

- a) Using a Preston tube. The one we used was a flattened tube of height 0.252 mm. (Subsequently, it was found that this corresponded to a height of $y^+ \approx 7$). The data was reduced using the Patel (1965) correlation equations.

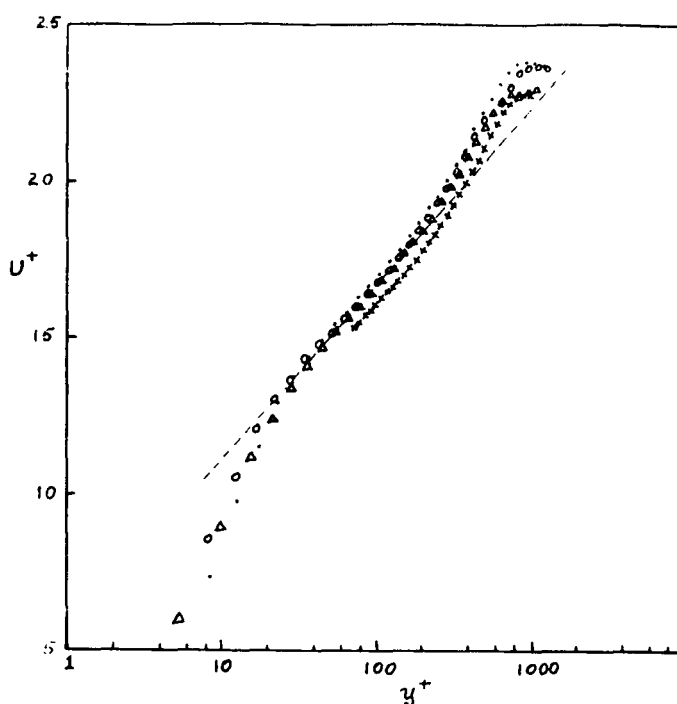


FIGURE 9. Mean velocity distribution across the boundary layer at $x/H \approx -6$.
 • Miniature X-probe with step; ○ Miniature X-probe without step; △ Single hot wire; × DIASA X-probe; — Best fit in log region.

b) Using the Clauser (1954) charts. These are based on

$$U^+ = \frac{1}{0.41} \ln y^+ + 5.1$$

c) Using the Coles (1962) curves of R_θ vs C_f . From the mean velocity profiles, a momentum thickness, θ , of 2.55mm was obtained at $x/H \approx -6$ so that, for the flow at this position, $R_\theta = 1680$.

The results from the three methods were:

- a) $C_f = 3.854 \times 10^{-3}$
- b) $C_f = 3.925 \times 10^{-3}$
- c) $C_f = 3.810 \times 10^{-3}$

A mean value of $C_f = 3.86 \times 10^{-3}$ was therefore used. This gave $u_\tau = 0.44\text{m/s}$ for a free stream velocity of 10.0m/s . The resulting velocity profiles, normalized using wall values, are shown in Figure 9.

The curves are in good agreement except for the DISA probe. All curves have not been shown in Figures 8 and 9, but it was clear that the curves obtained with and without step were practically identical. The best fit straight line in the log region (Figure 9, neglecting the DISA results) is:

$$U^+ = \frac{1}{.404} \ln y^+ + 5.35$$

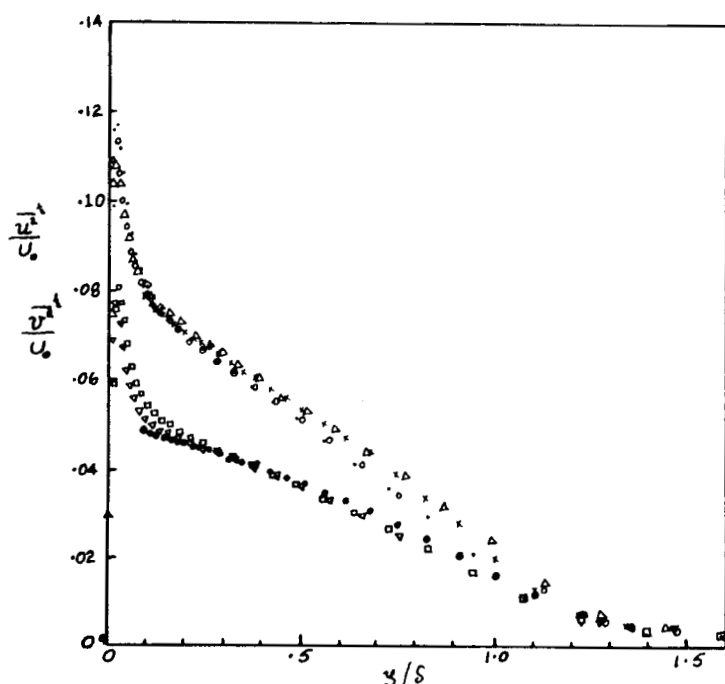


FIGURE 10. Distribution of $\overline{u'^2}^{1/2}$ and $\overline{v'^2}^{1/2}$ across the boundary layer at $x/H \approx -6$ (Outer scaling).

$\overline{u'^2}^{1/2}$: • Miniature X-probe with step; ○ Miniature X-probe without step;
 △ Single hot wire; × DISA X-probe
 $\overline{v'^2}^{1/2}$: ◻ Miniature X-probe with step; ▽ Miniature X-probe without step;
 • DISA X-probe.

which is close to the fully developed case.

The strength of the wake, using the miniature X-probe results, is $\Delta U^+ = 1.4$. For a zero pressure gradient, Cole's (1962) curve of π vs R_θ gives a wake strength of 1.90 for $R_\theta = 1680$. Our wake strength indicates a slightly favorable pressure gradient.

Based on the mean velocity profiles, it would appear that at 6 step heights upstream of the step, the flow is close to the fully developed state and that there is no influence of the step on the flow.

9.4. Turbulence Quantities in Boundary Layer Upstream of Step

Turbulence quantities from the single hot wire, from the miniature X-probe and from the DISA X-probe, obtained at the six step heights upstream of the step position, were compared with one another with published data.

The $\overline{u'^2}^{1/2}$ results are shown in Figure 10 using outer scaling and in Figure 11 using inner scaling.

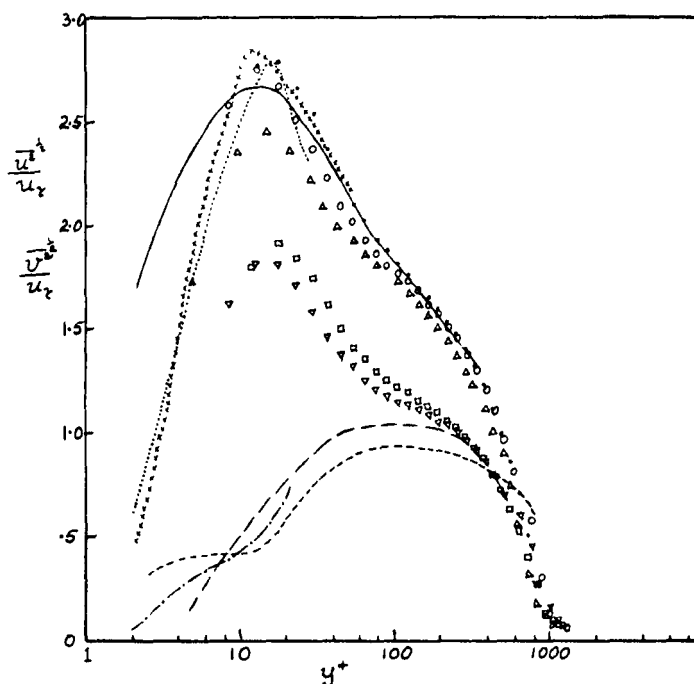


FIGURE 11. Distribution of $\overline{u^2}^{1/2}$ and $\overline{v^2}^{1/2}$ across the boundary layer at $x/H \approx -6$ (Inner scaling). Symbols as for Figure 10.

$\overline{u^2}^{1/2}$: — Spalart (1988); ... Eckelmann (1974); $\times \times \times$ Andreopoulos et al. (1984).

$\overline{v^2}^{1/2}$: --- Spalart (1988); - - - - Eckelmann (1974); - - - - Andreopoulos et al. (1984)

All values in Figures 10 and 11 appear to be reasonable except for the $\overline{v^2}^{1/2}$ values obtained with the miniature X-probe. For this probe, the values obtained between $y^+ = 10$ to $Y^+ = 100$ ($y = .36$ to 3.6 mm) are much higher than the usual values reported in the literature. Perry et al (1987) reported on and discussed at some length the difficulty of obtaining consistent v^2 measurements in the inner regions of boundary layers. Their survey of 13 published results for smooth-wall boundary layers shows the scatter of results obtained and is reproduced in Figure 12, together with the value that we obtained at that position in the boundary layer.

Our maximum value agrees with the values reported at higher von Karman numbers. These discrepancies need further investigation for clarification, although it should be noted that the "non-isotropy," indicated by the difference between the $\overline{u^2}$ and $\overline{v^2}$ values, seems rather high for the curves drawn in Figure 11.

The \overline{uv} results are shown in Figure 13 using outer scaling and in Figure 14

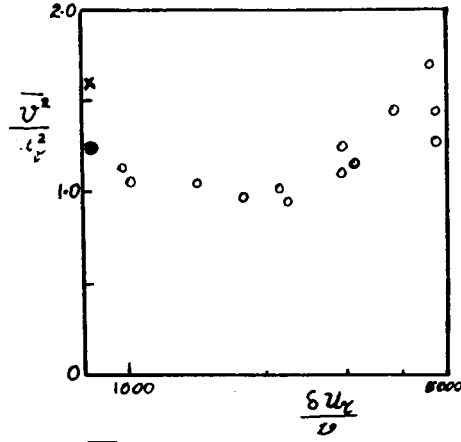


FIGURE 12. Values of $\overline{v^2}$ reported in the literature at $y/\delta = 0.1$ in a smooth-wall turbulent boundary layer. [Perry et al (1987)].

- Literature values — see Perry et al (1987) for details;
- Value obtained with miniature X-probe at $Y/\delta = .1$.
- × Maximum value obtained with miniature X-probe.

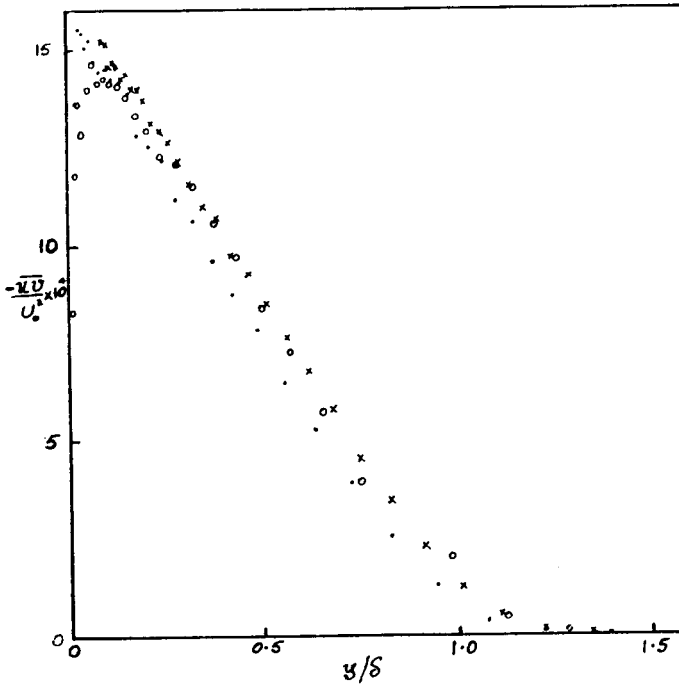


FIGURE 13. Distribution of $-\overline{uv}$ across the boundary layer at $x/H \approx -6$ (Outer scaling).

- Miniature X Probe with step; ○ Miniature X-probe without step; × DISA X-probe.

using inner scaling.

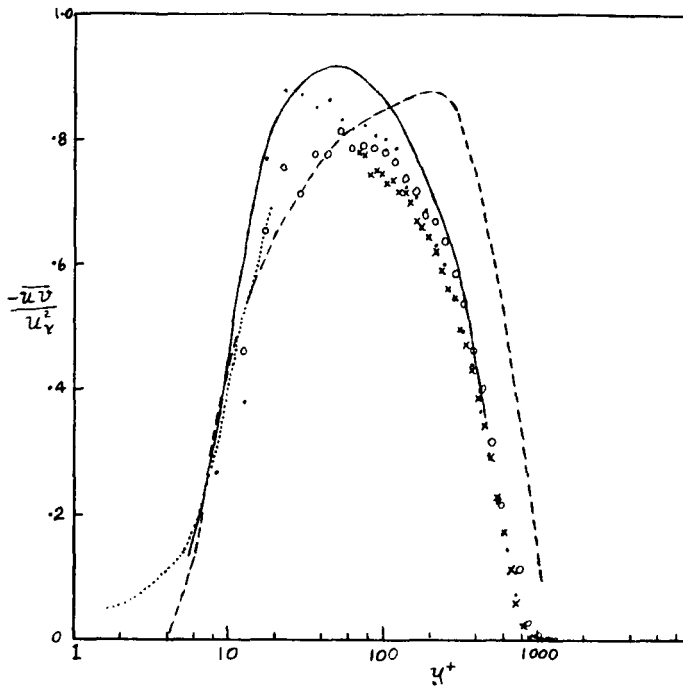


FIGURE 14. Distribution of $-\overline{u'v'}$ across the boundary layer at $x/H \approx -6$ (Inner scaling).

· Miniature X-probe with step; ○ Miniature X-probe without step; × DISA X-probe.

— Spalart (1988); ... Eckelmann (1974); --- Andreopoulos et al (1984).

Except for the Andreopoulos et al (1984) curve in the outer regions of the flow, all results show reasonable agreement for the $\overline{u'v'}$ values. It is perhaps a little strange that results which are in agreement in $\overline{u^2}^{1/2}$ (Figure 11) and $\overline{u'v'}$ (Figure 14) should be so different in the $\overline{v^2}^{1/2}$ values (Figure 11).

9.5. Characteristics of Tunnel Flow Approaching Close to Step

When the Preston tube was traversed in the X direction along the plate (at $z = 252\text{mm}$ — our standard z position) from $x = -350\text{mm}$ to the lip of the step, we were surprised to find significant departures of C_f from the expected values — see Figure 15.

This seemed to indicate an upstream influence of the step and, from published work on backward facing step flows, such an influence had not been expected. Consequently, using the C_f curve as a guide, five stations ($x/h = -2.6, -1.5, -0.53, -0.13$, and $-0.$) were selected for detailed profile studies. Since the miniature X-probe had given reasonable results, it was used for these profiles in order to allow measurements to be made as close to the wall as possible.

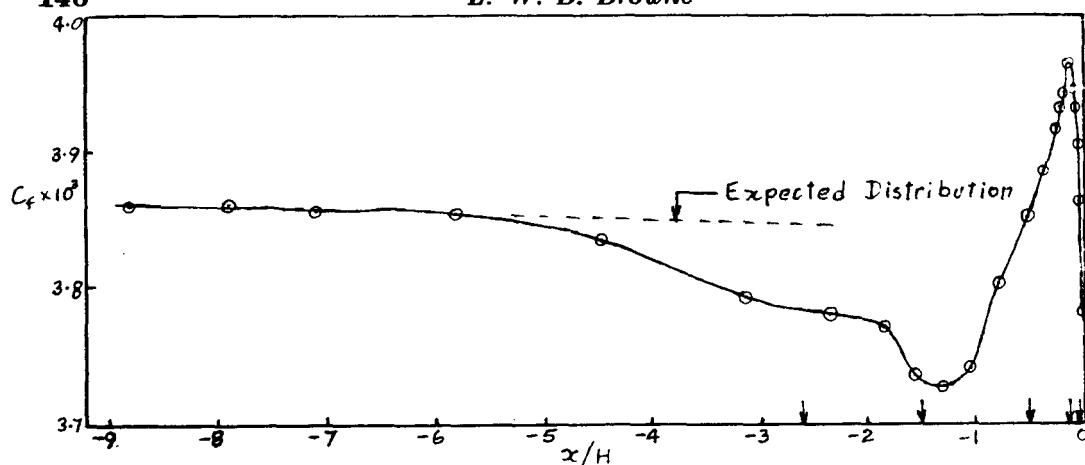


FIGURE 15. Distribution of C_f values near and upstream from the step. The arrows indicate stations where detailed profiles were taken.

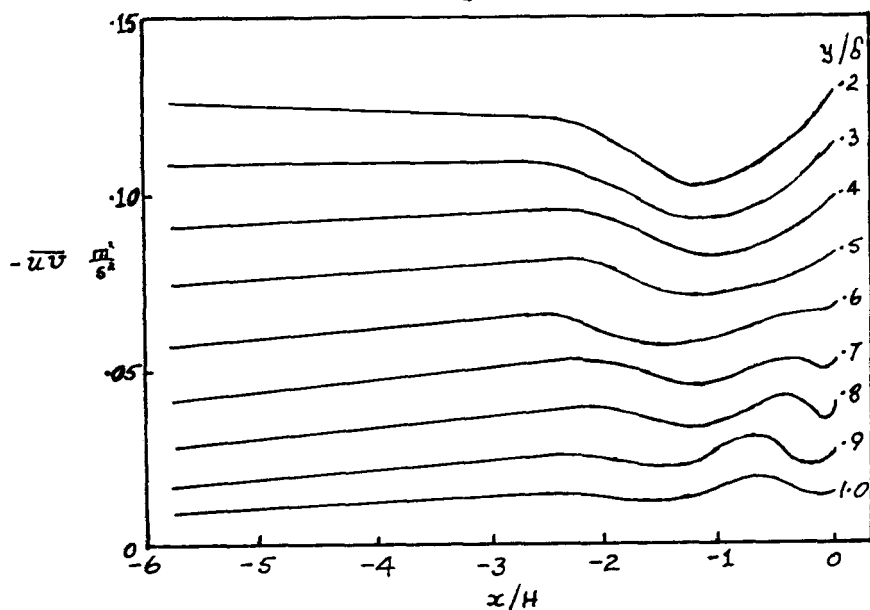


FIGURE 16. Distribution of $\overline{u'v'}$ in the outer regions of the boundary layer, upstream from the step.

The changes indicated by the C_f profile (Figure 15) were reflected in the turbulence quantities - in particular in the $\overline{u'v'}$ values, as shown in Figures 16 and 17.

The minimum of $-\overline{u'v'}$ in the inner part of the flow, Figure 17, occurs at approximately the same point ($x/H = -1.4$) as the minimum in the C_f curve, Figure 15. In the outer part of the flow, Figure 16, there are obviously some complex changes occurring in the large scale structures. The negative values of $-\overline{u'v'}$ that were measured at $y^+ = 10$ cannot be substantiated at this stage and

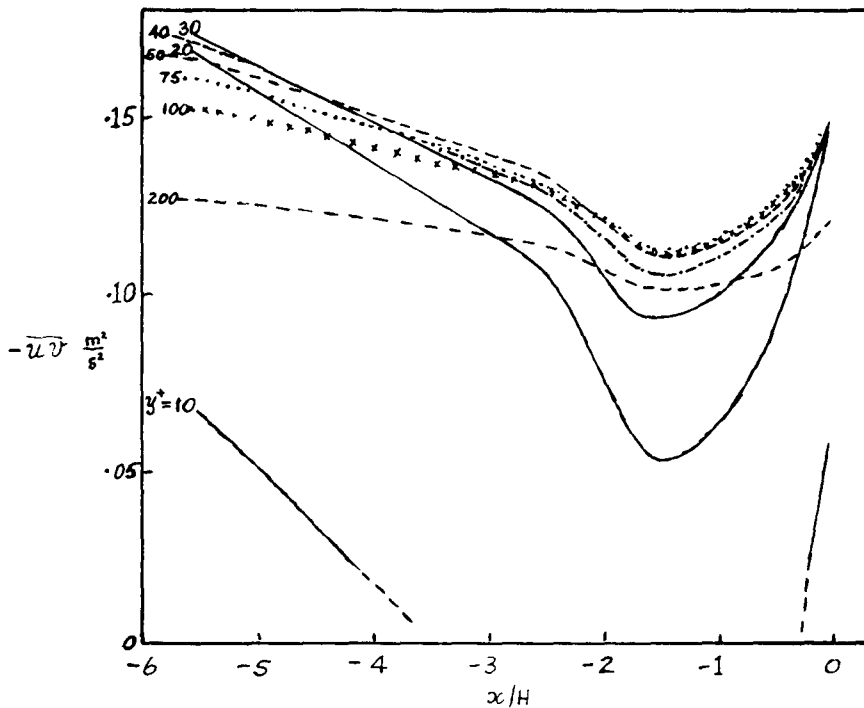


FIGURE 17. Distribution of \overline{uv} in the inner regions of the boundary layer, upstream from the step.

may be due to the problems associated with X -wire measurements so close to the wall. A probe with wires of say $0.63\mu\text{m}$ diameter and 0.1mm long may be required to resolve this region.

The mean \bar{v} velocities also follow the changes in the C_f curve, although in the opposite sense - peaking at minimum C_f and reaching a minimum at maximum C_f , Figure 18.

This upstream influence of the step does not seem to have been previously reported in the literature, although three instances of support for our results have been obtained:

- a) In discussions with Dave Driver, he said that he had observed, in his work on the backward facing step, an increase in C_f (one data point) as the step was approached. This point was shown in the paper of Monson et al (1981) but was not commented on. The C_f values for their flow were different to ours, but by shifting the C_f origin and using the boundary layer thickness for non-dimensionalizing the distance from the step, some agreement is obtained between their C_f values and ours - see Figure 19.

It is interesting to note that Monson et al (1981) obtained their C_f values using laser interferometry - a completely different technique to the Preston tube approach that we used.

- b) In 1981, M. Sindir carried out, for NASA-Ames, numerical simulation work,

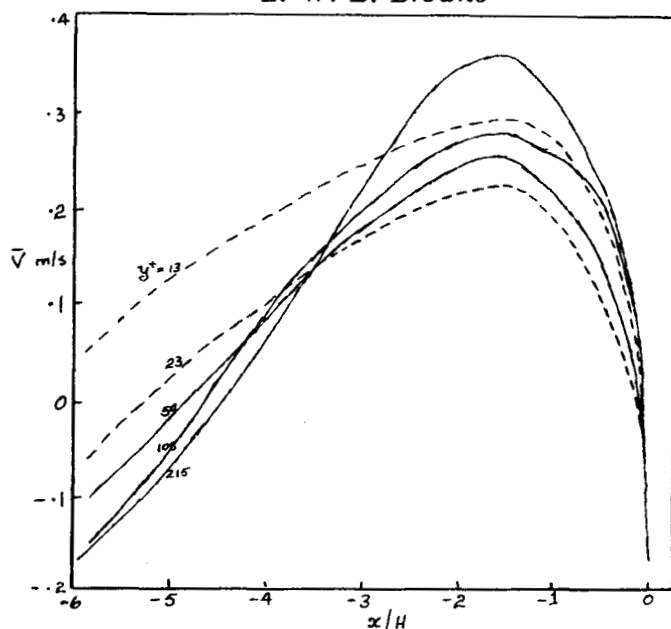


FIGURE 18. Distribution of \bar{U} in the inner regions of the boundary layer, upstream from the step.

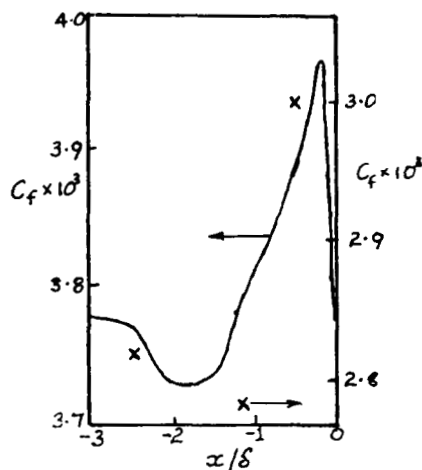


FIGURE 19. C_f values approaching the step.

— Our results, Figure 15. x Monsom et al (1981) results.

using modified TEACH programs, on flow over a backward facing step. In discussions with John Viegas concerning this work, John showed me the output from a program that he had run, using Sindir's algebraic stress model program. It was observed that the pressure values, and these values only, did indicate some influence upstream of the step - the negative pressures in the recirculating zone extending upstream about two step heights from the step. The extent of the negative zone, above the surface, was about half a step

height at the step, decreasing to zero at 2.5 step heights from the step. These pressure values, however, show non-monotonic changes, indicating that a finer grid is required in this region of the flow.

- c) In his computational solution of the laminar flow over an aerofoil section, Jim Brown (EFD branch, NASA-Ames) showed that the C_f distribution had a distinct dip and then recovery just before reaching the trailing edge, in many ways emulating the curve of Figure 15.

We conclude that the upstream influence of the step is a feature of the flow and may be an important consideration when direct simulations of the flow are attempted.

9.6. Measurements Made Relating to the Large Scale Structures

To study the large scale structures in the flow, it was decided to carry out initial measurements in the boundary layer upstream of the step. There were two reasons for this choice. Firstly, there is available considerable published material on the large scale structures in a boundary layer. Our results could then be of a corroborative nature and also perhaps, by judicious placement of the sensors and analysis of the data, contribute to the understanding of these structures - particularly with regard to the influence, one on the other, of the outer and inner structures.

Secondly, any experimental and analysis techniques developed for this part of the flow could be applied equally well to the other regions of the flow — the “mixing layer” region and the region downstream of reattachment. All initial experiments were, therefore, carried out at $x = -100\text{mm}$ ($x/H = -2.63$) where the step influence has hardly yet begun to have any major effect. For those measurements the floor plate was heated to a uniform temperature of about 10°C above the free-stream temperature, as described earlier.

The first experimental set-up consisted of two cold wire sensors at $y^+ \approx 10$ from the wall and separated from each other by $\Delta z^+ \approx 100$. The 3-wire miniature probe (X-wire + cold wire) was traversed between these two wires from $y^+ \approx 10$ to the outer regions of the boundary layer — data being taken at 30 stations. A typical time trace from the five sensors is shown in Figure 20.

Some structures can be discerned from the traces of the two wires closest to the wall. Sudden changes in the u signal also correspond to sudden changes in the temperature signals indicating that, as others have found, the u signal near the wall is a suitable structure detector.

The second experimental set-up, for investigating the large scale structures, consisted of 14 sensors. The previous 5 sensors were complemented by a further 5 cold wires arranged in a vertical array and 4 cold wires arranged in a horizontal array. Each of the wires in the vertical array was separated by approximately 5mm ($\Delta y^+ \approx 140$) while the wire that was closest to the wall was at $y^+ \approx 90$. To allow for the y traverse of the 3-wire sensor, it was necessary to offset the vertical array by about 4mm ($\Delta z^+ \approx 110$) from the centre-line of the traverse.

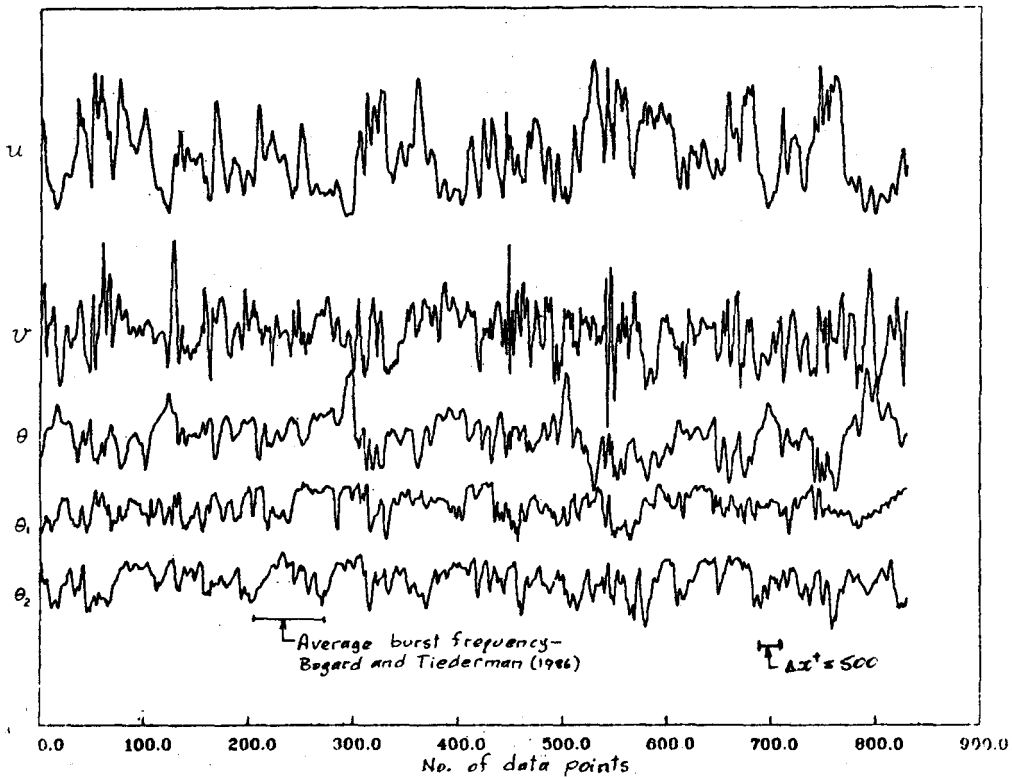


FIGURE 20. Time traces of velocity and temperature fluctuations. $x = -100\text{mm}$, $y^+ = 14$. θ : on 3-wire probe, θ_1 and θ_2 : at $y^+ = 10$

The horizontal array had 2 wires on one side of the traverse centre-line and 2 wires on the other side. This array was situated at about the half-boundary-layer distance from the surface and spanned a total width of about 30mm ($\Delta z^+ \approx 840$). Data was obtained from all sensors as the 3-wire probe was moved to 30 stations across the boundary layer. Typical traces from the 14 sensors, obtained when the 3-wire probe was at $y = 14.8\text{mm}$ ($y^+ = 415$) are shown in Figure 21.

A large scale structure can be noted as being detected simultaneously on a number of wires, as indicated by the crosses in Figure 21. The wire for θ_7 is obviously in the intermittent region of the flow.

A program was written to enable large scale structures to be detected, using data similar to Figure 20 or 21, by any single channel or combination of channels, using the WAG, Bisset et al (1958), method. This program was run and the detections made compared favorably with the "by-eye" detections using the time traces.

There was no time for further work by the author at this stage.

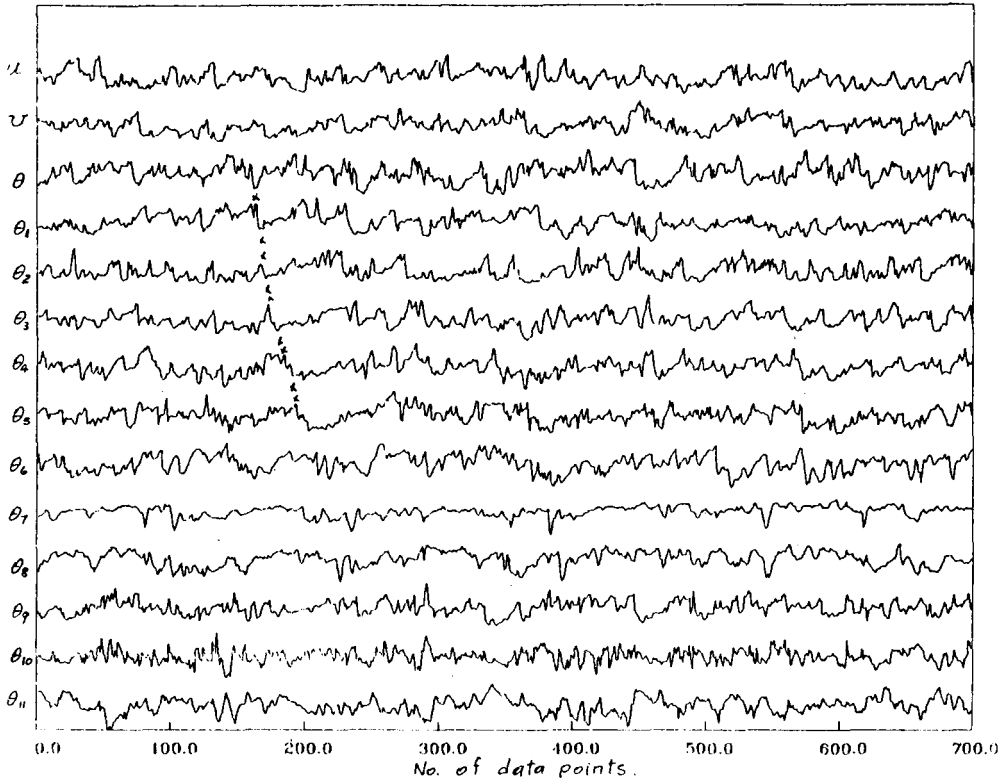


FIGURE 21. Typical time traces of velocity and temperature fluctuations using 3-wire probe (u, v, θ), 2 near-wall cold wires (θ_1, θ_2), a rake of 4 horizontal cold wires (θ_3 to θ_6), and a rake of 5 vertical cold wires (θ_7 to θ_{11}). $X = -100\text{mm}$, $y^+ = 415$.

10. Next Phase of the Work

Broadly, the next phase of the work is to apply the detections made using the above program to obtain conditionally sampled values of the velocities (u and v) at each station across the boundary layer. These values should be obtained for the inner and outer regions of the flow and also for, say, only those structures with the most common spacing. The results for structures with other spacings will also need to be checked. Some correlation work is necessary to determine the relative position of the conditioned velocities. Topologies of the inner and outer regions can then be built up and the distribution ("coherent" and "random") of momentum and heat transfer quantities determined. The other regions of the flow — the mixing layer and boundary layer after reattachment — can then be examined in a similar manner.

REFERENCES

- ANDREOPOULOS, J., DURST, F., ZARIĆ, Z., & JOVANOVIĆ, J. 1984 Influence of Reynolds number on characteristics of turbulent wall boundary layers. *Exp't. in Fluids*. **2**, 7-16.
- BISSET, D.K., ANTONIA, R.A., & BROWNE, L.W.B. 1988 Spatial organization of large structures in the turbulent far-wake of a cylinder. *J. Fluid Mech.* (submitted)
- BOGARD, D. G., & TIERDERMAN, W. G. 1986 Burst detection with single-point velocity measurements. *J. Fluid Mech.* **162**, 389-413.
- BRADSHAW, P. 1965 The effect of wind tunnel screens on nominally two-dimensional boundary layers. *J. Fluid Mech.* **22**, 679-687.
- CLAUSER, F. H. 1954 Turbulent boundary layers in adverse pressure gradient. *J. Aero. Sci.* **21**
- COLES, D. 1962 The turbulent boundary layer in a compressible fluid. Report No. R-403-PR, Rand Corp., Santa Monica.
- DENGEL, P., & FERNHOLZ, H. H. 1988 Generation of and measurements in a turbulent boundary layer with zero skin friction. Second European Turbulence Conference, Technische Universitat Berlin, Poster Presentation, Topic F.
- ECKELMANN, H. 1974 The structure of the viscous sublayer and the adjacent wall region in a turbulent channel flow. *J. Fluid Mech.* **65**, 439-459.
- MEHTA, R. D., & HOFFMANN, P. H. 1987 Boundary layer two-dimensionality in wind tunnels. *Exp'ts. in Fluids*. **5**, 358-360.
- MONSON, D. J., DRIVER, D. M., & SZODRUCH, J. 1981 Application of laser interferometer skin-friction meter in complex flows, IEEE publication, Proceedings of the International Congress on Instrumentation in Aerospace Simulation Facilities, Dayton, Ohio, pp. 232-243.
- PATEL, V. C. 1965 Calibration of the Preston tube and limitation on its use in pressure gradients. *J. Fluid Mech.* **23**, 185-208.
- PERRY, A. E., LIM, K. L., & HENBEST, S. M. 1987 An experimental study of the turbulence structure in smooth-and rough-wall boundary layers. *J. Fluid Mech.* **177**, 437-466.
- SPALART, P. R. 1988 Direct simulation of a turbulent boundary layer up to $Re_\theta = 1410$. *J. Fluid Mech.* **187**, 61-98.
- SWEARINGEN, J. D., & BLACKWELDER, R. F. 1987 The growth and breakdown of streamwise vortices in the presence of a wall. *J. Fluid Mech.* **182**, 255-290.

The effects of stabilizing and destabilizing longitudinal curvature on the structure of turbulent, two-stream mixing layers

By M. W. PLESNIAK AND J. P. JOHNSTON

1. Introduction

1.1 Background

The topic of the research program is mixing and turbulence transport in parallel, co-flowing, two-stream shear or mixing layers. In particular the effects of streamwise (longitudinal) curvature on the growth and development of the shear layer were investigated. The preliminary results of the present research program are reported in Plesniak and Johnston (1987), where results are presented for stable and unstable (in the Taylor-Görtler (T-G) sense) mildly curved two-stream mixing layers. These results are compared to a plane mixing layer studied in the same facility under nearly identical initial and boundary conditions. At typical operating conditions, a nominal speed ratio of 0.5 with flow speeds of 12 and 24 cm/s was employed. The ratio of the shear layer thickness to the radius of curvature is less than 5%. Reynolds numbers based on ΔU and momentum thickness ranged from 1000 to 2000 (5000 to 10000 based on vorticity thickness) over the region in which measurements were made. Laminar flow exists at the splitter plate trailing edge due to the low operating velocities. The average momentum thickness Reynolds number in the trailing edge boundary layers is estimated to be 190, too low for a trip to be effective. The mixing layer was not artificially forced and often exhibited more than one frequency of roll up. Dye flow visualization along with single component LDV results are presented for all three cases.

Flow visualization indicated that for stabilizing curvature vortex mergings (pairings and triple interactions) are common, but there is little mixing of the dye across the layer and fine-scale three-dimensionality does not occur in the region studied. Conversely, destabilizing curvature promotes mixing at all scales and the layer is characterized by complex three-dimensional structures. Vortex interactions are also less prevalent for the unstable case than for the stable or plane layers.

The LDV measurements showed that the unstable layer exhibits a greater growth than the plane or the stable layer of nearly the same velocity ratio (growth rate was determined from the maximum slope thickness). The mean (U) and fluctuating (u') streamwise velocity profiles exhibited self-similarity for all three cases studied. However the fluctuating normal (v') profiles were not

self-similar for either the stable or unstable layer. Peak fluctuation levels in both components were greatest for the unstable layer.

1.2 Current Research

The main goal of the research program is to gain a fundamental understanding of the physics of curved, turbulent, unforced free mixing layers and to provide a data base for turbulence modelers. Since the facility was previously instrumented only with a one-component LDV system, the major objective was to construct a two-component LDV system to allow the measurement of Reynolds stresses and examine turbulence transport in the mixing layers.

2. Approach

2.1 Documentation of Initial Conditions

It is well known that the scatter in data from various sources regarding free shear layers is large. This is due to the mixing layer's extreme sensitivity to initial conditions. A number of studies have been undertaken to examine the effects of initial conditions and side-wall confinement effects on the growth of free shear layers. These studies attempted to resolve the discrepancies in the literature concerning spreading rates and other characteristics of mixing layers. However conflicts regarding the effects of laminar vs. turbulent boundary layers at separation, initial fluctuation level, initial momentum thickness and influence of splitter-plate trailing-edge thickness on the streamwise evolution of the shear layer still exist. Some groups report confinement effects of boundaries while others do not.

In view of many unresolved issues concerning initial and boundary condition effects it is considered important to document the initial conditions of the present study. The two-component LDV system described below is being used to investigate the boundary layers on the high and low speed sides of the splitter plate. Determination of the momentum thicknesses will allow us to predict the most unstable frequency and compare to the results in Ho and Huerre (1984). The levels of free stream turbulence in the nozzle will also be measured with this system.

Another issue which has recently been addressed in the literature is spanwise nonuniformity in the mixing layer and the formation of small-scale streamwise vortical structures due to natural disturbances. Jimenez (1983), Lasheras et al (1986, 1988), Bernal and Roshko (1986), Mehta; Ho (private communications), and others have reported on the presence of these structures in plane mixing layers. They are easily detectable in spanwise variations of the mean streamwise (U) velocity profiles. Since these structures have never been studied in curved mixing layers, it is unknown whether there is any interaction with the T-G structures resulting in their suppression or enhancement.

2.2 Flow Visualization Studies

Previous results obtained with vegetable dye visualization were able to show diffusion of the dye across the layer and also the entrainment of ambient fluid into the layer. VHS format videotape movies showed large-scale structures which transported dye across to opposite sides of the shear layer in the case of destabilizing curvature. However the dye visualization technique had several limitations: the major being the rapid diffusion of dye in the fully turbulent regimes restricting the operating velocities lower than those used in acquiring the quantitative data.

Thus, for the present study a hydrogen bubble technique with portable laser sheet illumination was employed. The wire may be positioned at any location in the mixing layer along the entire length of the test section. Using existing equipment, timelines can be generated by pulsing the wire. This technique will enable us to visualize the transport of turbulence (and of mass if the Schmidt number of the bubbles is low enough) by the structures of various scales. In particular, the large scale motions associated with the T-G rollers in the unstable layer can be studied. A suitable lighting source is currently being sought to illuminate a 2-D grid of hydrogen bubble wire used to visualize an entire plane across the mixing layer.

2.3 Velocity Data

After unexpected delays in delivery of the necessary components the two/three-component LDV system has been constructed, optically aligned and calibrated. Preliminary two-component velocity profiles have been obtained for the stable and unstable layers. However, these data suffer convergence problems in the mixed (uv) moments due to insufficient numbers of samples. More complete data being presently acquired correct this problem. In addition the third component capability (w measured with an immersible fiber optics probe) has recently been added to the system so that the entire 3-D velocity field may simultaneously be acquired and the full Reynolds stress tensor computed.

2.3.1 Description of the 2-Component LDV

A three-color, two-component LDV system powered by a 3-Watt Argon-ion Lixel laser was constructed for turbulence studies in the curved mixing layers. The system employs frequency shifting on both channels and is configured to operate in the backscatter mode. The entire system is mounted on an optical breadboard which may be traversed in a rectilinear X - Y global coordinate system.

An aluminum traversing cart made of 2×4 inch square tubing (1/8 inch wall thickness) chosen for its light weight and stiffness was constructed to traverse the optical system. The traverse rides on pillow block linear bearings over a 1 inch diameter ground stainless steel shaft. Positioning in the global streamwise

direction (X) is performed manually over a travel of 12 feet (3.66 m). The direction normal to this (Y) has a travel of 4 feet (1.22 m). Thus, any point across the entire outer channel may be accessed.

In order to traverse along a radial line in the inner curved test section, programmable computer controlled stepper motors are used. The stepper motors are driven by Superior 430-TH translator modules operating in a chopped mode. An Anaheim Automation CL1605 programmable controller board is used to control the translator modules. Parameters such as motor speed, acceleration, and limit switch condition are controlled by the board. A serial RS-232 interface is used to communicate to the CL1605 with the data acquisition computer system.

A ball nut/screw assembly with a lead of 0.250 in (6.35 mm) is used for positioning in the Y direction while a lead screw unislide assembly with a lead of 0.100 in (2.54 mm) is employed for fine positioning over 10 inches (0.254 m) of travel in the global X direction. The stepper motors are driven in a half-step mode which produces a resolution of 400 steps/revolution. This allows a positioning resolution of 0.00025 in/step (0.00635 mm/step) in the X direction and 0.000625 in/step (0.015875 mm/step) in the Y direction. Backlash in X was measured to be 0.001 in (0.0254 mm) and in Y , 0.003 in (0.0762 mm).

A radial move in the local x - y coordinate system of the curved shear layer consists of two moves in the global X - Y coordinate system. The angle between a radial line in the local coordinates and the global coordinate system is determined experimentally. Considering spatial resolution in X and Y , backlash and uncertainty in determining the angle, the resolution in positioning accuracy is less than half of the LDV measuring volume diameter (100 microns).

One limitation of this traversing system is that no automated spanwise traversing is possible due to design constraints resulting from lack of funding. However, the He-Ne based fiber optics probe traverse does have spanwise capability and can be used when such measurements are dictated.

2.3.2 Present LDV Measurements

The two-component LDV system described above is being used to make measurements in the curved mixing layer for three different configurations: straight (reference), stable and unstable with a velocity ratio of 2:1. Measurements of complete profiles (20 to 30 spatial points) at approximately 8 streamwise stations will allow accurate determination of the mean growth rate and evolution of the shear layers' turbulence fields. In conjunction with the fiber optics probe, three components of velocity (u, v, w) can be measured. Acquisition of all three velocity components simultaneously allows the entire Reynolds stress tensor to be computed and estimates of the turbulent energy budget can be made. Complete time records are saved at each position for post-processing. Mean and rms velocities, Reynolds stresses, higher order moments (skewness and kurtosis), and velocity probability density functions will be calculated.

Separate runs with much longer record lengths necessary to resolve the lowest frequencies will be made for spectral and autocorrelation data acquisition at several points in the mixing layer. Since we have two independent LDV systems (1-component probe and 2-component system), it will be possible to obtain two-point spatial correlations by positioning the probes at different points in the mixing layer. This kind of data may be particularly useful in tracking the large T-G rollers in the unstable layers.

3. Summary

A major portion of the period covered under CTR funding was spent on the construction and development of the multi-component traversing system and associated control hardware and software. Delays in delivery of necessary components delayed construction by several months. The system was first used to make measurements in October, 1988.

In addition to acquiring the two-component measurement capability, a hydrogen bubble/laser sheet flow visualization technique was developed to visually study the characteristics of the mixing layers. With this new technique we can look for evidence of the large-scale rollers arising from the Taylor-Görtler instability and study its interaction with the primary Kelvin-Helmholtz structures.

In general, the recently acquired data confirm the results reported in our preliminary paper (Plesniak and Johnston, 1987). At this stage we are making two and three-component measurements and will be able to report information regarding the transport of turbulence and full Reynolds stress data in several months.

REFERENCES

- BERNAL, L. P. AND ROSHKO, A. 1986 Streamwise Vortex Structure in Plane Mixing Layers. *J. Fluid Mech.* **170**, 499-525.
- HO, C-H AND HUERRE, P. 1984 Perturbed Free Shear Layers. *Ann. Rev. Fluid Mech.* **16**, 365-424.
- JIMENEZ J. 1983 A Spanwise Structure in the Shear Layer. *J. Fluid Mech.* **132**, 319-336.
- LASHERAS, J. C., CHO, J. S. AND MAXWORTHY, T. 1986 On the Origin and Evolution of Streamwise Vortical Structures in a Plane, Free Shear Layer. *J. Fluid Mech.* **172**, 231-258.
- LASHERAS, J. C. AND CHOI, H. 1988 3-D Instabilities of a Plane Free Shear Layer: An Experimental Study of the Formation and Evolution of Streamwise Vortices. *J. Fluid Mech.* **189**, 53-86.

- PLESNIAK, M. W. AND JOHNSTON, J. P. 1987 The Effects of Stabilizing and Destabilizing Curvature on a Turbulent Mixing Layer, Proc. of the 2nd Int'l Symp on Transport Phenomena in Turbulent Flows, Tokyo, October 25-29, pub. in *Transport Phenomena in Turbulent Flows: Theory, Experiment, and Numerical Simulation*, (1988) Hemisphere Publishing Corp., M. Hirata and N. Kasagi, ed. 377-390

An experimental investigation of a low Reynolds number turbulent boundary layer subject to an adverse pressure gradient

By J. H. WATMUFF

Summary

This report covers a 12 month period from the beginning of the project. The project concerns an experimental study of a very low Reynolds number turbulent boundary layer subject to an adverse pressure gradient. The work is being performed in the Boundary Layer Wind Tunnel in the Fluid Mechanics Laboratory at NASA Ames Research Center in collaboration with Dr. R.V. Westphal. The aim is to obtain highly accurate mean-flow and turbulence measurements under conditions that can be closely related to the numerical simulations of Philippe Spalart for the purposes of CFD validation. It is expected that the experimental results will also serve as a useful contribution to the research literature in their own right.

Much of the Boundary Layer Wind Tunnel has been completely rebuilt with a new wider contraction and working section which will improve compatibility with the simulations. A unique sophisticated high-speed computer controlled 3D probe traversing mechanism has also been integrated into the new test section. Construction of the tunnel and traverse has consumed a large fraction of the period covered by this report and is discussed in some detail. The hardware is now complete, and measurements are in progress. The mean-flow data indicate that a suitably two-dimensional base flow has been established.

Automation of the probe positioning and data acquisition have led to a decreased running time for total pressure measurements. However, the most significant benefits are expected to occur when using hot-wire probes. Calibrations can be performed automatically and there is no need to handle fragile probes when moving between measuring stations. Techniques are being developed which require sampling of the signals from moving hot-wire probes on the basis of their position in the flow. Measurements can be made in high intensity turbulence by flying probes upstream at high speed so that the relative magnitude of the turbulent velocity fluctuations are reduced. In regions where the turbulence intensity is not too large, the probe can also be repetitively scanned across very dense spatial grids in other directions. With this new technique, a complete profile can be measured in about 1/3 the time and with a spatial density about 50 times that obtainable using a stationary probe.

1. Background

1.1 CFD Simulations

The numerical method used by Spalart (1988) is spectral in space and second-order in time. An important feature of the method is that there is no turbulence modelling. However, this requires a high grid density which restricts the simulations to low Reynolds numbers i.e. $Re_\theta < 1500$. Periodic spanwise and streamwise conditions are used and a multiple-scale procedure is applied to approximate slow streamwise growth. The key assumptions are that the streamwise evolution of the flow is slow and that the straining of the turbulence by the mean-flow can be neglected. Spalart has suggested that the assumption of small streamwise growth will cause the method to breakdown for large adverse pressure gradients.

1.2 Relationship between the experiment and simulation

There are three major requirements in the relationship between the experiment and simulation. Firstly, the Reynolds number of the experiment must match that of the simulation precisely. Secondly, the experiment and simulation also must have closely matched initial conditions. The simulation begins at the first station with an equilibrium boundary layer. A mildly favorable pressure gradient can be used to very closely approximate a "self-preserving layer" in the experiment, i.e. by careful experimental design the boundary layer can be maintained at almost constant thickness over some streamwise distance before being subjected to the adverse pressure gradient. Following a suggestion by Inman and Bradshaw (1981) the length of this region could be increased to allow any upstream trip effects to decay before the region of interest. Finally, accurate experimental pressure coefficient (C_p) measurements with high spatial resolution are required as an input for the simulation. A suitable flow configuration for the computations would be one in which the boundary layer experienced a non-dimensional pressure gradient $\beta_x = \frac{\delta^*}{\tau_w} \frac{dP}{dx} \approx 2$ at a maximum $Re_\theta \approx 1500$.

1.3 Preliminary experimental measurements

The combined requirements of low Reynolds number and accurate pressure measurements precludes the use of water as a flow medium or the use of very low air velocities (e.g. 0.5 m/s) for the experiment. R.V. Westphal used momentum integral boundary layer calculations as a design tool to show that the Boundary Layer Wind Tunnel in its old form was a suitable facility for the experiment. Preliminary mean-flow measurements verified that this facility could duplicate the Reynolds number and pressure gradient requirements of the simulations. A flat test surface was employed for the boundary layer development, and the pressure gradient was imposed by a contoured upper control wall. The inlet flow velocity was 8.2 m/s. An inlet free-stream velocity around 8 m/s was considered to be close to the lower limit for accurate C_p measurements, i.e. a total head of

0.15 inches of water with an accuracy of $\pm 1\%$. The mean-flow two-dimensionality appeared to be good since the streamwise momentum balance was found to be within 10%.

In the region of adverse pressure gradient at an $R_\theta \approx 1500$ the reduced profile data showed a $\beta_x \approx 0.7$ which is a little low. A stronger adverse pressure gradient would be required for the current experiment. Also the inlet unit Reynolds number appeared to be a little high. A high inlet unit Reynolds number is undesirable since it shortens the physical distance over which the experiment matches the capabilities of the simulation.

2. New Tunnel Contraction, Test Section and Traverse

2.1 Tunnel Contraction

When formulating the current experiment, it was desirable to use a lower inlet free-stream velocity which would reduce the inlet unit Reynolds number and also provide for better spatial and temporal resolution of hot-wire measurements. However, two factors had to be considered before a lower inlet velocity could be adopted. Firstly, the accuracy of the C_p measurements would need to be maintained. Secondly, an increase in the total free-stream unsteadiness (from about 0.25% to around 0.5%) was observed at low tunnel speeds.

The first restraint was relieved by purchasing the most accurate and sensitive commercially available pressure transducer. This allows the inlet free-stream velocity to be lowered to around 6 m/s (i.e. a total head around 0.08 inches of water) while still maintaining an accuracy of $\pm 1\%$ for the C_p measurements. The second problem appeared to be related to the tunnel fan which was operating near the lower extremity of its characteristics. It was evident that a further drop in the fan speed using the original form of contraction and test section would lead to even more unsteadiness. Instead the flow area of the test section inlet was increased by 50% from 80cm x 20cm to 100cm x 24cm, allowing a lower inlet velocity but at a higher fan speed. This required designing a new 5:1 2D contraction to replace the original 7.5:1 3D version.

Theoretical methods were used for selecting a new Boundary Layer Wind Tunnel contraction design from a number of alternatives. The pressure distribution on the side walls was estimated using a potential flow method. The numerical solution of the stream function inside the contraction and inside upstream and downstream extensions of constant area was used to calculate the velocities on the boundary and the pressure distribution was obtained from the Bernoulli equation. The evolution of the contraction side wall laminar boundary layer subject to this pressure distribution was calculated using a momentum integral method. The effects of streamline curvature and convergence were neglected. The calculations showed that the new contraction design is not likely to cause separation.

2.2 High-speed probe traverse integral with test-section

The numerical simulations usually have very high spatial resolution (e.g. Spalart (1988) used up to 10^7 grid points) but only for a limited number of time steps. This is in complete contrast to the experimental situation where almost unlimited temporal information is available but with very limited spatial content. One way of reducing this discrepancy is for the experimentalist to increase the spatial content of measurements. This dictates that multiple probes and/or more sophisticated traversing equipment be used.

In view of the above considerations, a high-speed 3D computer-controlled probe traversing system has been built. The range of motion is 2.5m in the streamwise X-direction, 0.1m in the Y-direction normal to the wall and 0.5m in the spanwise Z-direction. Minimum top speeds of around 3 m/s in the X-direction and 1.5 m/s in the Y- and Z-directions were desired. These speeds can be reached over a short enough distance with accelerations of 2 g's. Linear stepping motors satisfy the requirements for the Y- and Z-axes for accurate (0.05 mm) high speed (1.5 m/s) positioning. The probe and sting are carried directly by the Y-axis motor. The Y-axis motor rides on a steel platen which is attached to the Z-axis motor, linear bearing and platen assembly. The Z-axis assembly is supported above the test wall within the working section by a gantry which spans the 1m distance between the side walls.

The requirements of the gantry are low mass (to minimize inertial loading), high stiffness (to minimize deflections), and small projected area (to minimize aerodynamic interference). Therefore, the gantry was constructed in the form of a 1m wide truss using sections cut from thin sheets of carbon-fiber composite which were bonded together with epoxy resin. By itself the gantry weighs about 2Kg which is less than 10% of the total movable mass. The total projected area of everything (i.e. the gantry, bearing rails, motors, platens etc.) located within the tunnel is equal to a one inch thick object spanning the tunnel side walls so the blockage is not excessive. Loading the gantry with a 10Kg weight in the center of its one meter span results in a deflection of only 0.05mm. The ends of the gantry are fixed to carriages which move on linear bearings in the X-direction.

The gantry is propelled in the X-direction by a brushless linear d.c. motor which reacts with a long magnet track to provide a maximum propulsive force of 80lbf. The motor is operated as a closed loop servo system with feedback provided by a linear quadrature encoder with a resolution of 10 micron. The maximum speed of the gantry has been tested at 3 m/s. Current linear stepping motor technology cannot match this performance. The two linear bearing rails are fixed to adapter plates which are bolted to a 1.2 x 3.0 m (4 x 10 foot) optics table. One of these adapter plates also supports the magnet track and linear encoder. The optics table provides an extremely rigid mounting platform for the entire assembly. Another significant benefit of the optics table is that it provides

an extremely flat reference surface for alignment purposes.

Measurements are made in the boundary layer forming on a test plate which consists of a 0.375 ± 0.005 inch thick ground aluminum toolplate approximately 1m wide by 2.1m in length. The plate is supported above the optics table by machined standoffs. A dial gauge attached to the traverse indicated that the deviations of the test-plate over the entire traversable X-Z plane were within ± 0.15 mm. The X-axis motor and twin-rail linear bearings are located beneath the test-plate, and rubber strips are attached to the side walls and to the plate to seal the slots that provide access for mounting the gantry. The side walls and flexible ceiling which complete the test-section are attached to a frame that is bolted to the optics table. Full access to the test-plate and traverse assembly can be obtained in minutes by releasing the bolts and hoisting the frame away with a crane.

3. Benefits of the Traverse—Some New Techniques

Automation of the high-speed 3D traverse reduces the time taken for experiments since repetitive control commands do not have to be performed manually. Although this leads to decreased running time for total pressure measurements, the most significant benefits occur when using hot-wire probes.

Hot-wire probes can only be used with an acceptable accuracy when the mean velocity component is large compared to the velocity fluctuations. For a normal wire, the assumption of sensitivity only to the streamwise velocity fluctuations will become poorer as the fluctuations of the other component normal to the wire increase (by simple vector addition). Crossed-wire probes have a theoretical velocity vector wedge-angle limit defined by the normals to each wire. In practice, the allowable flow angle is much less than this owing to wakes which are shed from the prongs. The boundary layer turbulence encountered in the region of adverse pressure gradient is expected to increase to such an extent that these sources of error will become significant. One way around this problem is to fly the probe in the upstream direction at high speed while sampling on the basis of the probe position. The superimposed bias velocity will reduce the magnitude of the turbulent velocity fluctuations relative to the increased velocity seen by the probe so that accurate measurements are possible.

There is another, very distinct, advantage of flying the wire, i.e. measurements can be obtained on a very dense spatial grid. The time required to obtain converged data by repetitively scanning a dense grid can be more than an order of magnitude less than the time required to get the same data by traversing the probe to each point on the grid in succession and taking data with a stationary probe. At the low speeds of this experiment the sampling period must be as long as 100 seconds for adequate data convergence. In this case, the total time to obtain 30 points in a profile in the usual way with a stationary probe is of about 50 minutes duration. In regions where the turbulence intensity is not too high, the probe can be scanned up and down through the layer at

speeds that are quite high but not large enough relative to the mean flow to exceed the thresholds mentioned above. For example, with constant magnitude accelerations of alternating sign and a maximum speed limit of around 0.6 m/s, the oscillation frequency for traversing a distance of 32mm up and back down through a layer is about 4.5Hz. If samples are taken on the basis of the probe position and if 5,000 samples at each point are adequate for data convergence, then only 18 minutes is required to measure the entire profile compared to 50 minutes in the case of the stationary probe. However, a more significant benefit is that there is no time penalty for increasing the spatial density of the grid. For example, if samples are taken for each 0.025mm increment of the probe position, then the spatial density of the grid can be increased by a factor of more than 40 compared to the conventional method with a stationary probe. Also, spanwise derivatives and streamwise derivatives can be measured.

Calibration of crossed-wire probes requires a mechanism in addition to the probe traverse. For example, in dynamic calibration schemes the small perturbation sensitivity of the probe is determined directly by oscillating it back and forth continuously in a steady and uniform free-stream using a mechanical shaker. An alternative calibration scheme consists of imposing a number of flow angles on the probe by rotating it about an axis normal to the plane of the prongs. Intricate mechanisms are usually added to the traverse to perform this function. However, the same effect can be accomplished relative to the probe by moving it at high speed across a uniform free-stream. The advantage of a high speed 3D traverse is that either crossed-wire calibration scheme can be used without the need for additional hardware and without the need to handle probes.

Hot-wire probes must be calibrated frequently in a uniform stream. Using a conventional single-axis traversing system in the adverse pressure gradient experiments would require the removal and reinstallation of fragile and expensive probes from the measurement region for the purpose of calibration. This would be time consuming and risk probe breakage. With a high-speed traversing system this could be performed almost instantly as well as minimizing the chances of probe damage.

Since all the functions described above are under software control, the opportunity exists to create an intelligent system. For example, hot-wire calibration drift is a particularly common and frustrating phenomenon during the course of an experiment. At regular intervals, the probe could be rapidly moved to a reference point in the free-stream to check for drift and another calibration performed (automatically) if some tolerance level was exceeded.

4. Results to Date

4.1 Incoming laminar boundary layer

The boundary layer on the test plate has its origin upstream and, therefore,

it is influenced by the pressure gradients, wall curvature and lateral convergence within the contraction. Since the flow is accelerated by a contraction, the pressure gradients on the side walls are generally favourable. However, it can be shown that for a finite length contraction two regions of adverse pressure gradient exist on the walls in the vicinity of the entrance and the exit. Laminar boundary layers are especially sensitive to adverse pressure gradients and are prone to separation causing increased unsteadiness. Because of the low Reynolds number requirements of the current experiment, the quality of the incoming laminar boundary layer needs even more attention than usual.

Laminar boundary layer profiles were measured with a total pressure probe at a station 8.3cm downstream of the contraction exit for a number of free-stream velocities. The pressure was constant along the test section for these measurements. All the velocity profiles were found to be very near the Blasius profile. In particular the boundary layer corresponding to the lowest velocity of $U_o = 6.3$ m/s planned for the experiment has a shape factor $H = \frac{\delta^*}{\theta} = 2.45$ which is close to that of the Blasius profile ($H = 2.59$).

4.2 Selection of a transition device

The low Reynolds number requirements of the experiment dictates that measurements be obtained close to the boundary layer tripping device. The effect of a simple cylindrical wire has been the subject of many studies, see Schlichting (1979) p. 537 for a review. More recently there have been observations of spanwise irregularities in the boundary layers behind trip wires. Many workers have suggested that distributed three-dimensional roughness elements may be superior for transition purposes. However, the author is not aware of a systematic parametric study that offers a reproducible alternative to a trip wire. The observed irregularities have varying strengths depending on the facility. There is evidence to suggest (see Bradshaw 1965) that the observations are more closely associated with wind tunnel screens rather than with trip wires.

For the reasons outlined above, a simple wire was selected for boundary layer transition. The diameter and streamwise position for a number of wires were determined using the guidelines reported in Schlichting in conjunction with the laminar velocity profile measurements discussed earlier. Satisfactory results were obtained with 1.7mm and 2.0mm (diameter) wires when positioned near the contraction exit. However, when moved to a location 20cm downstream of the contraction, the 1.7mm wire failed to produce transition at all. Transition was intermittent with the 2.0mm wire at this location. These observations can be explained in terms of the adverse pressure gradient (not measured) near the exit of the contraction. Effective transition was obtained with a larger 2.4mm diameter wire at $X = 15$ cm. Measurements of C_f , momentum thickness and shape factor H indicated that a regular turbulent boundary layer is established behind the 2.4mm wire by $X \approx 25$ cm corresponding to a momentum thickness $R_\theta \approx 450$.

4.3 Mean velocity profiles with the pressure gradient

The variation of C_p with streamwise distance is shown in figure 1(a). The streamwise spacing (5cm) of the measurements appears to be adequate since estimates of dC_p/dX obtained with four different numerical schemes are much the same as shown in figure 1(b). Mean velocity profiles were measured on the centerline ($Z=0$) with a 0.042 inch outside diameter total pressure probe which also functioned as a Preston tube for estimating the wall shear stress. The same probe was also used for the spanwise wall shear stress surveys. Mean pressures were determined over a 90 second period requiring about 45 minutes per profile and the data was acquired over a three day period. The probe was traversed under-computer control and once set running in the morning, the experiment proceeded without manual intervention throughout the day.

A number of interesting features can be determined from the data set. A list of quantities derived from the profile data is given in table 1 and some of these have been plotted in figures 2(a)-(f). For $35\text{cm} < X < 55\text{cm}$ the layer thicknesses are approximately constant and the shape of the velocity profiles is similar as indicated by the shape factor. This suggests that the layer in this region is close to equilibrium. The profiles are shown in both wall- and outer-coordinates in both the region of the favorable and the adverse pressure gradients in figures 3(a)-(d). Estimates of the skin friction coefficient C_{f_o} obtained from the Preston tube have been used to plot the profiles shown in wall-coordinates. The pressure gradients are well within the allowable limits suggested by Patel (1965). The deviations from the log law indicate that uncertainties of up to 10% in wall shear stress may have to be accepted.

4.4 Checks for two-dimensionality

The results of two spanwise C_f surveys are shown in figure 4(a). The location of the upstream survey corresponds to the region where the layer is in equilibrium. The survey spans approximately 40 boundary layer thicknesses and the variations are within $\pm 5\%$ of the mean value. The downstream location in the region of adverse pressure gradient corresponds to $R_\theta \approx 1400$ which is within the capabilities of Spalart's simulations. The spanwise extent of the survey is about 20 layer thicknesses, and again the variations are within $\pm 5\%$ of the mean value. The momentum balance shown in figure 4(b) is within 10%. The spanwise C_f measurements and the momentum balance indicate that the flow is acceptably two-dimensional.

5. Conclusions

The boundary layer in the remodelled Boundary Layer Wind Tunnel is closely related to the capabilities of Spalart's simulations. In particular, the layer appears to be close to equilibrium just before application of the adverse pressure gradient which is a suitable initial condition for a simulation. The pressure gradient parameter $\beta_x \approx 2$ at $R_\theta \approx 1650$ which is about the upper limit of the

numerical simulation capabilities. At this location, the distance downstream of the contraction is equal to the width of the test section. The spanwise variation of C_f is within $\pm 5\%$ and the momentum balance is good.

The high-speed computer-controlled 3D traverse has unique capabilities that will allow hot-wire measurements with a high spatial density to be obtained very quickly. Accurate measurements can be obtained on the "fly" in regions of high turbulence intensity that would otherwise be subject to gross uncertainties using stationary probes.

REFERENCES

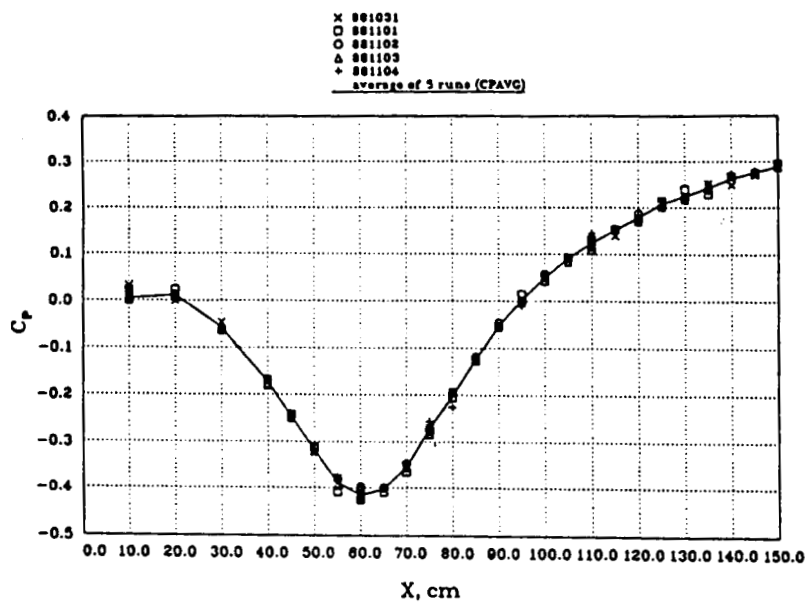
- BRADSHAW, P. 1965 The effect of wind tunnel screens on nominally two-dimensional boundary layers. *J. Fluid Mech.* **22**, 679.
- INMAN, P.N. & BRADSHAW, P. 1981 Mixing length in low Reynolds number turbulent boundary layers. *AIAA J.* Vol. 19, No. 5, 653-655.
- PATEL, V.C. 1965 Calibration of the Preston tube & limitations on its use in pressure gradients. *J. Fluid Mech.* **23**, 185-208.
- SCHLICHTING, H. 1979 *Boundary Layer Theory*. 7th ed. McGraw-Hill, New York.
- SPALART, P.R. 1988 Direct simulation of a turbulent boundary layer up to $Re_\theta=1410$. *J. Fluid Mech.* **187**, 61-98.

X cm	C_p	δ_{99} mm	δ^* mm	θ mm	δ_s mm	C_{f_e} $\times 10^3$ Prest.	C_{f_e} $\times 10^3$ Loglaw	H	β_s $\frac{t}{r_0} \frac{dP}{dz}$	R_s	ΔU^+ max	C_{f_0} $\times 10^3$ Using U_0
25	-0.20	8.50	1.56	1.00	0.75	5.75	5.68	1.555	-0.181	434.3	-	5.87
30	-0.60	10.27	1.60	1.06	0.82	5.85	5.75	1.501	-0.261	469.3	-	6.20
35	-0.10	11.03	1.67	1.13	0.88	5.71	5.65	1.477	-0.295	509.6	-	6.28
40	-0.17	11.69	1.68	1.14	0.90	5.62	5.60	1.465	-0.371	530.2	-	6.57
45	-0.24	12.07	1.66	1.13	0.90	5.52	5.59	1.467	-0.350	541.1	-	6.84
50	-0.31	12.92	1.73	1.19	0.94	5.36	5.50	1.457	-0.352	585.7	-	7.02
55	-0.38	13.02	1.75	1.20	0.95	5.26	5.47	1.453	-0.337	606.2	-	7.26
60	-0.41	13.27	1.78	1.24	0.98	5.28	5.41	1.440	-0.261	633.1	-	7.44
65	-0.40	14.35	2.05	1.41	1.11	4.89	5.16	1.450	0.198	717.4	0.140	6.84
70	-0.35	15.43	2.38	1.63	1.26	4.63	4.76	1.453	0.560	814.4	0.841	6.25
75	-0.27	17.23	2.81	1.91	1.44	4.29	4.42	1.474	0.748	925.6	1.550	5.45
80	-0.19	19.18	3.45	2.29	1.69	3.92	3.96	1.505	1.116	1074.0	2.650	4.67
85	-0.12	21.78	4.11	2.70	1.96	3.65	3.60	1.521	1.527	1229.0	3.640	4.09
90	-0.05	22.82	4.86	3.16	2.20	3.35	3.25	1.559	1.684	1392.0	4.930	3.52
95	-0.00	25.24	5.61	3.56	2.48	3.20	3.15	1.575	1.788	1531.0	5.150	3.20
100	0.06	27.33	6.35	3.98	2.73	3.08	2.89	1.595	2.008	1659.0	6.220	2.89
105	0.09	29.11	7.11	4.39	2.96	2.86	2.70	1.621	1.936	1800.0	7.080	2.60
110	0.12	31.61	7.83	4.80	3.21	2.85	2.56	1.630	1.731	1936.0	7.720	2.51
115	0.15	32.94	8.56	5.20	3.45	2.76	2.46	1.646	2.036	2061.0	8.340	2.35
120	0.19	34.69	9.28	5.59	3.67	2.69	2.36	1.661	2.392	2163.0	8.840	2.18
125	0.21	36.54	9.88	5.92	3.86	2.69	2.35	1.669	2.171	2262.0	8.820	2.13
130	0.22	39.17	10.54	6.32	4.13	2.68	2.30	1.666	1.790	2400.0	9.040	2.09
135	0.24	42.44	11.56	6.81	4.39	2.41	2.16	1.549	2.299	2553.0	9.860	1.83
140	0.26	44.31	12.18	7.15	4.61	2.41	2.10	1.703	1.909	2644.0	10.34	1.78

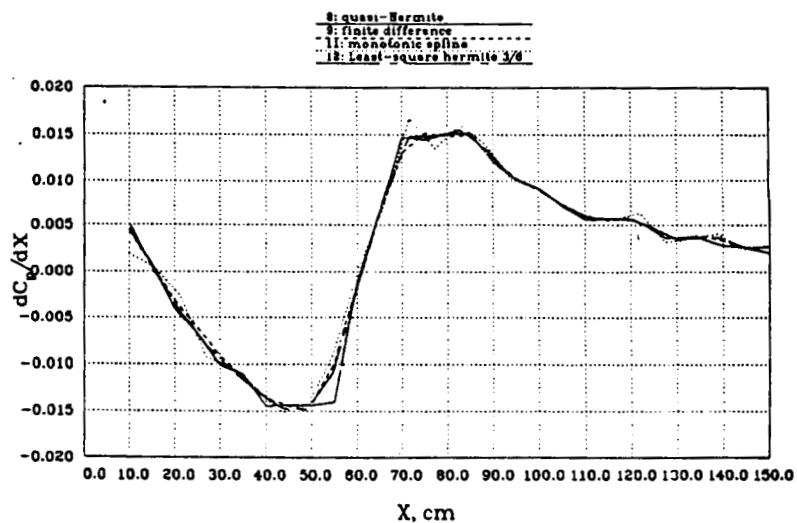
TABLE1. Streamwise Development of Mean Velocity Profiles with Pressure Gradient

NOTE:

1. Reference inlet velocity $U_0 \approx 6.5$ m/s at $X=0$ cm.
2. Boundary layer trip wire is at $X=15$ cm.



(a)



(b)

Figure 1(a) Variation of Pressure Coefficient C_p with streamwise distance.
 (b) Estimates of dC_p/dX using four numerical schemes.

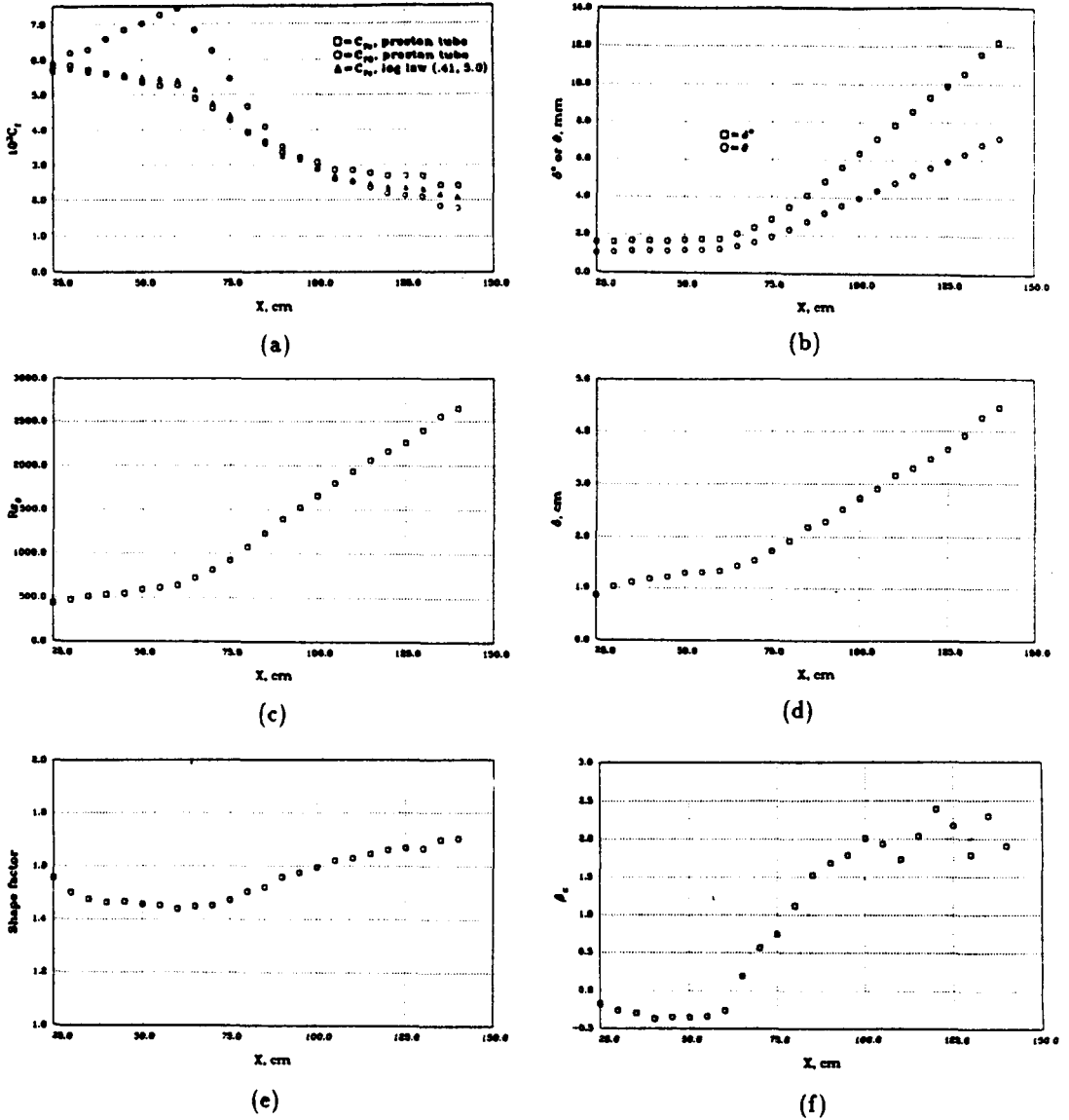


Figure 2. Variation of quantites derived from profile data with streamwise distance.

- (a) Skin Friction Coefficient C_f (b) Displacement δ^* and momentum θ thicknesses
 (c) Reynolds number based on momentum thickness R_θ (d) Boundary layer thickness δ
 (e) Shape Factor $H = \frac{\delta^*}{\theta}$. (f) Pressure gradient parameter $\beta_z = \frac{\delta^*}{\tau_w} \frac{dP}{dz}$

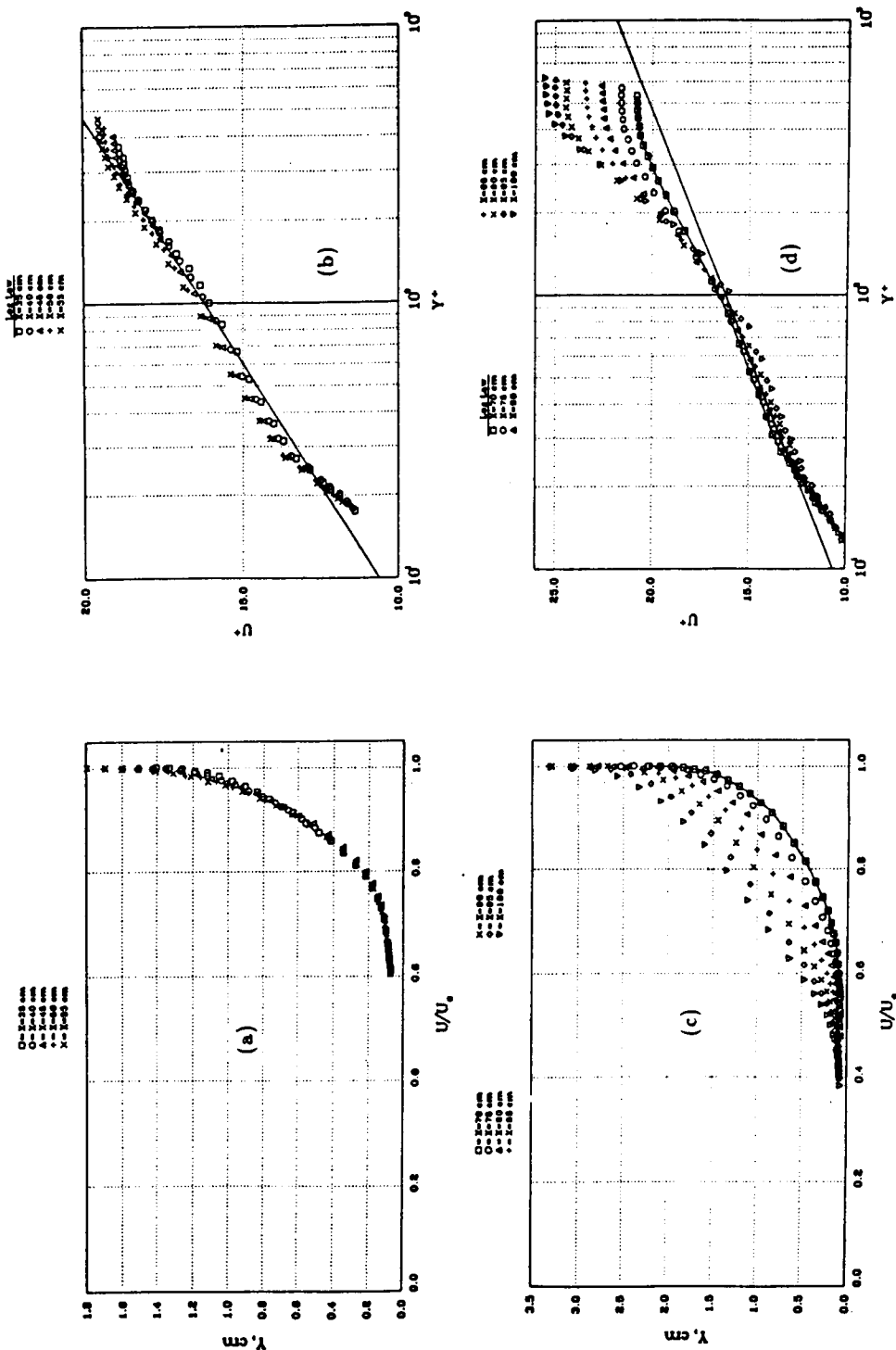


Figure 3. Mean velocity profiles.
(a) Region of favorable pressure gradient and (b) in wall coordinates.
(c) Region of adverse pressure gradient and (d) in wall coordinates.

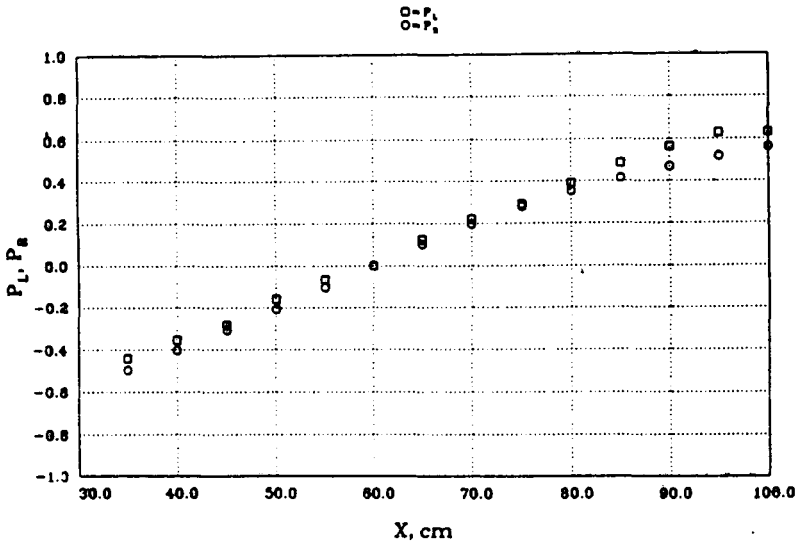
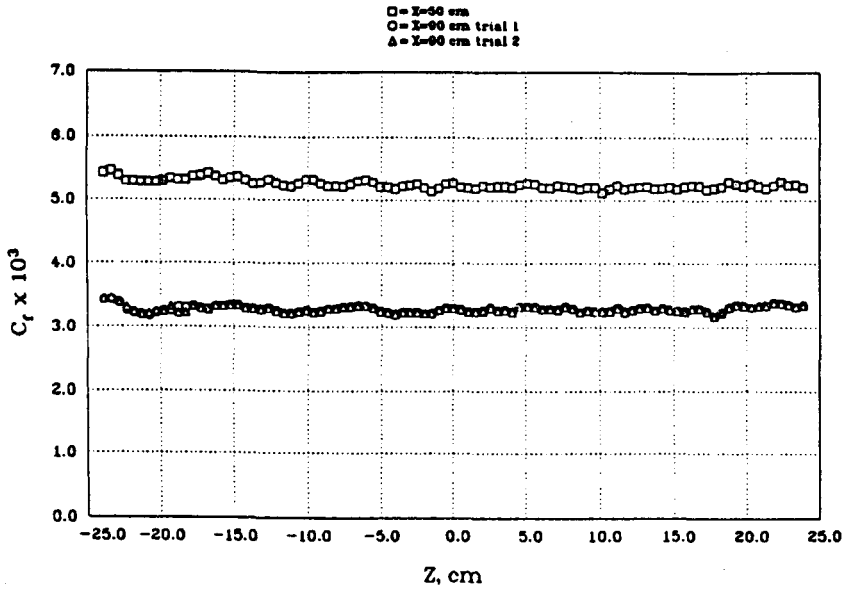


Figure 4(a) Spanwise variation of C_f at $X=50$ cm and $X=90$ cm.
(b) Momentum balance.

APPENDIX

CENTER FOR TURBULENCE RESEARCH 1988 ROSTER

<u>NAME/TERM</u>		<u>AREA OF RESEARCH</u>
POSTDOCTORAL FELLOWS		
CABOT, Dr. William H. 3/88 - present	Ph.D. Physics, 1983, University of Rochester	Turbulence in the early solar nebula, convection
KARNIADAKIS, Dr. George 9/87 - 2/88	Ph.D. Mechanical Engineering, Massachusetts Institute of Technology	Simulation and analysis of basic complex geometry turbulent flows
LEE, Dr. Moon J. 12/87 - present	Ph.D. Mechanical Engineering, 1985, Stanford	Turbulence physics and modeling
LELE, Sanjiva 1/88 - present	Ph.D. Mechanical Engineering, 1985, Cornell University	Direct numerical simulation of compressible free shear flows
POINSOT, Dr. Thierry 9/88 - present	Docteur es Sciences, Mechanical Engr., 1987, Univ. d'Orsay, France	Direct simulation of turbulent reacting flows
SHIH, Dr. Tsan Hsing 4/87 - present	Ph.D Mechanical Engineering, 1984, Cornell University	Turbulence modeling
SMITH, Dr. Leslie M. 9/88 - present	Ph.D. Applied Mathematics, 1988, Massachusetts Institute of Technology	Renormalization group theory of turbulence
STANAWAY, Dr. Sharon K. 6/88 - 12/88	Ph.D. Aeronautics and Astronautics, 1988, Stanford	Numerical simulation of viscous vortex rings
THOMPSON, Dr. Kevin W. 6/87 - present	Ph.D. Physics, 1985, Princeton	Direct numerical simulation of compressible turbulent flows with application to the early evolution of solar nebula
VASTANO, Dr. John A. 9/88 - present	Ph.D. Physics, 1988, University of Texas at Austin	Low dimensional chaos in turbulence

NAME/TERM**AREA OF RESEARCH**

VEGT, Dr. Jaap van der 9/88 - present	Ph.D. Mathematics, 1988, Delft Univ. of Technology, The Netherlands	Transition to turbulence at hypersonic speeds
WATMUFF, Dr. Jonathan H. 11/87 - present	Ph.D. Mechanical Engineering, 1979, University of Melbourne, Australia	Experimental investigation of turbulent boundary layers with adverse pressure gradient

SENIOR POSTDOCTORAL FELLOWS

BROADWELL, Dr. James E. 8/88 - present	California Institute of Technology	Turbulent reacting flows
BROWNE, Dr. L. W. B. 2/88 - 8/88	University of Newcastle - Australia	Experimental investigation of flow over backward facing step
ETEMADI, Prof. Nassrollah 8/87 - 5/88	University of Illinois	Lagrangian statistics
GERMANO, Prof. Massimo 11/88	University of Torino - Italy	Subgrid scale modeling and filtering
LESIEUR, Prof. Marcel 4/88 - 5/88	University of Grenoble, France	Two-point closures
LILLY, Prof. Douglas K. 8/88 - 12/88	CIMMS - University of Oklahoma	Subgrid scale modeling
MELANDER, Dr. Mogens 5/88 - 7/88	Univ. of Pittsburgh	3D vortex dynamics at high Reynolds numbers
ROSHKO, Prof. Anatol 4/88	California Institute of Technology	Turbulent free shear flows

APPENDIX

NAME/TERM

AREA OF RESEARCH

GRADUATE STUDENTS

BEAUDAN, Patrick
10/87 - present

Numerical methods

COLONIUS, Timothy
7/88 - 9/88

Aerodynamic noise

KASSINOS, Stavros
10/88 - present

Reynolds averaged
turbulence modeling

LE, Hung
4/88 - present

Direct numerical
simulation of flow over a
backward facing step

LEE, Sangsan
4/88 - 12/88

Shock/turbulence
interaction

NEVES, Joao
10/87 - 4/88

Numerical simulation of
axial flow over a cylinder

PLESNIAK, Michael
1/88 - 6/88

Effects of curvature on the
structure of mixing layers

POLIFKE, Wolfgang
City Univ. of NY
10/88 - 12/88

Topological complexity of
the vorticity field in
homogeneous turbulence

SASGES, Michael
7/88 - 9/88

Mixing in curved shear
layers

SORAKAYALPET,
Sundaresan
10/87 - 4/88

Space-time characteristics
of wall -pressure
fluctuations

SQUIRES, Kyle
10/87 - 9/88

Effects of particle loading
on turbulent structure and
modeling